Title
Ion emission and expansion in laser-produced tin plasma

Author
Burdt, Russell Allen

Publication Date
2011

UNIVERSITY OF CALIFORNIA, SAN DIEGO

Ion Emission and Expansion in Laser-Produced Tin Plasma

A dissertation submitted in partial satisfaction of the
requirements for the degree
Doctor of Philosophy

in

Electrical Engineering (Applied Physics)

by

Russell Allen Burdt

Committee in charge:

Farrokh Najmabadi, Chair
Farhat Beg
Kevin Quest
Mark Tillack
George Tynan

2011

The dissertation of Russell Allen Burdt is approved, and it is acceptable in quality and form for publication on microfilm and electronically:

Chair

University of California, San Diego

2011

EPIGRAPH

These are some of the things that hydrogen atoms do given fifteen billion years of cosmic evolution.
—*Carl Sagan*

TABLE OF CONTENTS

LIST OF FIGURES

LIST OF TABLES

ACKNOWLEDGMENTS

This work would not have been possible without the involvement of numerous others. Most importantly, Professor Farrokh Najmabadi deserves a very sincere acknowledgment for his contributions to this work. Shortly after I joined the Center for Energy Research in late 2006, Prof. Najmabadi presented challenging projects in the lab to provide a hands-on introduction the rich field of laser produced plasmas. Together, we converged on a direction for my doctoral research, and met regularly to discuss the numerous challenging issues involved. Throughout, Prof. Najmabadi provided an intellectually stimulating and politic-free research environment with access to all necessary technical equipment. I am grateful for the scientific methods and principles I learned as a graduate student under Prof. Najmabadi, and look forward to applying them in my future career.

It is also an honor to acknowledge the additional members of my doctoral committee, Dr. Mark Tillack, Prof. Farhat Beg, Prof. Kevin Quest, and Prof. George Tynan. Dr. Mark Tillack was an integral part of this work, as he supervised much of the work in the laser plasma and laser matter interactions laboratory, and approved and funded many of my expensive equipment purchases. Dr. Tillack was also invaluable in helping prepare many manuscripts and presentations over the years.

This work also utilized the vast talents of many technicians, machinists, undergraduate assistants, and visiting scientists. Sincere acknowledgments are deserved by John Pulsifer, who helped on a daily basis with vacuum equipment, in addition to Tyler Lynch, Matt Baldwin, and Leo Chousal, who all provided invaluable support in various machining, fabrication, and welding activities. Rigoberto Marin supported my efforts to obtain insightful electronics advice and electrical components free of charge. It was also a pleasure interacting with our foreign visiting scientists. Nek Muhammad Sheikh from University of Sindh in Pakistan, and Yoshifumi Ueno from Komatsu Corporation in Japan, were both involved directly in my experiments, and both made valuable contributions of their own in the laboratory.

Chapter 4, in part, has been published in Journal of Applied Physics in 2009. The dissertation author was the primary investigator and author of this material. Contributing to the experiments and analyses were Sam Yuspeh, Kevin Sequoia, Yezheng Tao, Mark

Tillack, and Farrokh Najmabadi, all of whom are associated with the Center for Energy Research at the University of California, San Diego.

Chapter 5, in part, has been published in both Journal of Applied Physics in 2010 and Applied Physics Letters in 2010. The dissertation author was the primary investigator and author of this material. Contributing to the Journal of Applied Physics article in 2010 were Yezheng Tao, Mark Tillack, Sam Yuspeh, and Farrokh Najmabadi of the Center for Energy Research at the University of California, San Diego. Nek M. Shaikh of the University of Sindh in Pakistan, and Eli Flaxer of the Tel-Aviv Academic College of Engineering in Israel also were contributing authors. The Applied Physics Letters article in 2010 was co-authored by Yoshifumi Ueno of Komatsu Corporation in Japan, in addition to Yezheng Tao, Sam Yuspeh, Mark Tillack, and Farrokh Najmabadi of the Center for Energy Research at the University of California, San Diego.

Chapter 6 and Chapter 7 were also, in part, previously reported in the Journal of Applied Physics article in 2010. The dissertation author was the primary investigator and author of this material, and the co-authors of this article were listed in the previous paragraph.

VITA

2004	B. S. in Electrical Engineering *Magna cum Laude*, University of Missouri Columbia
2007	M. S. in Electrical Engineering, University of Missouri Columbia
2011	Ph. D. in Electrical Engineering, University of California, San Diego

PUBLICATIONS

R. Burdt, Y. Ueno, Y. Tao, S. Yuspeh, M.S. Tillack, and F. Najmabadi, "Recombination effects during expansion into vacuum in laser produced Sn plasma", *Applied Physics Letters*, **97**, 041502 (2010)

R. Burdt, Y. Tao, M.S. Tillack, S. Yuspeh, N.M. Shaikh, E. Flaxer, and F. Najmabadi, "Laser wavelength effects on the charge state resolved ion energy distributions from laser-produced Sn plasma", *Journal of Applied Physics*, **107**, 043303 (2010)

R. Burdt, S. Yuspeh, K.L. Sequoia, Y. Tao, M.S. Tillack, and F. Najmabadi, "Experimental scaling law for mass ablation rate from a Sn plasma generated by a 1064 nm laser", *Journal of Applied Physics*, **106**, 033310 (2009)

S. Yuspeh, Y. Ueno, M.S. Tillack, R. Burdt, Y. Tao, and F. Najmabadi, "Cavity formation in a liquid Sn droplet driven by laser ablation pressure for an extreme ultraviolet light source target", *Journal of Applied Physics*, **109**, 076102 (2011)

S. Yuspeh, K.L. Sequoia, Y. Tao, M.S. Tillack, R. Burdt, and F. Najmabadi, "Heating dynamics and extreme ultraviolet radiation emission of laser-produced Sn plasmas", *Applied Physics Letters*, **96**, 261501 (2010)

Y. Tao, M.S. Tillack, S. Yuspeh, R. Burdt, and F. Najmabadi, "Non-classical hydrodynamic behavior of Sn plasma irradiated with a long duration CO_2 laser pulse", *Applied Physics B - Lasers and Optics*, **99**, 397 (2010)

Y. Tao, M.S. Tillack, S. Yuspeh, R. Burdt, N.M. Shaikh, N. Amin, and F. Najmabadi, "Interaction of a CO_2 laser pulse with tin-based plasma for an extreme ultraviolet lithography source", *IEEE Transactions on Plasma Science*, **38**, 714 (2010)

Y. Tao, M.S. Tillack, N. Amin, R. Burdt, S. Yuspeh, N.M. Shaikh, and F. Najmabadi, "Flexible CO_2 laser system for fundamental research related to an extreme ultraviolet lithography source", *Review of Scientific Instruments*, **80**, 123503 (2009)

S. Yuspeh, K.L. Sequoia, Y. Tao, M.S. Tillack, R. Burdt, and F. Najmabadi, "Optimization of the size ratio of Sn sphere and laser focal spot for an extreme ultraviolet light source", *Applied Physics Letters*, **93**, 221503 (2008)

Y. Tao, M.S. Tillack, K.L. Sequoia, R. Burdt, S. Yuspeh, and F. Najmabadi, "Efficient 13.5 nm extreme ultraviolet emission from Sn plasma irradiated by a long CO_2 laser pulse", *Applied Physics Letters*, **92**, 251501 (2008)

K.L. Sequoia, Y. Tao, S. Yuspeh, R. Burdt, and M.S. Tillack, "Two dimensional expansion effects on angular distribution of 13.5 nm in-band EUV emission from laser-produced Sn plasma", *Applied Physics Letters*, **92**, 221505 (2008)

Y. Tao, M.S. Tillack, S.S. Harilal, K.L. Sequoia, R. Burdt, and F. Najmabadi, "Mass-limited Sn target irradiated by dual laser pulses for an extreme ultraviolet lithography source", *Optics Letters*, **32**, 1338 (2007)

ABSTRACT OF THE DISSERTATION

Ion Emission and Expansion in Laser-Produced Tin Plasma

by

Russell Allen Burdt

Doctor of Philosophy in Electrical Engineering (Applied Physics)

University of California, San Diego, 2011

Professor Farrokh Najmabadi, Chair

Laser produced Sn plasma, in its role as an efficient extreme ultraviolet (EUV) x-ray source, is being studied extensively in support of next generation manufacturing of integrated circuits by nanolithography. The ability to diagnose and manipulate the properties of ions emitted from the laser produced plasma (LPP) must be achieved in order for the technology to meet stringent performance requirements. Here we study the emission and expansion of ions from Sn LPP, in parameter space relevant to the EUV x-ray source application. Several particle and radiation plasma diagnostics, in addition to analytical and numerical analysis, are all used to elucidate the complex relationships between the target properties, irradiation conditions, and resultant plasma and ion properties. Two specific laser systems of current interest to the application, at wavelengths

of 1.064 μm and 10.6 μm, are both utilized, which allows for direct comparisons of the effects of laser wavelength on ion properties.

Details of the available experimental apparatus, including the Nd:YAG and CO_2 laser systems, are discussed first. Following, the design and realization of a custom charged particle plasma diagnostic, hereafter referred to as the ion probe, is described. The successful development of the ion probe enabled measurements of the energy distribution for each charge state of each ion species in expanding plasma, which is a new diagnostic capability.

Measurements of mass ablation from Sn plasma produced by a 1.064 μm laser are discussed next, specifically the scaling of mass ablation rate with laser intensity. These measurements are useful in the design of mass-limited targets, and also are used to infer mechanisms of laser energy absorption and heat conduction within the plasma. In addition to the ion probe, an EUV spectrometer and a calibrated EUV calorimeter were both utilized as diagnostics to measure the mass ablation rate by complementary methods. Laser intensity was scanned from $3 \times 10^{11}\,\mathrm{W/cm^2}$ to $2 \times 10^{12}\,\mathrm{W/cm^2}$, encompassing parameter space of the EUV x-ray source application to the low end of parameter space of the laser fusion application. Accordingly, previous theoretical results relevant to the laser fusion application can be applied in the data analysis.

Experiments at two different laser wavelengths to extensively study the dynamics of ion expansion into vacuum are discussed next. In one set of experiments, the ion probe was used to measure energy distributions for all charge states of Sn ions at laser intensities of $3 \times 10^{11}\,\mathrm{W/cm^2}$ and $2 \times 10^{10}\,\mathrm{W/cm^2}$, from 1.064 μm and 10.6 μm lasers, respectively. At the longer laser wavelength, higher charge state ions are observed. At both laser wavelengths, the peak ion energies increase approximately linearly as a function of charge state, and all ion energies greatly exceed the initial thermal electron temperature. In a second set of experiments, the distance from the target surface over which the charge state distribution evolves in vacuum is investigated. A Faraday cup translated along the path of plasma expansion is utilized in these measurements. It was found that at the longer laser wavelength, the charge state distribution is decaying to lower charge states over distances up to hundreds of millimeters from the target surface, whereas at the shorter laser wavelength the charge state distribution reaches a frozen-in state within a few tens of millimeters from the target surface. These experimental results are used to infer mechanisms of ion acceleration and recombination in the expanding plasma.

In the last section, analytical models of ion expansion into vacuum relevant to the experimental results are first discussed. More detailed analyses are then carried out through numerical simulations. First, a zero-dimensional code following the time evolution of plasma temperature and the population of each ion species is discussed and used to verify some qualitative features observed in the experiments. A more complex one-dimensional Lagrangian hydrodynamics code utilizing the zero-dimensional code as one step in its algorithm is then used to simulate ion properties throughout the spatial expansion into vacuum. Due to the significant number of assumptions made in both codes, only qualitative features of the experiments are reproduced.

Chapter 1

Introduction

1.1 Motivation for Continued Study of Laser Produced Plasma

Transient plasma produced by focused laser radiation finds considerable application in diverse technologies such as inertial fusion energy [1], laser ablation and deposition [2], x-ray emission [3], and particle acceleration [4]. Several decades of research has been devoted to understanding the many complex and interrelated processes occurring throughout the laser plasma interaction, from initial ionization of the target, to laser heating, emission of radiation, hydrodynamic expansion, and interaction with the surrounding environment [5] [6] [7] [8]. However, a more thorough understanding of these processes is still required to advance and develop the many applications of laser produced plasma.

Numerous complex processes occur over disparate spatial and temporal scales as a result of the interaction of focused laser radiation with matter. The photon energy of the laser field, $(E_p/\mathrm{eV}) \approx 1.2/\lambda$ where λ is the laser wavelength in μm, is a few eV for ultraviolet lasers and close to 1 eV for infrared lasers – in both cases less than the first ionization potential of most atoms. Initial ionization proceeds by other mechanisms, such as multi-photon ionization [5], and free electrons are generated at the target surface in time scales on the order of 10 ps, which is much shorter than the long pulse durations used here (> 1 ns). Following the initial ionization, laser energy

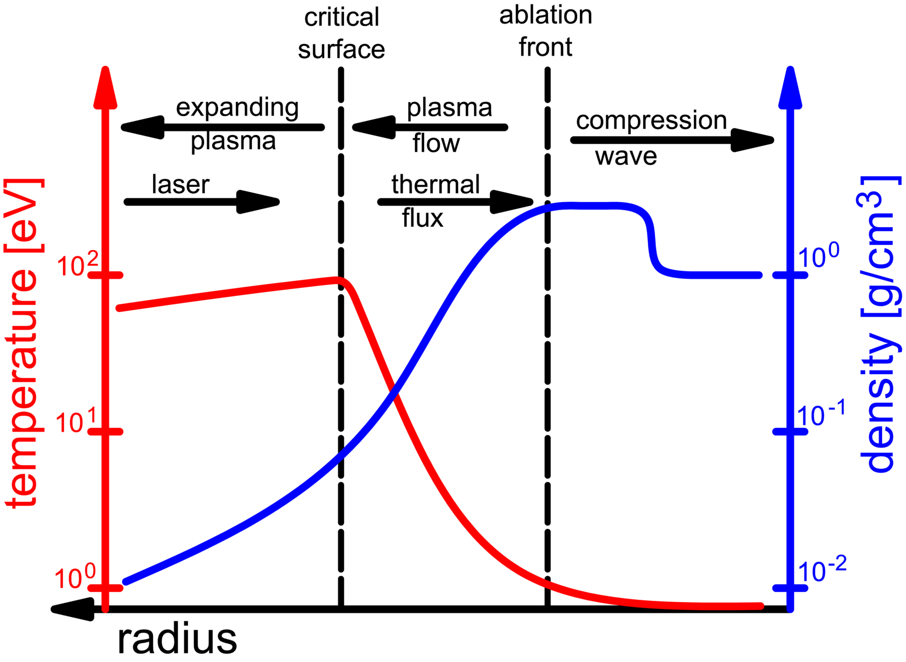

Figure 1.1: Spatial variation of plasma properties close to the target surface.

is absorbed in the plasma by a variety of linear and nonlinear processes, depending on the incident laser conditions [6]. At the low laser intensities of the present experiments ($< 10^{15}/\lambda^2$ W/cm^2), the dominant absorption mechanism is inverse bremsstrahlung, where electrons absorb energy from the radiation field during collisions with ions [9]. A steady-state ablation regime, as illustrated in Figure 1.1, is established during the laser pulse if the ratio L/v_S is less than the laser pulse duration [10], where L is the initial plasma size and v_S is the expansion velocity; in these experiments, $L \approx 100\,\mu\mathrm{m}$ and $v_S \approx 5 \times 10^6\,\mathrm{cm/s}$, therefore a few nanoseconds is required.

For the duration of the laser pulse, the steady-state ablation regime is established and the plasma properties vary spatially in different regions separated by two distinct surfaces [11]. The critical surface is defined where the laser frequency is balanced by the plasma frequency, the characteristic time scale at which plasma electrons shield out charge non-neutralities. The plasma density at the critical surface, n_{cr}, is laser wavelength dependent,

$$\left(\frac{n_{cr}}{\mathrm{cm}^{-3}}\right) = (1.1 \times 10^{21}) \left(\frac{\lambda}{\mu\mathrm{m}}\right)^{-2}, \tag{1.1}$$

which results in a two order of magnitude difference for the two laser wavelengths used in these experiments (1.064 and 10.6 μm). The laser field is reflected at the critical surface and absorbed in the coronal plasma, extending from the critical surface towards the direction of the incident laser, over a region where the electron ion collision frequency is sufficiently high. Electrons heated by inverse bremsstrahlung, and plasma radiation emanating in the coronal plasma, transport towards the ablation front in the conduction region. Here there is a steep gradient in temperature between the hot coronal plasma and the cold target surface. At the ablation front, material from the target surface is continuously ablated and ionized for the duration of the laser pulse. Finally, a shock wave is driven into the solid target behind the ablation front, raising its density above the solid value, and resulting in additional mass ablation following the laser pulse. In the far expansion zone, beyond the coronal plasma, the expanding plasma interacts with its surrounding environment. In vacuum, the plasma expands quasi-adiabatically and electrons and ions remain coupled for time scales on the order of the electron ion thermalization time. As long as the electrons and ions remain coupled, significant changes to the ionization distribution occur through recombination, and depending on the initial conditions the plasma can completely recombine or can freeze into an ionization distribution with a nonzero average charge state [8].

1.2 Review of Relevant Applications of Laser Produced Plasma

Numerous applications make use of the aforementioned processes occurring throughout the laser plasma interaction. Perhaps the most important application of laser produced plasma is inertial fusion energy, in which the ablation pressure generated in the laser produced plasma is used to compress fusion reactants to thermonuclear conditions [1]. However, research in this field requires a laser source with kilojoules of energy, which is not practical to maintain in a university research laboratory. Several applications of laser produced plasma making use of much smaller table top lasers, suitable for the university laboratory, and relevant to the experiments discussed within, are the extreme ultraviolet x-ray source and the laser ion source; both are reviewed subsequently.

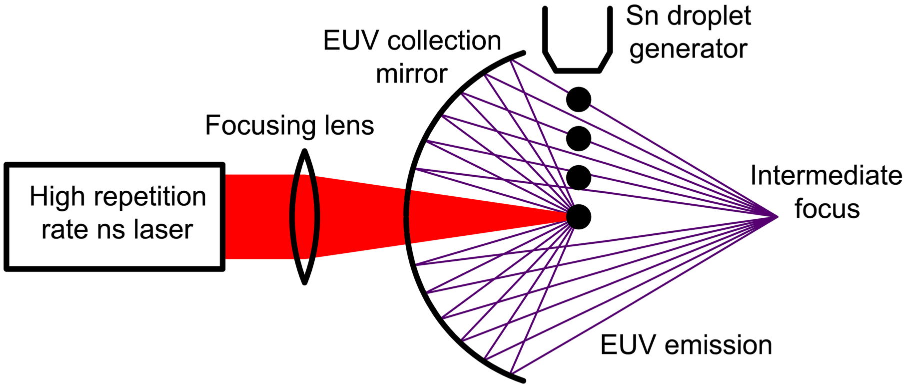

Figure 1.2: General schematic of a LPP EUV x-ray source.

1.2.1 Extreme Ultraviolet X-Ray Source

The extreme ultraviolet x-ray source makes use of laser produced plasma (LPP) as an efficient source of 13.5 nm x-rays, the next generation wavelength for manufacturing of integrated circuits by nanolithography. A general schematic of a LPP EUV x-ray source is shown in Figure 1.2. In the figure, a high-repetition rate ns laser is focused through an aperture in the collection mirror onto a synchronized train of Sn droplets. In the interaction of the laser and droplet, a plasma is formed that emits EUV light into a broad angular distribution. The EUV light is reflected to the intermediate focus with the large EUV collection mirror, positioned on the order a few tens of cm away from the plasma. Following the intermediate focus are EUV collimation and focusing optics, followed by the mask, projections optics, and finally the wafer.

The wavelength requirement of the EUV x-ray source is chosen for compatibility with available x-ray optics with high reflectivity at 13.5 nm [12]. The primary figure of merit of the EUV x-ray source is the conversion efficiency, defined as the percentage of incident laser energy which is re-radiated by the plasma as soft x-rays in a 2% bandwidth centered at 13.5 nm. Early studies converged on Sn as the target material, and on the optimal parameters of the Sn plasma, which produce the highest theoretical and experimental conversion efficiencies [13] [14] [15] [16] [17]. These include electron temperature of 30 to 40 eV and electron density of $10^{19}\,\mathrm{cm}^{-3}$. The atomic transitions responsible for generating the EUV radiation are the 4d–4f and 4p–4d subshells, within Sn^{+7} to Sn^{+12} ions.

In addition to high conversion efficiency, an additional requirement of the LPP EUV x-ray source is long lifetime of the expensive EUV collection mirror, which places stringent requirements on the properties of debris emitted by the plasma. Several system parameters affect both conversion efficiency and emitted debris, including the target composition, target geometry, laser parameters and focusing conditions, and finally the irradiation scheme. In general, the focus of previous research has been to systematically study the effects of these parameters on both the conversion efficiency and emitted debris.

The system parameter with the greatest influence on conversion efficiency and debris is laser wavelength. Laser absorption by inverse bremsstrahlung is enhanced for shorter laser wavelengths, as the collision frequency scales with electron density, which in turn scales with λ^{-2}. However, reabsorption of in-band EUV light is also enhanced in a dense plasma, and additional debris is generated as well. Early studies investigated wavelengths from 266 nm to 1064 nm, concluding that re-absorption was too significant in a plasma generated by a 266 nm laser [18]. Laser wavelengths as high as 10.6 μm, as generated by a CO_2 laser, have also been investigated. These early studies show comparable conversion efficiencies to those obtained by using a 1064 nm Nd:YAG laser [19] [20]. However, debris was reduced at the longer laser wavelength due to the lower critical density, and the EUV spectrum was relatively unchanged as laser intensity was scanned, which indicates reabsorption of EUV light is negligible. In another experiment using a CO_2 laser, the pulse duration was varied from 25 to 110 ns and the conversion efficiency was constant over this range [21], again indicating negligible reabsorption. In contrast, when using a Nd:YAG laser, the conversion efficiency decreases as the pulse duration is extended from 2 to 9 ns, which indicates reabsorption is significant at the shorter laser wavelength [22]. Currently, both laser wavelengths remain candidates for the commercial product. The Nd:YAG laser is advantageous as it can be focused to a smaller spot size, which generates an EUV emitting region of comparable dimensions. However, the CO_2 laser is advantageous because of the reduced debris, negligible reabsorption of EUV light, and because CO_2 laser power can be scaled up easily as compared to the solid-state Nd:YAG laser.

Additional methods have been proposed to improve conversion efficiency and reduce debris at both laser wavelengths. At the 1.064 μm wavelength, in which reabsorption of EUV light has been shown to be significant, efforts have tried to limit the number of Sn atoms in the plasma through the use of mass-limited targets. Thin Sn films on the order of 10 nm, in addition to Sn-doped droplet and foam targets, have all been shown to both generate conversion efficiency comparable to the solid Sn target, but to increase the spectral purity and reduce debris [23] [24] [25]. At the 10.6 μm wavelength, in which reabsorption is negligible, efforts have tried to confine the plasma to increase the plasma density. For example, conversion efficiency has been doubled through the use of targets with pre-formed cavities of dimensions on the same scale as the spot size [26]. At both laser wavelengths, similar methods are used to reduce plasma debris. Electrostatic and magnetostatic repeller fields, background gases, and prepulsing to lengthen the initial density gradient, have all been proven to be effective methods [27] [28] [29].

1.2.2 Laser Ion Source

In contrast to the EUV x-ray source application, the laser ion source application takes advantage of high charge state ions from laser produced plasma, which can be generated from most elements and with energies from hundreds of eV to MeV [30]. Typical laser intensities in the laser ion source application extend from 10^9 to 10^{16} $\mathrm{W/cm^2}$, where resonant and nonlinear laser absorption processes must be considered [31]. Below approximately 10^{14} $\mathrm{W/cm^2}$, laser ion sources are used for ion implantation, in which heavy ions are implanted hundreds of nm into the surface of a material to modify its properties [32]. Over the entire intensity regime, laser ion sources are used to inject heavy ions into accelerators. At lower intensities, a laser ion source can be coupled to an electron cyclotron resonance ion source [33]. At higher laser intensities, the laser ion source can inject, e.g., up to 25-times ionized Pb atoms into a heavy ion synchrotron, such as the Large Hadron Collider at CERN [34].

Similar to the EUV x-ray source application, lasers of varying wavelength are used in the laser ion source application, such as frequency-tripled iodine lasers (438 nm), Nd:YAG lasers (1.064 μm), and CO_2 lasers (10.6 μm) [31] [34]. At lower laser intensities ($< 10^{15}/\lambda^2$ $\mathrm{W/cm^2}$, where λ is the laser wavelength in μm), longer wavelength lasers generate the highest charge state ions in the far expansion zone. Although laser absorption is enhanced for short laser wavelengths, recombination rates in the dense plasma created by a short wavelength laser are sufficiently high so that most ions recombine to lower charge states in the coronal plasma. A theoretical analysis of the laser ion source at low laser intensity reveals ways to improve the yield of high charge state ions – increase the laser pulse duration, minimize the spot size, and increase the radiation wavelength, all of which affect the initial density profile in a manner reducing recombination rates throughout the plasma expansion [8]. At higher laser intensities, above the threshold given previously, the opposite is true, i.e., shorter wavelength lasers generate the highest charge state ions in the far expansion zone [31] [35]. This is due to the production of a suprathermal electron population at high laser intensities through resonant and nonlinear laser absorption processes. The temperature of these electrons scales with the product $I\lambda^2$, where I is the laser intensity, and these electrons do not contribute efficiently to ionization [36].

1.3 Objectives and Organization of the Present Work

The experiments and analyses discussed within address the emission and acceleration of ions from laser produced Sn plasma, as well as the dynamics of ion expansion into vacuum, in parameter space relevant to both the EUV x-ray source and laser ion source applications. Only a single target element, Sn, is investigated, as it is the target element used in the EUV x-ray source application. However, Sn is a high-Z element (Z=50), comparable in its properties to other heavy metals used in laser ion sources, and past studies have demonstrated similar ion properties in laser produced plasma from Cu, Sn, Ta, W, Au, and Pb targets [31] [37].

The several radiation and particle plasma diagnostics are discussed first, with an emphasis on the design and realization of a custom charged particle diagnostic to measure ion energy distributions for each charge state of each ion species present in the plasma. Also discussed initially are the two laser systems used in the experiments – a 1.064 μm Nd:YAG laser and a 10.6 μm CO_2 laser. The remainder, in general, elucidates some of the complex relationships between the target properties, irradiation conditions, and resultant plasma and ion properties, through both experiment and simulation. The following questions are addressed specifically:

- How much total mass is emitted in the laser plasma interaction, and how does the mass ablation scale with the incident laser parameters?
- How does laser wavelength affect the charge states and energies of ions in the far expansion zone?
- How does laser wavelength affect the evolution of the charge state distribution during plasma expansion into vacuum?
- How can the experimental measurements, recorded at distances very far from the target surface as compared the initial spot size, be used to infer plasma properties near the target surface, at the scale of the spot size?
- How do the experimental measurements influence the EUV x-ray source and laser ion source applications?

Following discussions of the experimental apparatus and diagnostic development, the dissertation is organized as follows. First, measurements of mass ablation from Sn plasma produced by a 1.064 μm laser are discussed, as the laser intensity is scanned from $3 \times 10^{11}\,\mathrm{W/cm^2}$ to $2 \times 10^{12}\,\mathrm{W/cm^2}$. The ablation depth is measured by irradiating a thin layer of Sn evaporated onto a Si wafer, and looking for signatures of Si ions in the expanding plasma with radiation and particle diagnostics. The exact scaling of mass ablation rate with laser intensity is calculated and used to infer mechanisms of laser energy absorption and heat conduction within the plasma.

Second, experiments at two different laser wavelengths to extensively study the dynamics of ion expansion into vacuum are discussed. In one set of experiments, ion energy distributions are measured for all charge states of Sn ions at laser intensities of $3 \times 10^{11}\,\mathrm{W/cm^2}$ and $2 \times 10^{10}\,\mathrm{W/cm^2}$, from 1.064 μm and 10.6 μm lasers, respectively. In a second set of experiments, the distance from the target surface over which the charge state distribution evolves in vacuum is investigated. A Faraday cup translated along the path of plasma expansion is utilized in these experiments. The data provide physical insights into the mechanisms of ion acceleration, and recombination in the expanding plasma.

In the last section, analytical models of ion expansion into vacuum relevant to the experimental results are first discussed. More detailed analyses are then carried out through numerical simulations. First, a zero-dimensional code following the time evolution of plasma temperature and the population of each ion species is discussed and used to verify some qualitative features observed in the experiments. A more complex one-dimensional Lagrangian hydrodynamics code utilizing the zero-dimensional code as a step in its algorithm is then used to examine ion properties throughout the spatial expansion into vacuum. Due to the significant number of assumptions made in both codes, only the qualitative features of the experiments are reproduced. Finally, the experimental and theoretical results are summarized and recommendations are made for future studies.

Chapter 2

Experimental Apparatus and Techniques

2.1 Experimental apparatus

The experimental apparatus consists of a laser system, laser optics, laser diagnostics, vacuum chamber and associated vacuum equipment, target and target positioning system, plasma diagnostics, and finally data acquisition and control equipment. The complete experimental arrangement is shown in Figure 2.1.

The laser system is either a 1.064 μm Nd:YAG laser or a 10.6 μm CO_2 laser; additional details on the lasers, optics, and beam diagnostics at each wavelength are discussed in subsequent sections. The vacuum chamber was evacuated by either a turbomolecular pump or a cryopump depending on the date of the experiment, due to various vacuum equipment malfunctions over time. Pressures as low as 10^{-6} torr measured by an ion gauge could be achieved with both pumping systems. Targets were solid Sn in different configurations; more details are in the relevant experimental sections. Target alignment was accomplished with a sophisticated imaging and positioning system. At all times, the target chamber center was imaged real-time in the focal plane and an orthogonal plane, with μm resolution. The target was mounted on a motorized stage with μm accuracy in three translational degrees of freedom, so the target could be positioned in the focal plane with μm accuracy and could also be translated within the focal plane

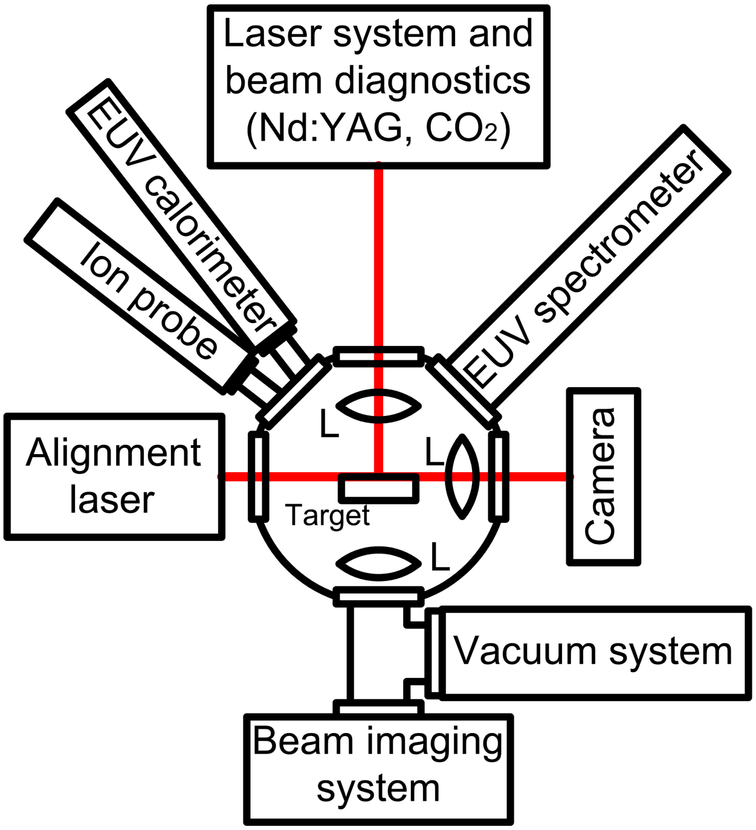

Figure 2.1: Experimental arrangement. L – lens. Variations of this general experimental arrangement are discussed in the relevant experimental section.

before every shot to provide a fresh surface. Additional details on the plasma diagnostics, including data acquisition and instrument control, are discussed in a subsequent section.

2.2 Laser Characterization and Diagnostics

Two specific types of lasers of current interest to the EUV x-ray source application, 1.064 μm Nd:YAG lasers and 10.6 μm CO_2 lasers, were both utilized in these experiments. Although all lasers operate on the same basic principles, the different types, such as solid-state and gas lasers, have very different physical configurations and require beam characterization diagnostics specific to the laser wavelength. The details of both types of laser used in these experiments are therefore discussed separately.

2.2.1 Nd:YAG Laser System

A commercial laser system, the Continuum Surelite II-10, generated the 1.064 μm laser radiation. The Surelite laser uses a single-rod oscillator and Q-switch to produce a polarized laser pulse with full-width-half-maximum pulse duration between 5 and 7 ns and pulse energy up to 650 mJ. The beam can be focused to a $\left(1/e^2\right)$ spot size as low as 50 μm. Accordingly, the irradiance from the Surelite laser can be as high as $5 \times 10^{12}\,\mathrm{W/cm^2}$, which is well above the requirement for optimal conversion efficiency of a Nd:YAG LPP. By adjusting the flashlamp voltage, irradiating the target away from best focus, and adjusting the laser energy with polarization optics, the laser intensity could be varied several orders of magnitude up to its maximum value.

The beam properties of the Surelite laser were diagnosed repeatedly before, during, and after all experiments to ensure constant and well-known irradiation conditions throughout the experimentation schedule. Beamsplitters in the optical path were used to monitor pulse duration and pulse energy real-time during experiments. For these measurements, a fast photodiode (Electro-Optics Technology ET-2000) with a 200 ps rise time, and a calibrated laser energy monitor (Ophir 30(150)A-HE-106), were used. For the measurement of spot size, the method described in Section 2.2.3 was used. Error in the pulse duration measurement was dominated by random shot-to-shot variations of approximately ±0.5 ns. Error in the pulse energy measurement included a probe measurement error (±3%) in addition to random shot-to-shot variations, resulting in error of approximately ±5% of the nominal laser energy. Typical errors in the measurement of spot size were a few microns, as discussed in Section 2.2.3. Taking into account all sources of error in the beam measurements which constitute laser irradiance, typical error in laser irradiance could be kept within ±20% of the nominal value. Exact errors are given in more detail in the relevant experimental section.

2.2.2 CO_2 Laser System

The CO_2 laser system is custom-designed and consists of a master oscillator, pre-amplifier, main amplifier, and plasma switch, in a typical arrangement as shown in Figure 2.2

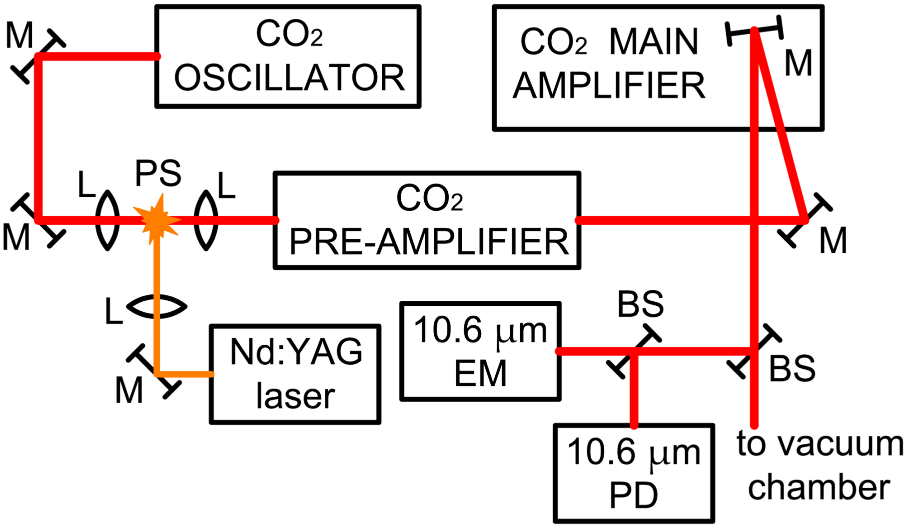

Figure 2.2: Typical arrangement of the CO_2 laser system. M–mirror, L–lens, BS–beamsplitter, PD–photodiode, EM–energy monitor, PS–plasma switch.

The operating principles and beam characteristics of this laser have been described in a previous publication [38], and will be summarized here. The ratio of gases in the oscillator laser cavity is $CO_2 : N_2 : He = 20\% : 4\% : 76\%$. An electrical discharge within the laser cavity excites the N_2 gas, which transfers energy to rotational and vibrational levels of the ground state of the CO_2 molecule, where the lasing occurs. The N_2 gas, in a lower excited state, decays to the ground state by collisions with He atoms. The lifetime of the excited N_2 is long as compared to the lifetime of the desired lasing transitions in the CO_2 molecules, which adds a low intensity tail to the laser pulse lasting several microseconds. This tail does not contribute efficiently to EUV generation from a Sn plasma but does generate debris, and therefore must be removed. In our laser system, the tail of the laser pulse is removed by a plasma switch in the CO_2 optical beam path. The plasma switch consists of the air breakdown of a high-intensity ($\approx 3 \times 10^9\,\mathrm{W/cm^2}$), focused Nd:YAG laser, which is opaque to the light from a CO_2 laser. By externally triggering all the lasers using a programmable timing generator (Stanford Research Systems DG535) with ±0.1 ns jitter, the plasma switch can be fired any time with respect to the main laser pulse. Therefore, the plasma switch can be used to adjust the laser pulse duration over a range of values; temporal measurements of the CO_2 laser pulse with several different pulse durations are shown in Figure 2.3.

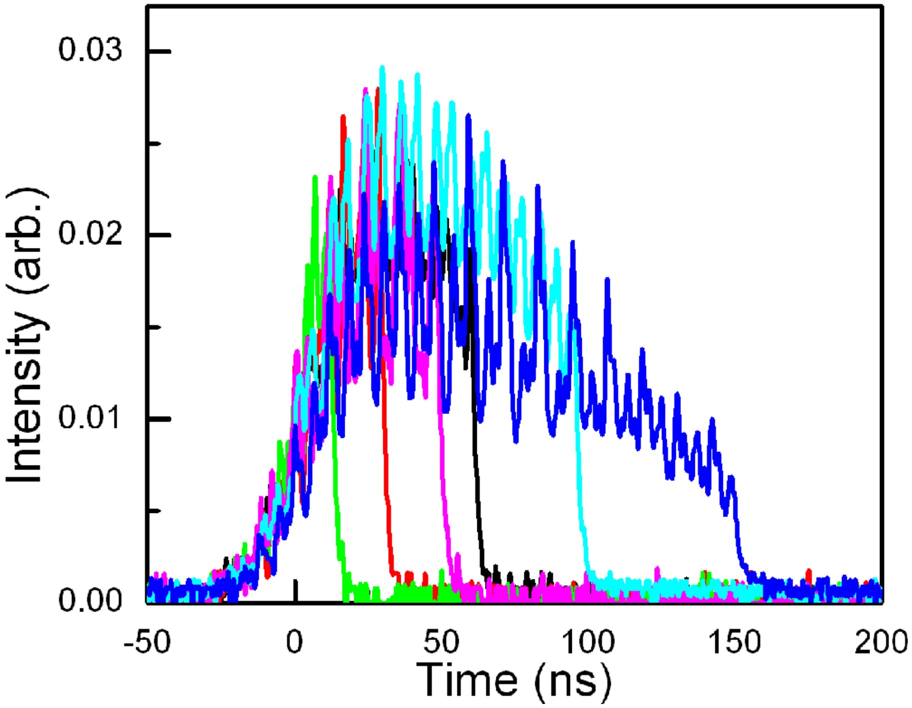

Figure 2.3: Temporal measurements of the CO_2 laser pulse as the delay time between the plasma switch and the master oscillator is scanned. Pulse durations from 10 to 110 ns are demonstrated [38].

The laser pulse passing through the plasma switch from the master oscillator enters a single-pass pre-amplifier and a separate dual-pass amplifier. The overall gain of both amplifiers is 6× without saturation. Details on the amplifiers, such as operating voltage, configuration, and gas mixture can be found in the previous publication [38].

The pulse energy and pulse duration of the CO_2 laser sytem are positively correlated due to the nature of the plasma switch. With all amplifiers, pulse energies of 60, 150, 400, and 500 mJ were measured for pulse durations of 10, 25, 60, and 110 ns, respectively. As with the Nd:YAG laser system, beamsplitters were used to monitor the beam characteristics real-time. A photoelectromagnetic infrared detector (Boston Electronics) was used to monitor the pulse duration, and a calibrated laser energy monitor (Ophir 3A-FS) was used to monitor pulse energy. As discussed in detail in Section 2.2.3, the beam can be focused to a $(1/e^2)$ spot size as low as 80 μm. Accordingly, irradiance as high as 10^{11} W/cm^2 can be achieved, which is greater than the irradiance required for optimal conversion efficiency from a CO_2 LPP. By adjusting the discharge voltage

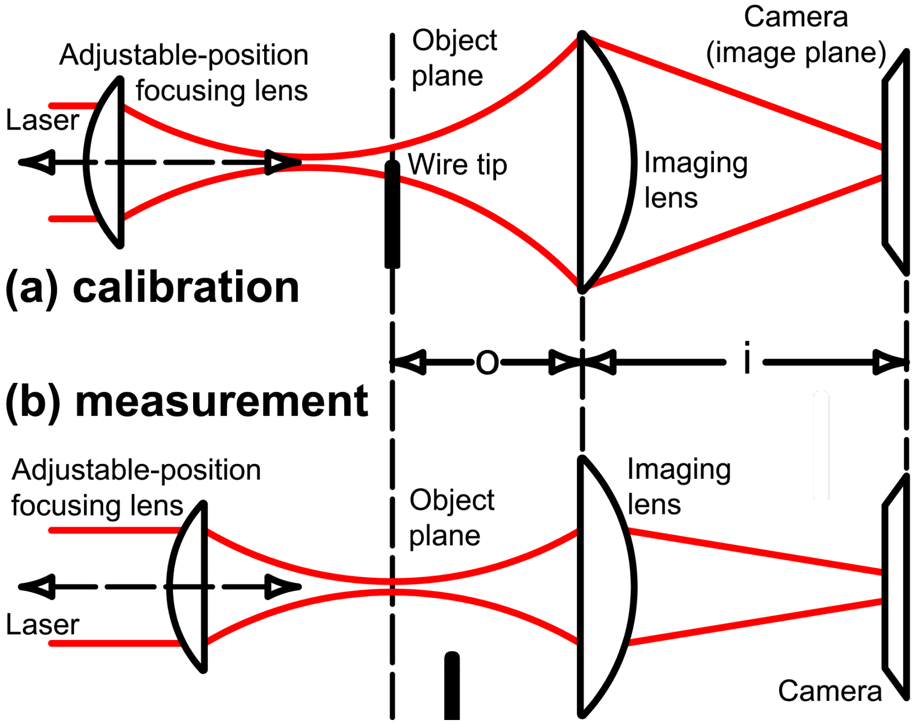

Figure 2.4: Experimental configuration used in the focal diameter measurements. (a) Calibration configuration, (b) Measurement configuration. After the spot size has been measured, the focusing lens is locked into position for the duration of the experiments.

of the master oscillator, the timing of the plasma switch, and irradiating the target away from best focus, the intensity of the CO_2 laser system could be varied several orders of magnitude up to its maximum value. Random shot-to-shot variations in the CO_2 beam characteristics were significant, mostly due to additional timing jitter in the discharge switches of the CO_2 lasers and the Q-switch of the Nd:YAG plasma switch. Errors in the pulse energy and pulse duration could vary by a factor as high as 2 on a shot-to-shot basis. Consequently, all beam characteristics were recorded for every experimental shot with the CO_2 laser system, and only those with energy and pulse duration within a defined range were included in the data analysis; additional details are included in the relevant experimental section.

2.2.3 Spot Size Measurements

A direct imaging technique was used to measure the two dimensional intensity distribution, hereafter referred to as spot size, for both the Nd:YAG and CO_2 lasers. The experimental arrangement used in the spot size measurement is shown in Figure 2.4; separate configurations are required for calibration and measurement. Both are based on a simple imaging system, characterized approximately by the equations for an ideal thin lens in the paraxial ray approximation,

$$\begin{aligned} \frac{1}{f} &= \frac{1}{o} + \frac{1}{i} \\ M &= \frac{i}{o} \end{aligned} \tag{2.1}$$

where f is the focal length of the imaging lens, o is the distance from object plane to the imaging lens, i is the distance from the imaging lens to the camera (the image plane), and M is the magnification of the object plane at the camera. These equations are ideal and do not account for aberrations and diffraction, and therefore cannot be used to reliably calculate the magnification of the imaging system. Accordingly, the imaging system was calibrated with an object of known dimensions on the same order as the nominal spot size. Thin wires with nominal diameters of 20, 50, and 125 μm were used for this purpose; a series of photographs of the thin wires are shown in Figure 2.5.

Additional details on the imaging system at each laser wavelength are explained separately, as equipment specifications vary with wavelength. The charge-coupled device (CCD) camera used to image the 1.064 μm radiation (DataRay WinCamD) has 4.65×4.65 μm pixels arranged in a 1280×1024 array, and thus an active detection area of 6.0×4.8 mm. The different experiments with the Nd:YAG laser discussed within all used slightly different spot sizes due to different focusing conditions; here the images and data analysis for the median spot size (60 μm) are presented. The magnification was set so the nominal spot size would cover at least 50×50 pixels, so that $M \approx 5$.

Images and corresponding lineouts for all important steps in the calibration and measurement process are shown in Figure 2.6. The imaging lens is first adjusted on a micrometer stage until the tip of a thin wire placed at the target chamber center is brought into focus using the laser as a backlighter; the imaging lens is then locked in position. The laser wavelength for backlighting must be the same laser wavelength used in the experiments (as opposed to a He:Ne source of a different wavelength) as the properties of the imaging system will be subject to chromatic aberrations. An image of the tip of the thin wire is then acquired, and because the dimensions of the wire are known, the pixel-

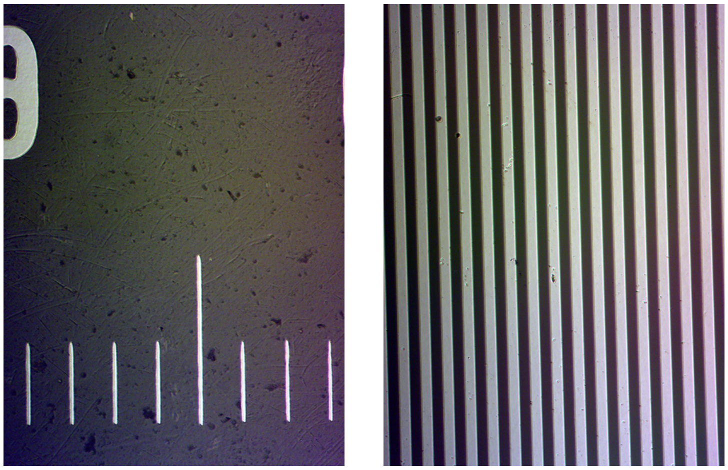

(a) calibrated glass scale, 1 division = 100 µm

(b) calibrated Ronchi ruling, 1 bar = 25 µm

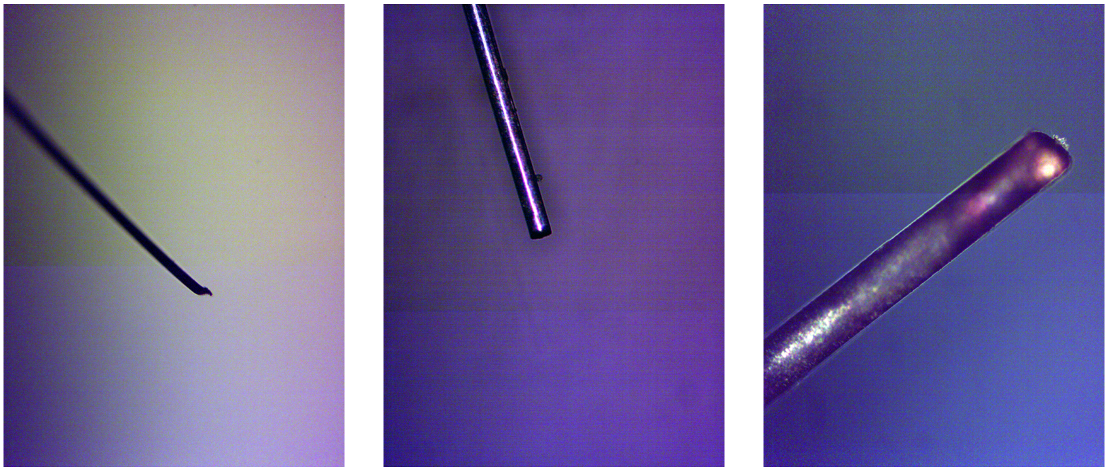

(c) wire with nominal diameter of 20 µm

(d) wire with nominal diameter of 50 µm

(e) wire with nominal diameter of 125 µm

Figure 2.5: Photographs obtained by optical microscopy for accurately measuring the diameter of various thin wires used in the spot size measurements for calibration. Each photograph is at 100× magnification and in the same relative scale. Two different scales were imaged for consistency, and the finer scale with the best contrast (the Ronchi ruling) was used to generate the pixel-to- µm scale factor. Where possible, the same photographs were acquired at 400× magnification for better resolution and consistency with the results at 100× magnification.

to- µm scale factor of the imaging system can be inferred. The image of the wire tip is shown in Figure 2.6a, and the lineout of the wire tip is shown in Figure 2.6c. Several lineouts along the wire tip can be averaged to obtain an average value and error; in this case a few pixels of error are introduced as the boundary of the wire is continuous in the lineout. The focusing lens is then adjusted and locked into position for the experiment, and the focused spot size is imaged directly. The original image is shown in Figure 2.6d, the cropped image is shown if Figure 2.6b, and the lineout through the center is shown in Figure 2.6e. Several lineouts can be measured to obtain an average value and error. Error in this procedure arises from uncertainty in the exact width of the wire, uncertainty in locating the exact boundary of the wire from the lineout, and the interpretation of a beam profile which is slightly elliptical. Total error is less than $\pm$ 5 µm, depending on contrast in the various images.

The pyroelectric array camera used to image the 10.6 µm radiation (model PyroCam III from Ophir-Spiricon) has 85×85 µm pixels (effective size of 100×100 µm) in a 124×124 grid, and thus an active area of 12.4×12.4 mm. The nominal spot size of the CO_2 beam is approximately equal to the pixel size of the pyroelectric array camera, therefore the magnification of the imaging system had to be at least $M \approx 10$. In addition, a ZnSe wedge and several CaF_2 disks were utilized to reduce the intensity of the CO_2 beam below the damage threshold of the expensive pyroelectric array camera. The same sequence of images as in Figure 2.6 are repeated in Figure 2.7, but for the case of the spot size measurement of the CO_2 laser in which the $(1/e^2)$ spot size is 80 µm. Although magnification of the imaging system for the CO_2 laser is twice that of the Nd:YAG laser, resolution is decreased because the pixel size of the pyroelectric camera is large as compared to the CCD camera. Additional magnification would reduce image intensity and complicate alignment, consequently $M \approx 10$ was used for the CO_2 imaging system. A consequence of reduced image resolution is additional error, as the boundary of the wire in the lineout is not as sharp as in the lineout from the Nd:YAG imaging system.

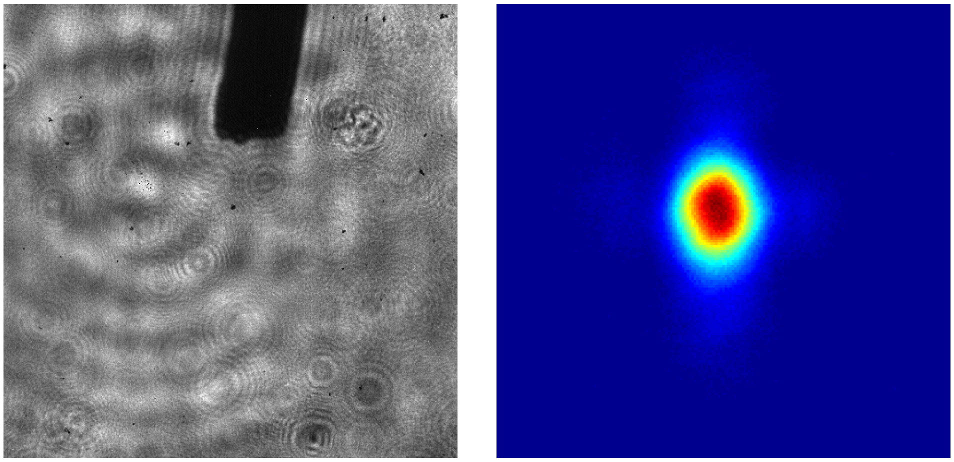

(a) Original image of the wire tip using the laser as the backlighter

(b) Cropped and recolored image of the focused spot size

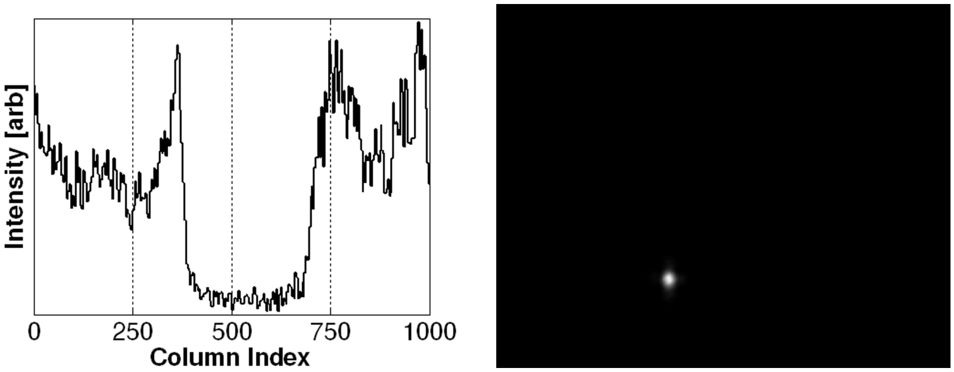

(c) Lineout of the wire tip

(d) Original image of the focused spot size

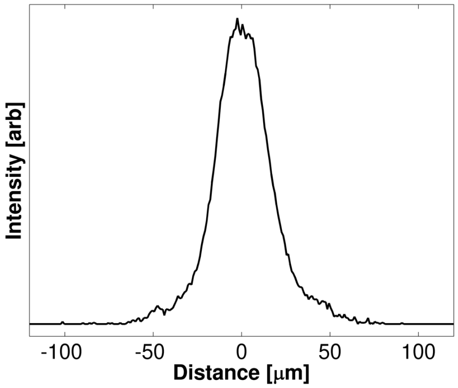

(e) Lineout through the focused spot size

Figure 2.6: Images and lineouts for all important steps in the measurement of spot size for the Nd:YAG laser.

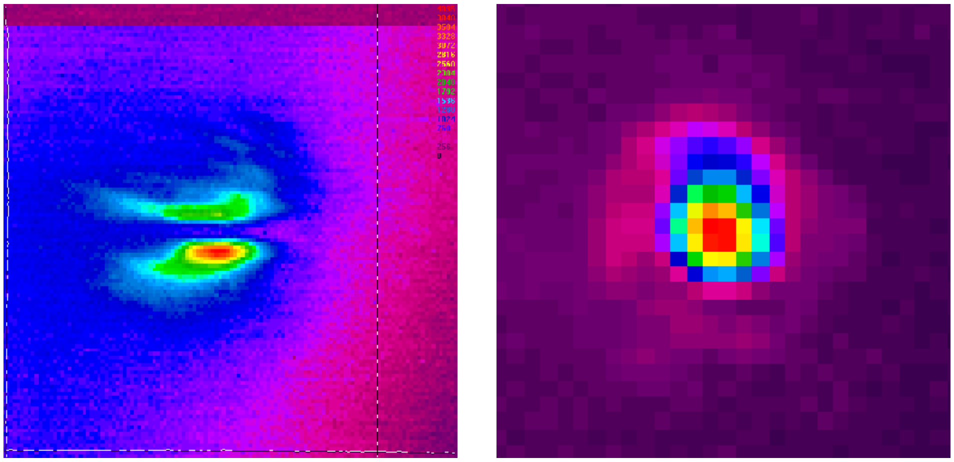

(a) Original image of the wire tip using the laser as the backlighter

(b) Cropped image of the focused spot size

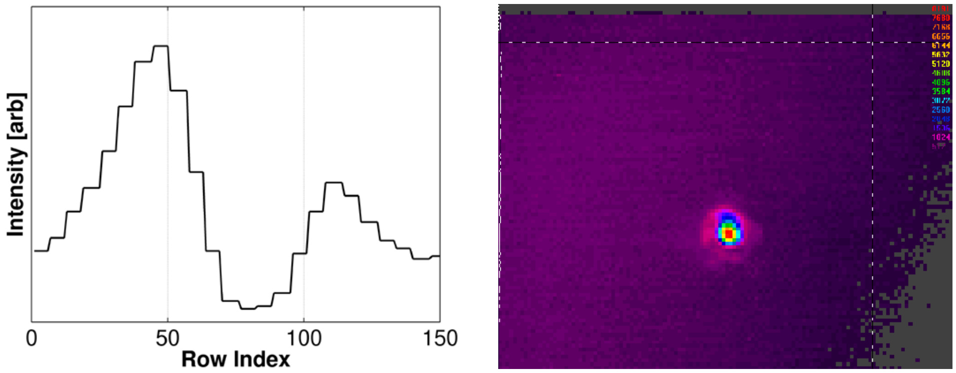

(c) Lineout of the wire tip

(d) Original image of the focused spot size

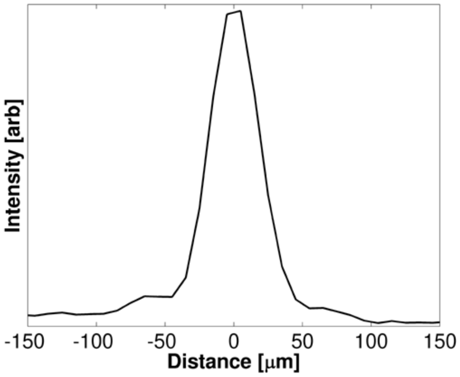

(e) Lineout through the focused spot size

Figure 2.7: Images and lineouts for all important steps in the measurement of spot size for the CO_2 laser.

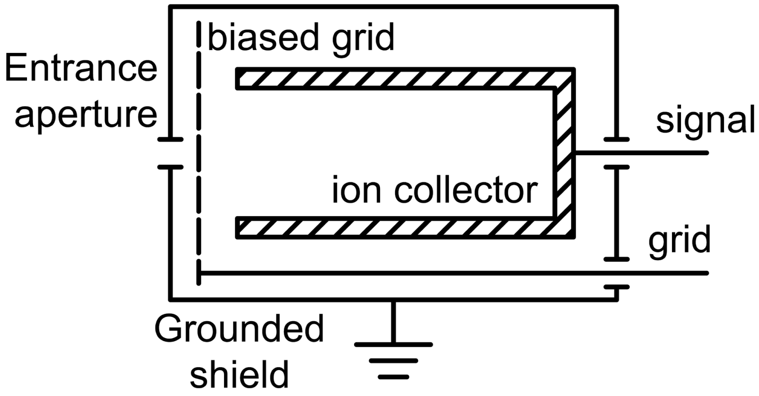

Figure 2.8: Schematic drawing of a Faraday cup.

2.3 Plasma Diagnostics

Several radiation and particle plasma diagnostics were utilized in the experiments. The custom ion probe developed to measure ion energy distributions for each charge state of each ion species will be discussed in Chapter 3. An additional particle diagnostic used in these experiments is a Faraday cup. Radiation plasma diagnostics utilized in these experiments include an extreme ultraviolet calorimeter and an extreme ultraviolet spectrometer.

A Faraday cup is a particle plasma diagnostic which can be electrically biased to measure ion current from a laser produced plasma [39]; a schematic drawing of the type used in these experiments is shown in Figure 2.8. The biased grid between the grounded entrance aperture and the ion collector is used to suppress the effects of secondary electron emission as ions impact the collector. The grid also serves the purpose of separating electrons from ions in the expanding plasma. The grid voltage utilized in all experiments is $-30\,\mathrm{V}$. Two commercial Faraday cups were used in the experiments – a small cylindrical Faraday cup (Kimball Physics FC-71A) that could be mounted inside the vacuum chamber, and a larger Faraday cup (Kimball Physics FC-73A) on a vacuum flange. Complete data processing methods for Faraday cups is given in Woryna, *et al.* [40]; relevant equations are discussed in the subsequent experimental sections.

The extreme ultraviolet (EUV) calorimeter measures the total energy carried by photons in a narrow bandwidth centered at 13.5 nm, over a small solid angle at a distance on the order of 10 cm from the laser plasma source. A schematic drawing

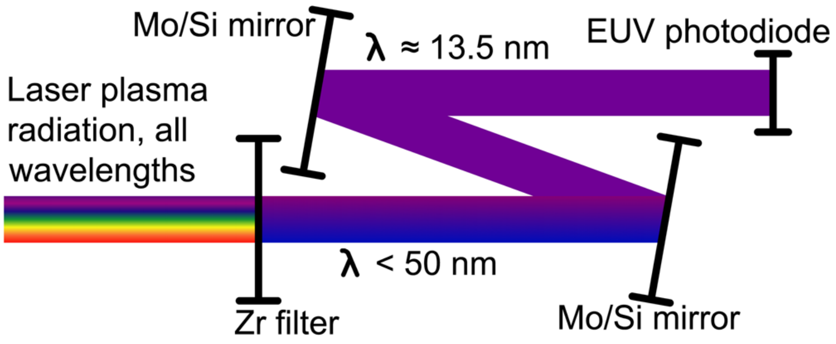

(a) Internal components

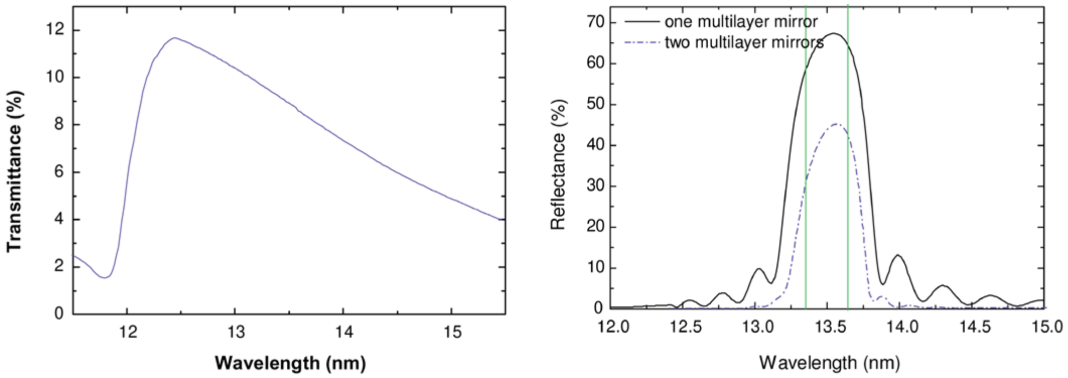

(b) Spectral transmittance of the Zr filter [41]

(c) Spectral reflectance of the Mo/Si mirrors [41]

Figure 2.9: Operation of the EUV calorimeter [41].

of the EUV calorimeter, including the spectral response of its various components, is shown in Figure 2.9.

The EUV calorimeter used in these experiments is a commercial probe (Jenoptik Mikrotechnik E-mon) [41]. The time integration of its temporal response is multiplied by a scale factor supplied by the manufacturer to obtain the local in-band EUV energy measured by the probe. The calculation of conversion efficiency, as defined previously, requires the local EUV energy, the laser energy, which is easily measured real-time, and the angular distribution of EUV radiation into 2π sr. The latter is usually assumed to be isotropic [23], or can be measured experimentally [42], in which case its anisotropic form is revealed. Data processing methods in each case can be found in the corresponding reference; in these experiments the EUV calorimeter was used only for qualitative analysis at different laser conditions.

The EUV spectrometer is a transmission grating spectrometer that measures the time-integrated spectra from 5 to 20 nm with a spectral resolution of $\lambda/\Delta\lambda \approx 160$. It is composed of a vacuum vessel and mount, grating, and x-ray camera. The grating is a 100 nm thick silicon-nitride foil with 10^4 lines/mm. The x-ray camera (Princeton Instruments PI-SX) is a thermoelectrically cooled, back-illuminated CCD camera, with $20 \times 20\,\mu\text{m}$ pixels in a 1340×1300 pixel array. The EUV spectrometer is calibrated in wavelength by looking for intense oxygen lines in the soft x-ray spectrum. It is not absolutely calibrated in intensity and was used only for qualitative measurements under different irradiation conditions; additional details are discussed in the relevant experimental section.

Chapter 3

Design and Realization of an Electrostatic Ion Energy Analyzer

Measurement of the energy distribution for each charge state of each ion species in an expanding plasma is necessary for the design of ion mitigation schemes in the EUV x-ray source application, and necessary for determining the ion yield from a laser ion source. In addition, measurement of the selective acceleration of different charge states and species reveals information about the hydrodynamics and atomic processes occurring within the plasma. Accordingly, a Faraday cup, which records a single energy distribution for all charge states of all ion species, is not an adequate diagnostic to properly study ions from laser produced plasma for the relevant applications. For this purpose, a sophisticated charged particle plasma diagnostic, hereafter referred to as the ion probe, was designed, built, and utilized in the experiments.

3.1 Theory and Literature Review

Several plasma diagnostics exist to measure energy distributions for each charge state of each ion species in an expanding plasma [43] [40]. The common feature is a method to filter ions based on their mass-to-charge state (M/Z) ratio. Single electro- or magnetostatic fields act as a filter at a single M/Z ratio, whereas combined electro- and magnetostatic, or pulsed electric or magnetic fields can be used to record a trace of ions in a plane with varying M/Z ratio dependent on position [44], which inherently

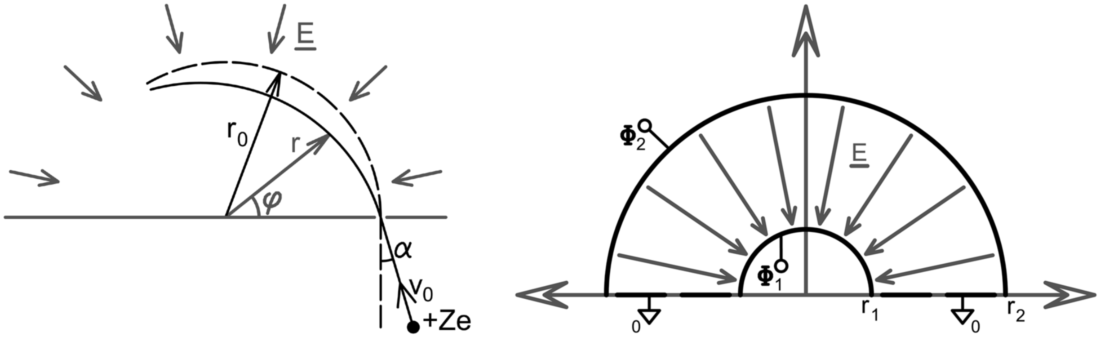

(a) Conceptual schematic of an ion trajectory initially at a small angle to the centerline axis of a radial electrostatic field. Polar coordinates in (r,ϕ) are used. The centerline is defined as the equipotential surface at $r = r_0$. The ion with charge $+Ze$ and initial velocity v_0 enters the field through an aperture at an angle α to the tangent of the $r = r_0$ centerline, normal to the horizontal axis.

(b) Cross-section of concentric cylindrical sectors. The inner cylinder has a radius r_1 and is at a potential Φ_1, the outer cylinder has a radius r_2 and is at a potential Φ_2; for the case of the field shown $\Phi_2 > \Phi_1$.

Figure 3.1: General ion trajectory and electric field configuration for a cylindrical sector ion probe.

requires a detector with spatial resolution. Diagnostics utilizing a single electrostatic field are most commonly employed, as the field is simple to produce, and a single-channel detector can be used. The electric field can be generated between parallel plates, concentric cylindrical sectors, or concentric spherical shells [43]. The latter is inherently difficult to manufacture, and a parallel plate probe provides poor energy resolution as compared to a cylindrical sector probe, which was therefore chosen in the design of the ion probe for these experiments.

The cylindrical sector probe utilizes a radial electrostatic field to filter an ion beam based on its M/Z ratio, as shown schematically in Figure 3.1. The electric field, E, is generated by concentric cylindrical sectors and is proportional to the inverse radius, $E = -A/r$ where A is a constant dependent on the radii and potential of the cylinders. For the configuration shown in Figure 3.1b,

$$A = \frac{\Phi_2 - \Phi_1}{\ln(r_2/r_1)}. \tag{3.1}$$

The simplest ion trajectory is along the equipotential surface $r = r_0$, i.e., when $\alpha = 0$.

In this case, the equation of motion for the ion can be solved analytically,

$$\frac{Mv^2}{r} = \frac{Ze(\Phi_2 - \Phi_1)}{r\ln(r_2/r_1)}, \tag{3.2}$$

where M is the ion mass, and v is the constant ion velocity, $v = L/TOF$, where L is the distance from the ion source to the ion detector, and TOF is the time-of-flight of ions from the source to detector. Accordingly, the M/Z ratio can be calculated,

$$\frac{M}{Z} = \frac{Ze\,(\Phi_1 - \Phi_2)}{L^2\ln(r_2/r_1)}(TOF)^2, \tag{3.3}$$

or, alternatively, the kinetic energy to charge state ratio, KE/Z, can be calculated,

$$\frac{KE}{Z} = \frac{e\,(\Phi_1 - \Phi_2)}{2\ln(r_2/r_1)}. \tag{3.4}$$

As a result, ions which travel along the centerline will have a constant KE/Z ratio dependent on probe geometry and applied voltage to the electrodes; all other ions will deviate from this path.

If a grounded output aperture is positioned along the equipotential surface, for $\phi > 0$, ions with the exact KE/Z ratio will exit the aperture. Of practical interest, however, is the energy resolution, $\Delta KE/KE$, determining the range of ion energies which exit the output aperture. To solve for the resolution, the trajectory of an ion at a small angle to the centerline and with an arbitrary velocity must be calculated. Equations of motion for the r-trajectory and ϕ-trajectory of the ion are given by,

$$\begin{gathered}\frac{d^2r}{dt^2} - r\left(\frac{d\phi}{dt}\right)^2 = -\frac{ZeA}{Mr} \\ \frac{d}{dt}\left(r^2\frac{d\phi}{dt}\right) = 0\end{gathered} \tag{3.5}$$

subject to the following initial conditions at $t = 0$,

$$\begin{aligned} r &= r_0 \\ \phi &= 0 \\ v_r &= -v_0\sin\alpha \\ v_\phi &= v_0\cos\alpha \end{aligned} \tag{3.6}$$

This problem cannot be solved analytically, however the r-trajectory can be computed approximately in orders of the small parameter α [45],

$$r(\phi,\alpha,r_0) = r_0\left(1-\frac{\alpha}{\sqrt{2}}\sin\left(\phi\sqrt{2}\right)\right)+r_0\sum_{i=2}^{N}\alpha^i f_i(\phi) \tag{3.7}$$

in which terms to first order in α are given explicitly, and terms up to $N=3$ are given in Kozlov and Strivhenko [45]. The solution for the r-trajectory of an ion with the same energy at the opposite initial angle is the same, where α is replaced by $-\alpha$. Accordingly, trajectories of ions incident at $\pm\alpha$ to the centerline with the same energy will intersect where $\sin\left(\phi\sqrt{2}\right)=0$, i.e., when $\phi=127^\circ$. A diagram of these trajectories, calculated with accuracy to three orders in α [45], is shown in Figure 3.2a. Finally, if an output aperture of width Δs is positioned at $\phi=127^\circ$, the resolution will be

$$\frac{\Delta KE}{KE}=\frac{\Delta s}{r_0}+\frac{2}{3}\alpha^2. \tag{3.8}$$

The same problem can be solved numerically. For this purpose, the commercial software package Simion was used to calculate the ion trajectories. Simion solves for the potential due to an arbitrary electrode configuration, and then solves for the motion of charged particles within the field. Figure 3.2b is a Simion screen shot showing the ion trajectories with the same initial conditions used for the trajectories in Figure 3.2a. Figure 3.2c compares the trajectories computed by Simion with the approximate solutions to three orders in α. The numerical solution reproduces the trajectories from the approximate solution, with error on the order of $r_0\alpha^3$, and therefore Simion is used for additional analysis of the ion probe.

Due to the refocusing effect at $\phi=127^\circ$, the angle subtended by the cylindrical sector electrodes in many probes described in the literature is the same [46] [47] [48]. Angles less than or greater than 127° will adversely impact the probe resolution, however, probes with 90° subtended by the cylindrical sector electrodes are easiest to manufacture, mount, and align. Accordingly, several probes at this angle have also been described in the literature [40] [49] [50], and a 90° probe was chosen for these experiments. In this case, though, analytical expressions for the resolution are not available, and a numerical investigation of ion trajectories over a range of energies and incidence angles must be used to determine the resolution.

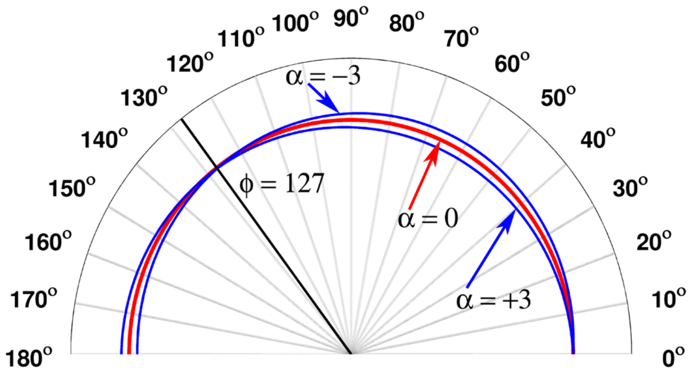

(a) Analytical trajectories calculated using the solution to Eqn. (3.5) accurate to three orders in α

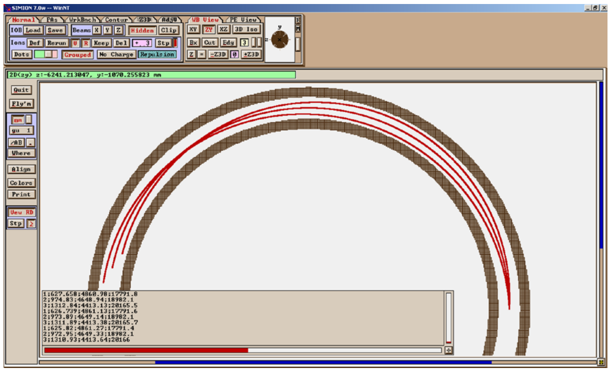

```
2D(zy) z:-6241.213047, y:-1070.255823 mm
```

```
1;627.658;4860.98;17791.8
2;974.83;4648.94;18982.1
3;1312.84;4413.13;20165.5
1;626.739;4861.13;17791.6
2;973.89;4649.14;18982.1
3;1311.89;4413.38;20165.7
1;625.82;4861.27;17791.4
2;972.95;4649.33;18982.1
3;1310.93;4413.64;20166
```

(b) Screen shot of a Simion simulation showing the same trajectories as in Figure 3.2a

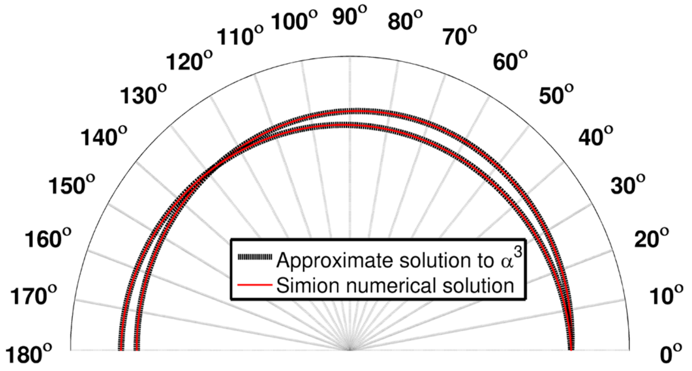

(c) Comparison of ion trajectories from the analytical and numerical solutions.

Figure 3.2: Analytical and numerical ion trajectories at initial angles of $\alpha = 0$ and $\alpha = \pm 3$ with respect to the centerline

Table 3.1: Physical dimensions chosen for the design of the ion probe. The geometric factor appears in the formula for the KE/Z ratio of the probe [Eqn. (3.4)].

Parameter	Value
Deflection angle [degree]	90
Radius of outer electrode [cm]	10
Radius of inner electrode [cm]	9
Mean electrode radius [cm]	9.5
Geometric factor $= [2\ln(r_2/r_1)]^{-1}$	4.75
Diameter of input aperture [mm]	0.1
Diameter of output aperture [mm]	2
Distance from source to input aperture [cm]	100
Distance from output aperture to ion detector [cm]	10
Maximum angle of incidence of ions [degree]	0.03

3.2 Design

To first order, the resolution of the ion probe will be $\Delta KE/KE = \Delta s/r_0$, where Δs is the width of the output aperture and r_0 is the mean radius of the cylindrical sector electrodes. This motivates the selection of a physically large probe with a small output aperture. Conversely, signal level scales with the output aperture size, and the physical size of the probe obviously impacts its complexity to manufacture, mount, and align. Dimensions for the ion probe were chosen with these tradeoffs in mind, in addition to available information on dimensions of similar probes described in the literature [40] [49] [50]; Table 3.1 summarizes the dimensions chosen for the ion probe.

The resolution of the probe, to first order, will therefore be $KE/\Delta KE = 48$. Additional effects, such as the deviation from the centerline of ions incident at small angles, and fringe fields near the entrance and exit apertures, can adversely affect the probe resolution. To calculate the actual resolution, the geometry of the probe from source to detector was input into Simion for numerical experimentation. For reasons discussed subsequently, the probe is mounted approximately 100 cm from the laser plasma source, and the detector is mounted approximately 10 cm from the output aperture. The com-

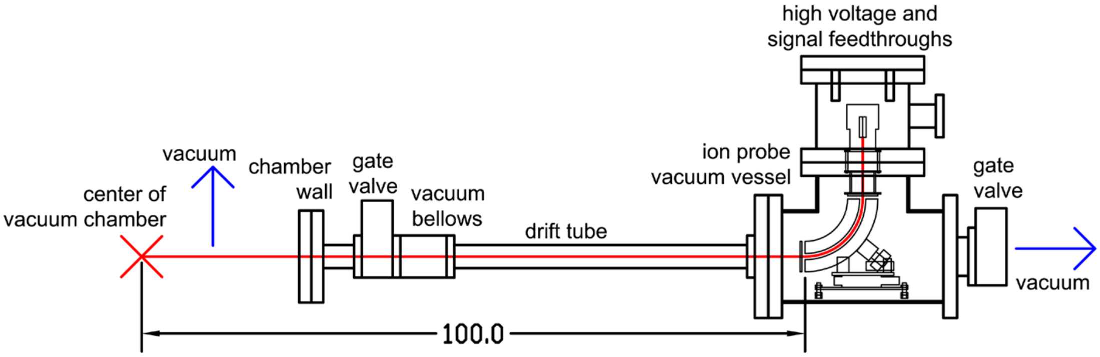

(a) Geometry of ion probe and vacuum vessel in CAD format, dimensions in cm.

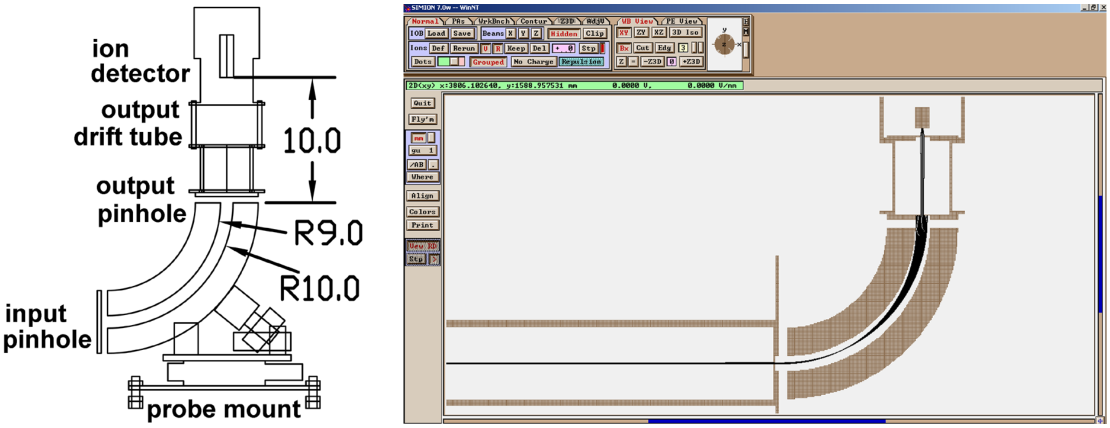

(b) Geometry of ion probe in CAD format, dimensions in cm.

(c) Simion simulation of ion trajectories

Figure 3.3: The exact geometry of the ion probe, from source to detector, as used to determine the probe resolution.

plete cross-sectional probe design is shown in Figures 3.3a and 3.3b in CAD format, and in Figure 3.3c the geometry has been imported into Simion.

The resolution determined by numerical simulation is $KE/\Delta KE = 45.7$, which is 95% of the upper limit. The maximum angle of incidence of ions at the input pinhole is 0.03°, and resolution is affected negligibly due to this effect. Fringe fields near the probe input and output also affect the resolution negligibly. This can be understood by plotting the electric field in the exact geometry of the probe; the commercial simulation package Maxwell 2D is used for this purpose with results shown in Figure 3.4. The only effect lowering resolution is the non-optimal deflection angle of the probe, however the effect is minimal. Finally, the resolution can also be impacted by space charge effects, as discussed subsequently.

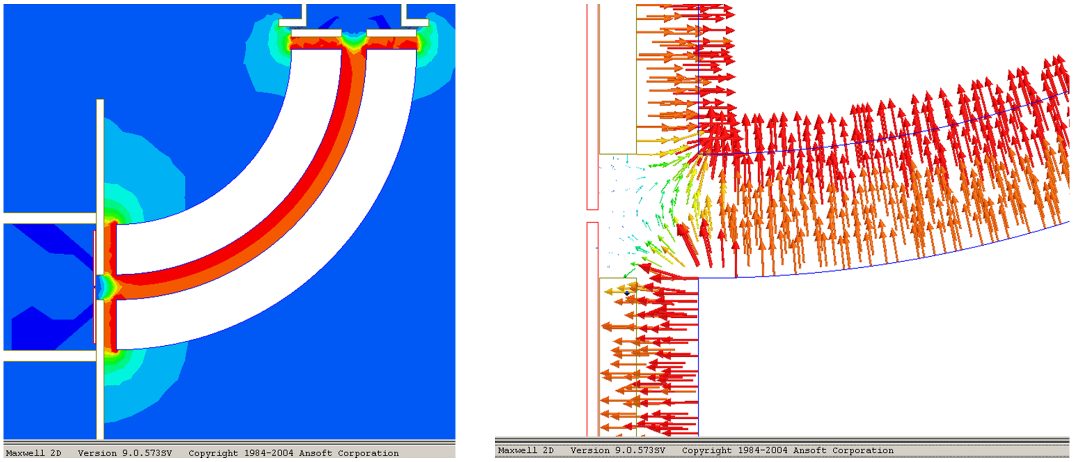

(a) Magnitude of the field, where the scale extends over four orders of magnitude.

(b) Zoomed-in view of the field vectors close to the input pinhole.

Figure 3.4: Two dimensional plots of the electric field within the ion probe geometry, calculated and plotted using Maxwell 2D. Clearly, all fringe fields in the path of the ions are negligible as compared to the radial electrostatic field, and thus energy distortion by fringe fields will be negligible.

The requirement to mount the ion probe 100 cm from the laser plasma source is due to an upper limit on ion density, n_i, at the probe input aperture imposed by two physical considerations. First, electrons and ions in the expanding plasma must be separated, which can be achieved if the applied field is greater than the electric field due to charge separation, i.e., if

$$\frac{\Delta\Phi}{\Delta r} \gg 4\pi Zen_i d_i, \tag{3.9}$$

where $\Delta\Phi$ is the applied voltage between the electrodes, Δr is their spacing, and d_i is the diameter of the input pinhole. Accordingly, the upper limit on ion density becomes

$$\left(\frac{n_i}{\mathrm{cm}^{-3}}\right) \ll \frac{\left(6\times 10^9\right)\left(\Delta\Phi/\mathrm{V}\right)}{\left(\Delta r/\mathrm{cm}\right) Z \left(d_i/\mu\mathrm{m}\right)}. \tag{3.10}$$

An additional physical consideration imposing an upper limit on ion density is the effect of space charge expansion on the ion beam within the cylindrical electrodes. It can be shown that an ion beam with geometry described in Figure 3.5 will expand radially according to the relation [51]

$$w_1 = \left(\frac{n_i Z^2 4\pi e^2}{KE}\right)^{1/2} s_1 w_0. \tag{3.11}$$

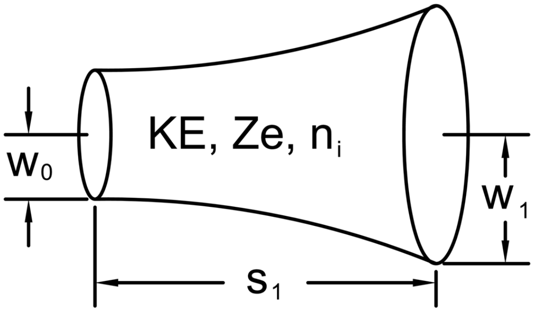

Figure 3.5: Space charge expansion of an ion beam with kinetic energy KE, charge Ze, and ion density n_i, from an initial radius w_0 to a final radius w_1, over a distance s_1.

If the probe resolution is not to be affected by space charge effects, then w_1 must be set to output aperture radius, w_0 to the input aperture radius, and s_1 to the path length along the centerline, $\pi(r_1+r_2)/2$. Accordingly, the upper limit on ion density becomes

$$\left(\frac{n_i}{\mathrm{cm}^{-3}}\right) < (2\times10^5)\left(\frac{d_o}{d_i}\right)^2\left(\frac{r_1+r_2}{\mathrm{cm}}\right)^{-2}\frac{(\Delta\Phi/\mathrm{V})}{Z\ln(r_2/r_1)}. \tag{3.12}$$

In order to ensure the two limits on ion density are not exceeded, the spatial decay of density must be determined. An adiabatic model of expansion can be used, in which

$$n_e(r) = n_{e0}\,(r/r_0)^{-3}, \tag{3.13}$$

where r is the distance from the laser plasma source, r_0 is the initial plasma size, and n_{e0} is the initial plasma density. Typical parameters relevant to the experiments discussed within are $n_{e0} \approx 10^{20}\,\mathrm{cm}^{-3}$ and $r_0 \approx 100\,\mu\mathrm{m}$. As a result, the electron density will decay to approximately $10^8\,\mathrm{cm}^{-3}$ after 100 cm of expansion.

The maximum electron density ($n_e = Zn_i$) imposed by the electron-ion separation condition ([Eqn. (3.10)]) is $6\times10^8\,\mathrm{cm}^{-3}$, using the parameters from Table 3.1 and $\Delta\Phi = 10\,\mathrm{V}$ (the minimum voltage used in the experiments). Electron density decays more rapidly than predicted by the adiabatic model, however, as electrons are also lost through recombination in the early phase of expansion. As a result, the electron-ion separation condition ([Eqn. (3.10)]) will be satisfied.

The maximum ion density imposed for negligible effects due to space charge expansion ([Eqn. (3.12)]) correctly represents only the density of ions filtered by the probe. An estimate of the fractional ion density which is filtered depends on the KE/Z ratio,

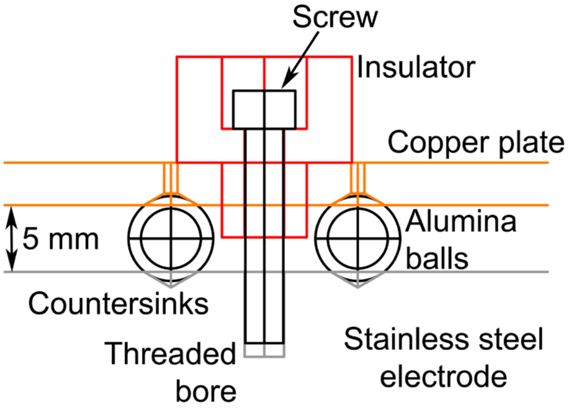

Figure 3.6: Manufacturing technique used to isolate two components electrically, but join them mechanically in a very rigid and precise manner. The stainless steel electrode can be held at a potential with respect to the copper plate.

total ion energy distribution, and probe resolution. In these calculations, a conservative estimate of 1% was used, which effectively raises the constant in Eqn. (3.10) by two orders of magnitude if n_i is to be interpreted as total ion density. In this case, the maximum electron density is then $2 \times 10^9\,\mathrm{cm}^{-3}$, using the parameters from Table 3.1 and $\Delta\Phi = 10\,\mathrm{V}$, and thus the condition for negligible space charge expansion ([Eqn. (3.12)]) will be satisfied.

3.3 Fabrication

The primary challenge in fabrication of the probe was isolating the various components electrically, but connecting them mechanically in a very rigid and precise manner. A manufacturing technique common in charged particle optics [52], illustrated in Figure 3.7, was utilized for precise alignment of all electrodes and ground plates. In addition, a steel rod with a calibrated 1 cm diameter was used to verify the gap spacing of the cylindrical electrodes; error in the 1 cm gap is less than $\pm 50\,\mu\mathrm{m}$.

The spacing between the ground plates and electrodes is 5 mm. It is well known that millimeter gaps in vacuum can support tens of kilovolts [53], which is much greater than the typical voltages used in the experiments (10 to 1000 V). The specific gap spacings were chosen to simplify fabrication and achieve the requisite electric field configuration.

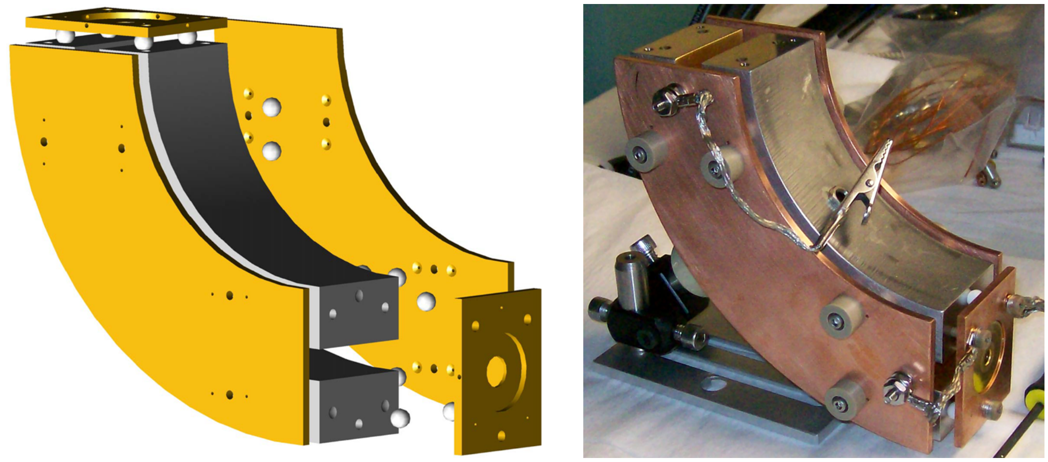

(a) CAD rendering of ion probe. (b) Photograph of assembled ion probe.

Figure 3.7: Assembled ion probe.

The probe electrodes were fabricated from stainless steel 304, a nonmagnetic alloy. The surfaces of the stainless steel electrodes were coated with a thin layer of gold, chosen for its inert properties, in order to ensure that nonconducting oxide films do not distort the electric field. Indeed, other authors have discussed the problem of field distortion by surface charge on oxide films, including gold-plating as a solution [50]. The ground plates surrounding the probe electrodes were fabricated from oxygen free high-conductivity copper, a common material for charged particle optics [52]. Finally, ground alumina balls were used as insulators between all conducting surfaces. A CAD rendering and a photograph of the assembled cylindrical electrodes, alumina insulators, and ground plates are shown in Figure 3.7

3.4 Installation and Alignment

The requirement to align the 100 μm input aperture to a laser plasma source 100 cm away, itself with sub-millimeter dimensions, is a very challenging mechanical problem. Complicating the problem even more is the weight of the ion probe, approximately 4 kg, which renders it incompatible with many commercial optical mounts. Finally, the radius of the vacuum chamber in which the target resides is less than 30 cm, therefore a separate vacuum vessel for the ion probe connected by a drift tube to the target cham-

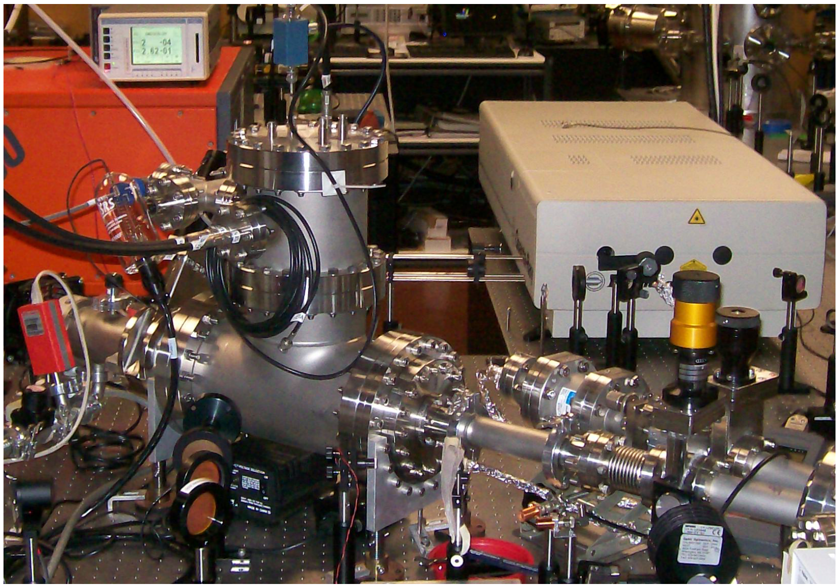

Figure 3.8: Photograph of vacuum components for the ion probe.

ber is required. The arrangement of vacuum components was illustrated previously in Figure 3.3a, and Figure 3.8 is a photograph of the complete vacuum system.

Proper alignment of the ion probe requires 10 μm accuracy along the X and Y axes, and 0.1° accuracy in the YZ and XZ planes, as defined in Figure 3.9. Alignment accuracy along the Z axis can be a few millimeters, and in the XY plane can be a few degrees. Due to limited physical space within the ion probe vacuum vessel, a single micrometer stage could be installed, as shown in Figure 3.10a. The stage was chosen for rotational adjustment in the XZ plane, and methods to align the probe in all other degrees of freedom had to be accomplished by other methods, as discussed subsequently.

The first step in the alignment process is to install the ion probe vacuum vessel on the optical table the correct distance from the target chamber. Thin wire is then installed as centered cross hairs on both sides of the vacuum vessel, and a He:Ne alignment laser is positioned from the target chamber center through both crosshairs, as seen in Figure 3.10a. The entire vacuum vessel can be adjusted in two rotational degrees of freedom, in the YZ and XY planes, as it is installed on four legs which move independently on ball bearings, i.e., the entire vacuum vessel is itself a two-axis goniometer. The probe mount, which connects to the rotation stage in Figure 3.10a, is shown in Figure 3.10b. When connected directly to each other, the probe input aperture is designed

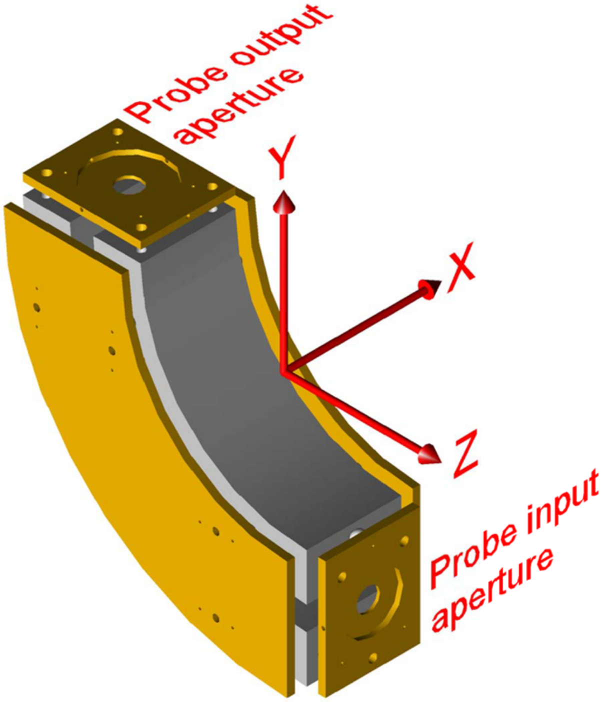

Figure 3.9: Axes used to define degrees of freedom for probe alignment.

to be a few millimeters too low along the Y axis. Metal shims with thickness as low as 25 µm are added to make up the difference until the desired position along the Y axis is achieved. In addition, clearance holes, as shown in the red circle in Figure 3.10b, are oversized for $\frac{1}{4}''$ screws, so that the entire probe can be translated along the X axis to achieve the desired position. Usually, following slight adjustments along the X axis, the probe had to be adjusted again in the XZ plane with the micrometer stage. As a verification of proper alignment, the intensity of the He:Ne alignment beam reaches a maximum as viewed through the output aperture. In addition, when the input pinhole is replaced by a mirror, the He:Ne alignment beam is reflected back to its source.

3.5 Calibration and Sample Data

Sample data from the ion probe in its final configuration is shown in Figure 3.11a. Of course, earlier configurations of the ion probe, without all of the complexities in design, fabrication, and alignment discussed previously, generated data that was either excessively noisy, as shown in Figure 3.11b, or otherwise incomprehensible. In the case

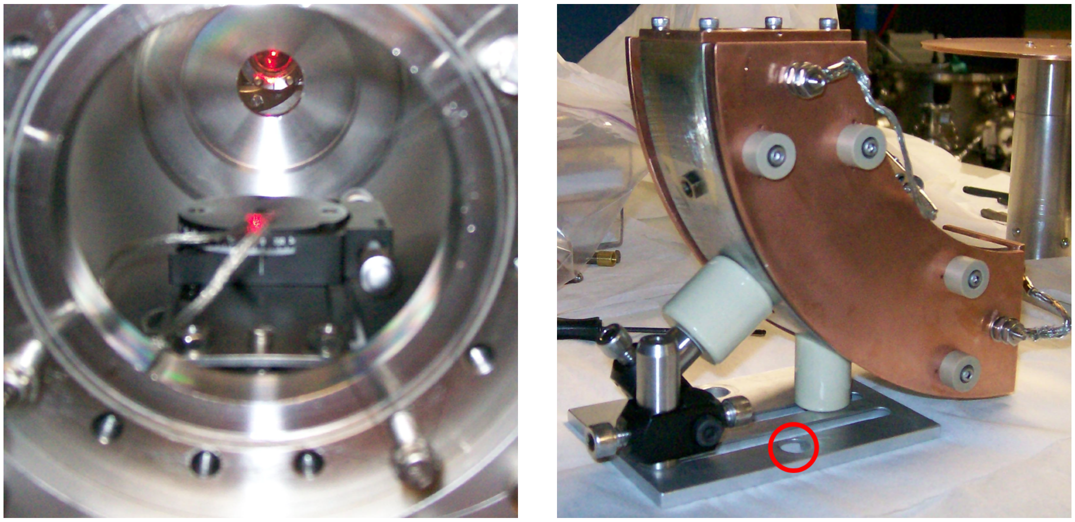

(a) Photograph from rear of the ion probe vacuum vessel. The micrometer stage for adjustment in the XZ plane is shown, and the He:Ne alignment laser is shown intersecting the target chamber center and crosshairs positioned at the center of each side of the ion probe vacuum vessel.

(b) Photograph of the ion probe mount. The clearance hole in the red circle is oversized for $\frac{1}{4}''$ screws, as necessary for alignment along the X axis.

Figure 3.10: Photographs of the vacuum vessel and the probe mount to illustrate the alignment procedure.

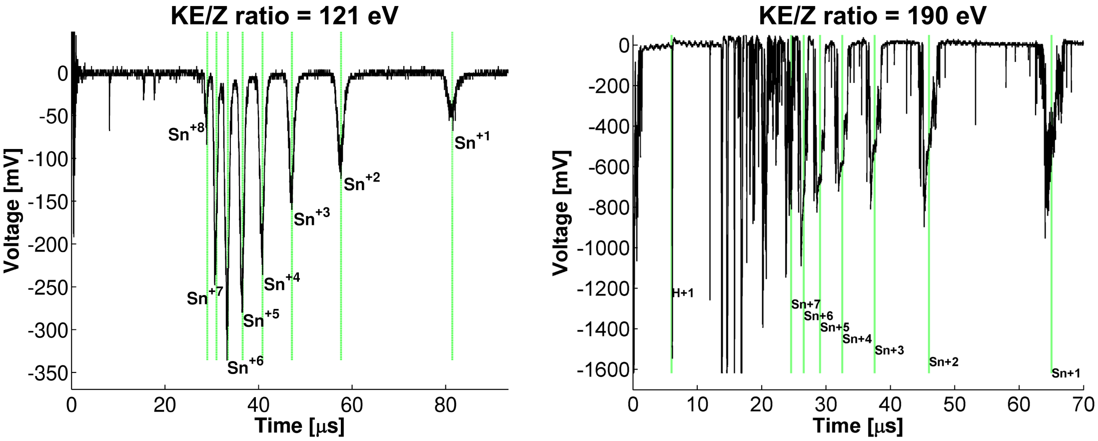

(a) Final sample data from the ion probe, in which primary sources of noise have been removed.

(b) Sample data from the ion probe when significant noise due to secondary electron effects is present.

Figure 3.11: Sample time-of-flight data from the ion probe.

of the data shown in Figure 3.11b, the ion detector was mounted only millimeters from the output aperture of the ion probe. In the interaction of ions not filtered by the probe with the walls of the ion probe, copious secondary electrons are generated, and some of those exit the output aperture and are recorded by the ion detector; this is the source of noise in Figure 3.11b. When the ion detector is separated from the output aperture by 10 cm, the secondary electrons deviate from the probe centerline path and the noise disappears, as seen in Figure 3.11a. Indeed, other authors who have published precise dimensions of similar ion probes find it necessary to separate the ion detector from the probe output aperture by several centimeters [49]. Other issues adversely affecting the quality of data from the ion probe were numerous, however all were resolved and not discussed further.

The horizontal axis in Figure 3.11 represents the time-of-flight (TOF) of ions from the laser plasma source to the detector, given by

$$TOF(Z) = d\sqrt{\frac{M}{2(KE/Z)Z}} \tag{3.14}$$

where the source to detector distance, d, the ion mass, M, and the KE/Z ratio are all constant. Accordingly, if ions with varying charge state, Z, are present in the expanding plasma, then groups of ions with the same KE/Z ratio, but different charge state, arrive at the detector at different times. Prior to any experimentation, times at which ions of different species and different charge state are expected to arrive can be calculated; the vertical green lines in Figure 3.11a represent calculated times for up to 8-times ionized Sn atoms. The multiple peaks preceding the arrival of all Sn ions represent the arrival of light ions from an ablated impurity layer on the surface of the target. This layer typically consists of H, He, C, N, and O atoms, and the precise composition can be calculated with the ion probe.

The vertical axis in Figure 3.11 represents the voltage across a $50\,\Omega$ oscilloscope load from a preamplifier connected at the output of the ion detector. For all experiments, a single channel electron multiplier (Burle Channeltron 4860), and a low noise preamplifier designed for use with ion detectors [54], were used. The relative differences in the amplitudes of each peak in Figure 3.11a do not imply the same relative differences in some ion property. Rather, each peak has to be scaled pursuant to a detection efficiency, γ, for the energy at which the ion is detected. The detection efficiency is an inherent property of the single channel electron multiplier (CEM), as described in the schematic of the physical operation of the CEM shown in Figure 3.12a.

From the description of the physical operation of the CEM, the importance of the detection efficiency becomes apparent. Each peak in Figure 3.11a represents the arrival of ions with the same KE/Z ratio, but varying Z and therefore varying kinetic energy. Without knowledge of the detection efficiency at each of the requisite ion energies, the relative differences in the amplitudes of each peak as seen in Figure 3.11a would imply nothing meaningful. Therefore, a reliable determination of detection efficiency in parameter space of the present experiments (Sn ions with energies up to several keV) is critical.

The most reliable method to determine detection efficiency is by direct measurement for each specific detector, as previous studies have shown variability due to geometry, manufacturing processes, and handling [55]. Detection efficiency is measured by recording the number of output pulses from a CEM, and the number of incident ions. The latter can be recorded with a faraday cup connected to an electrometer with pA resolution, in place of the CEM [55] [56] [57] [58]. However, to infer number of ions from a Faraday cup measurement, a monatomic source of ions of a single charge state

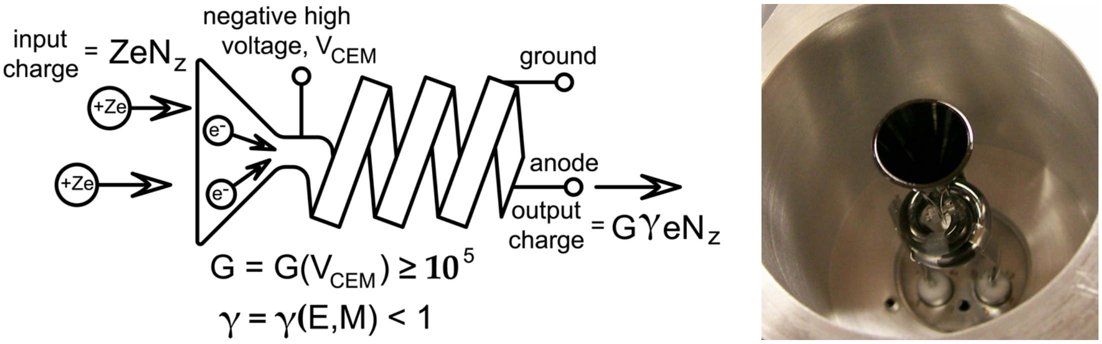

(a) Physical operation of the CEM

(b) Photograph of the CEM

Figure 3.12: Schematic and photograph of the channel electron multiplier (CEM). Multiply charged ions are incident at the input of the CEM, each with a charge $+Ze$, where e is the electron charge. The inner walls of the CEM are coated with a material having a high secondary electron emission coefficient. The interaction of the incident ion with the inner wall generates several secondary electrons. The numerous subsequent interactions of those secondary electrons as they propagate along the helical path of the CEM amplify the initial number of secondary electrons by many orders of magnitude. The source of additional electrons in this process is a high voltage applied to the CEM, and the gain therefore depends on this high voltage, V_{CEM}. If the input charge is ZeN_Z, where N_Z is the number of ions with charge state Z, the output charge from the CEM will be $G\gamma eN_Z$, where G is the gain which depends on V_{CEM}, and γ is a detection efficiency, which quantifies the response of the CEM as a function of the incident ion properties, specifically energy and mass. The gain of a CEM is typically greater than 10^5, whereas detection efficiency is less than unity.

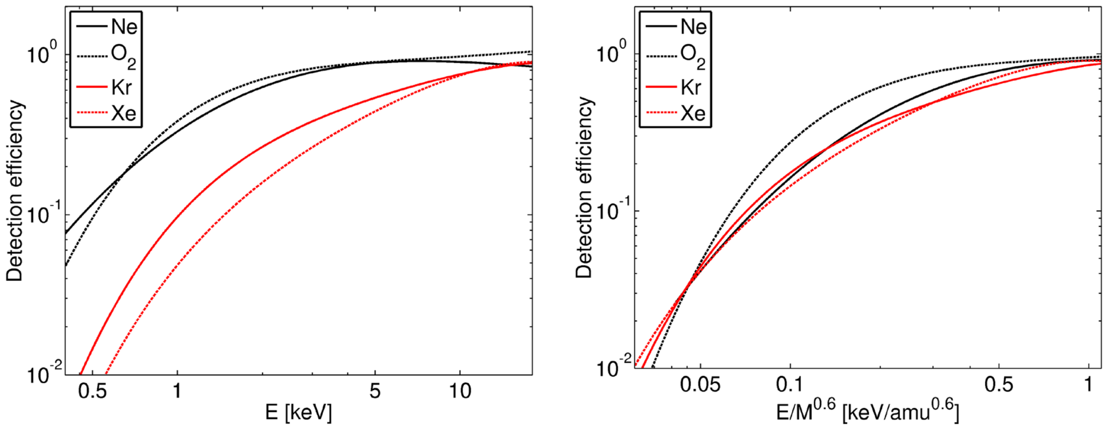

(a) Detection efficiency as a function of ion energy (b) Detection efficiency as a function of $E/M^{0.6}$

Figure 3.13: Detection efficiency for Ne, O_2, Kr, and Xe ions as measured by a new Burle Channeltron 4860 ion detector [58].

is required, rather than a laser produced plasma source, which generates several charge states of several ionic species.

A recent measurement and review of detection efficiencies by Krems, *et al.* compares new data for various multiply-charged ions with previously available data in similar parameter space [58]. Several detectors are utilized, including a new CEM of the same model used in the present experiments (Burle Channeltron 4860). In addition to replicating previous data by other authors [55] [56] [57], the database by Krems, *et al.* extends to multiply-charged heavy ions with atomic mass close to that of Sn (Kr and Xe), and with energies from 250 eV to 25 keV, which overlap the expected ion energies of the present experiments. Detection efficiencies for Ne, O_2, Kr, and Xe ions, as recorded with the same model CEM used in the present experiments, are shown in Figure 3.13. In Figure 3.13a, the horizontal axis is ion energy, however, when plotted against $E/M^{0.6}$, where E is ion energy, and M is ion mass, the detection efficiencies for heavy ions scale to a single curve, as shown in Figure 3.13b. Accordingly, because the mass dependence for heavy ions is empirically understood, and because new detectors of the same model are used by Krems, *et al.* and in the present experiments, the detection efficiency data in Krems, *et al.* are scaled for Sn ions and used in the present data analysis.

An important consequence of the data in Figure 3.13a is that detection efficiency for heavy ions becomes greater than approximately 50% only when ion energies are at least a few keV. A significant fraction of ions generated in the relevant applications have energies of just hundreds of eV. Accordingly, these ions are accelerated across a potential difference of several kV immediately before detection by the CEM. In practice, a grounded aperture is installed a few mm before the entrance aperture of the CEM, itself biased to a negative high voltage. The total energy of ions in eV at the CEM entrance aperture is then

$$E_{ion} = \left(\frac{KE}{Z}\right)Z + |V_{CEM}|, \tag{3.15}$$

where V_{CEM} is typically set to $-2\,\mathrm{kV}$ for the experiments, chosen so that detection efficiency is close to 50% for the lowest energy ions.

The effect of pre-acceleration of ions to high energies immediately before detection is a reduction in the overall TOF of ions from source to detector. For most of the source to detector distance, the ions drift in either a field-free region, or within the cylindrical electrodes where the field is always normal to ion velocity. The TOF within these regions is given by

$$TOF_{drift} = L_{drift}\sqrt{\frac{M}{2E}}, \tag{3.16}$$

where L_{drift} is the total distance from the laser plasma source to the aperture in front of the CEM. The time-of-flight of ions in the acceleration region is the positive root of the polynomial equation

$$\left(\frac{ZeV_{CEM}}{2Md}\right)TOF_{accel}^{2} + \sqrt{\frac{2E}{M}}TOF_{accel} - d = 0, \tag{3.17}$$

where d is the separation distance of the accelerating gap. If the time-of-flight in the acceleration region were calculated as if it were a drift region, error as high as 1 μs would be introduced, dependent on ion properties. The total TOF is the sum within the drift and acceleration regions,

$$TOF = TOF_{drift} + TOF_{accel}. \tag{3.18}$$

3.6 Data Analysis

In order to record the complete distribution of ion energies and charge states using the ion probe, the experiment must be repeated several times as the KE/Z ratio is scanned by varying the high voltage applied to the probe electrodes. In practice, approximately 30 experimental repetitions are required to generate the requisite time-of-flight data set. Following data acquisition, the ion energy distribution, $dN_{\alpha,Z}/dE$ as a function of E, where $N_{\alpha,Z}$ is the number of ions of species α and charge state Z, and E is ion energy, is calculated in the following procedure.

The voltage measured by the oscilloscope, hereafter referred to as $v(t)$, is first divided by the amplification from the low noise preamplifier, G_A, to recover the voltage generated by the ion detector. The output charge, q_{OUT}, from the ion detector is described by

$$d\left(q_{OUT}\right) = \frac{v(t)/G_A}{R_S}dt, \tag{3.19}$$

where R_S is the oscilloscope resistance $(50\,\Omega)$. The relation of output charge to input charge for the ion detector has previously been described, so that Eqn. (3.19) can be rewritten as

$$d\left(G\gamma e N_Z\right) = \frac{v(t)/G_A}{R_S}dt. \tag{3.20}$$

Because the CEM gain and detection efficiency do not vary with time, it follows that

$$\frac{dN_Z}{dt} = \frac{v(t)/G_A}{R_S G\gamma e}. \tag{3.21}$$

Furthermore, the time-of-flight as a function of ion kinetic energy is known in analytical form [Eqn. (3.18)], so that its derivative can be calculated,

$$\frac{dt}{dE} = \frac{d}{dE}\left(TOF_{drift}\right) + \frac{d}{dE}\left(TOF_{accel}\right). \tag{3.22}$$

Finally, the quantity of interest is the ion energy distribution, dN_Z/dE, calculated as

$$\frac{dN_Z}{dE} = \frac{dN_Z}{dt}\frac{dt}{dE} = \frac{v(t)/G_A}{R_S G\gamma e}\frac{dt}{dE}. \tag{3.23}$$

From the above equations, an ion energy distribution can be calculated from numerous time-of-flight waveforms as the KE/Z ratio is scanned. A sample ion energy distribution is shown in Figure 3.14.

3.7 Sources of Measurement Error

Measurement error in the ion energy distribution is a result of the propagation of error in several variables involved in the data analysis procedure. In general, the error in

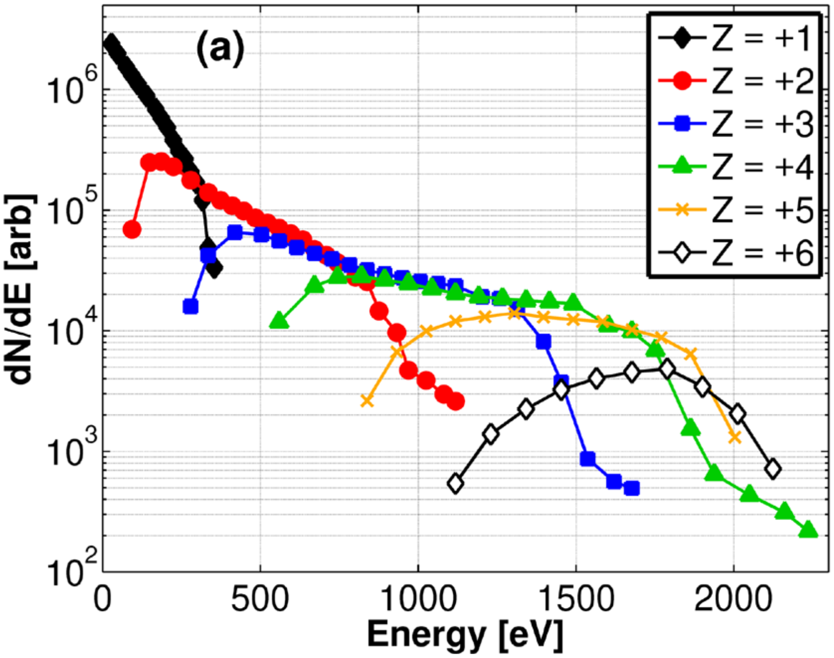

Figure 3.14: Sample ion energy distribution for Sn ions. In this example, six charge states of Sn ions were present in the data analysis.

a multi-variable function depends on the error in each of its variables. For example, if the variables x and y have error expressed by

$$\begin{aligned} x &= x \pm \delta x \\ y &= y \pm \delta y \end{aligned} \tag{3.24}$$

then the error in the multi-variable function $f(x,y) = f(x,y) + \delta f(x,y)$ will be [59]

$$\delta f(x,y) = \sqrt{\left(\frac{\partial f}{\partial x}\delta x\right)^2 + \left(\frac{\partial f}{\partial y}\delta y\right)^2}. \tag{3.25}$$

The KE/Z ratio of the ion probe depends upon the applied voltage and the ratio of radii of the cylindrical electrodes. Precise measurements of the radii were made by scanning the assembled probe directly and importing the to-scale image into CAD software. Using this technique, the radius of the inner electrode is determined to be 9.027 cm, the radius of the outer electrode is 10.029 cm, and errors in radius determined by multiple repetitions of the same measurement were ±40 μm. The image of the scanned ion probe, with circles superimposed in the CAD software, is shown in Figure 3.15.

Separate power supplies are used to generate a potential on each cylindrical electrode. Each power supply is a Fluke 415B and provides highly regulated output. Error

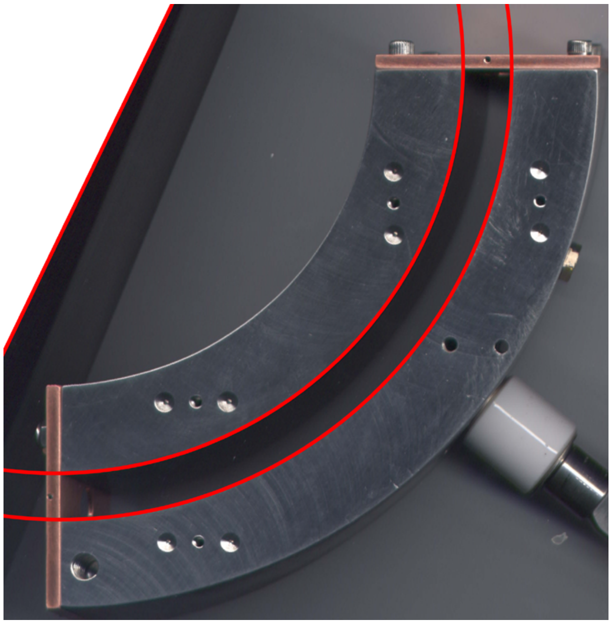

Figure 3.15: Image of the ion probe as scanned and imported into CAD software. The red circles are superimposed and used to determine the precise dimensions of the ion probe.

in the voltage from each power supply is ±40 mV over the range of voltages used in the experiments, as measured by a calibrated multimeter. The error in the KE/Z ratio at a specific voltage can then be calculated, e.g., for a potential difference of 100 V, the KE/Z ratio is 475 eV, and the error in the KE/Z ratio will be ±2.71 eV, in general about 0.6% of the nominal value.

The time-of-flight in the drift region depends upon the drift length and the KE/Z ratio. The error in the KE/Z ratio was previously reported, and the drift length is 118.4 ± 10 cm. The large static error in the drift length is due to error in the dimensions of physically large vacuum components, such as shown previously in Figure 3.3a and Figure 3.8. The time-of-flight in the acceleration region depends upon the KE/Z ratio, the CEM voltage, and the spacing of the acceleration gap. The CEM voltage is 2000.0 ± 0.1 V, and the gap spacing is 5.0 ± 0.1 mm. A specific example of time-of-flight data in the drift and acceleration regions, including error, for the same conditions used in the sample data set (Figure 3.11a, $KE/Z = 121 eV$) are summarized in Table 3.2 for the first three charge states of Sn ions.

The times at which peaks are found in the data, TOF_{expt}, are within the possible

Table 3.2: Various time-of-flight values for the same conditions as in the sample data set (Figure 3.11a); all times are in µs. The error in the time-of-flight calculation in the acceleration region is always less than 10 ns. TOF_{calc} represents the total calculated time-of-flight, and TOF_{expt} represents the times where peaks are found in the data.

Charge State	TOF_{drift}	δTOF_{drift}	TOF_{drift}	δTOF_{accel}	TOF_{calc}	TOF_{expt}
1	84.38	7.13	0.14	N/A	84.52	81.07
2	59.67	5.04	0.10	N/A	59.77	57.33
3	48.72	4.12	0.09	N/A	48.81	46.80

error in the calculated time-of-flight values for the first three charge states of Sn ions, TOF_{calc}. Furthermore, there are no other possible ions besides the first three charge states of Sn which the peaks seen in the data could represent. Therefore, the data itself can be used to calibrate the time-of-flight within its possible calculated error, and therefore to obtain a precise value for the drift length, which otherwise is known only to within $\pm 10\,\text{cm}$. An accurate value of the drift length is then $113.2\,\text{cm}$, which is within the error of the original estimate. After this calibration procedure, the precise value for drift length can be used in all subsequent data analysis. Finally, the quantity plotted on the horizontal axis of the ion energy distribution (Figure 3.14), ion energy, will have negligible error, as it depends upon variables with negligible error – ion mass, drift length, and time-of-flight.

The quantity plotted on the vertical axis of the ion energy distribution, dN_Z/dE, was given analytically in Eqn. (3.23), and depends upon preamplifier gain, CEM detection efficiency, CEM gain, measured voltage, scope resistance, and time-of-flight. Error in the measured voltage, scope resistance, and time-of-flight are all negligible, however, error in all other variables propagate to error in dN_Z/dE. The preamplifier gain was measured over the relevant frequencies, as shown in Figure 3.16, and is $G_A = 200 \pm 0.7$, which is exactly the preamplifier specification for the nominal gain [54].

Detection efficiency data for Sn was scaled from published detection efficiency data for Kr and Xe [58], as discussed previously. Figure 3.17a shows the scaled detection efficiency data as a function of $E/M^{0.6}$, in which the data for heavy ions scale to a single curve. In Figure 3.17b, detection efficiency data for Kr, Xe, and Sn are plotted as a function of ion energy in parameter space relevant to the present experiments. Table 3.3

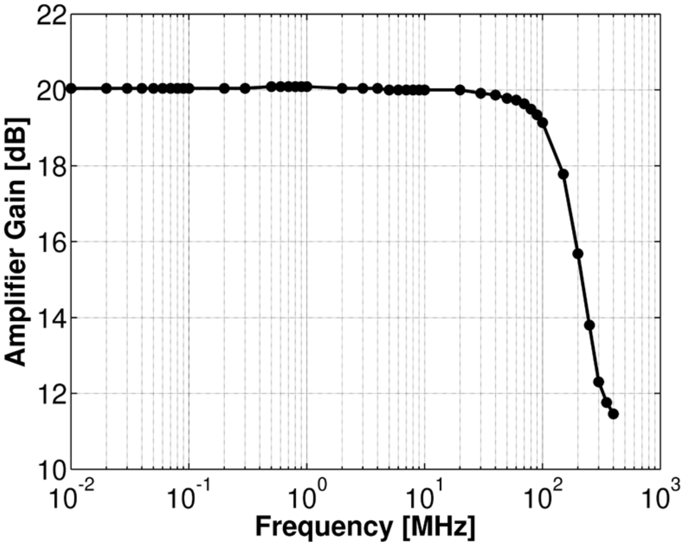

Figure 3.16: Frequency response of the low noise preamplifier [54]. A radio frequency signal generator, high frequency oscilloscope, and signal cables with calibrated frequency response were used in the measurement.

gives the coefficients used in calculating the detection efficiency data. The measurement error in the published detection efficiency data for Kr and Xe is $\pm 10\%$, and it is assumed to be the same for the scaled Sn data.

The final parameter affecting error in dN_Z/dE is error in the CEM gain. As discussed previously, CEM gain depends only upon applied voltage and does not vary with incident ion properties. Manufacturer's data for gain of the detector used in these experiments is available, however its quality is unreliable. In addition, CEM gain was not measured directly, nor was data available in the scientific literature. Therefore, an assumed value of 10^6 was used in the subsequent data analysis, taken from the manufacturer's data for an applied voltage of 2 kV, however, this value is not certain and its error cannot be reliably quantified. The error introduced in the calculation of dN_Z/dE by this assumption will be static, i.e., the magnitude is the same for all data points. The consequence of unknown static error is that dN_Z/dE must always be plotted in arbitrary units.

In summary, error in the CEM gain contributes an unknown amount of static error to the calculation of dN_Z/dE. Random error of 0.35% in the preamplifier gain, and random error of 10% in the detection efficiency collectively contributes 10.01% random

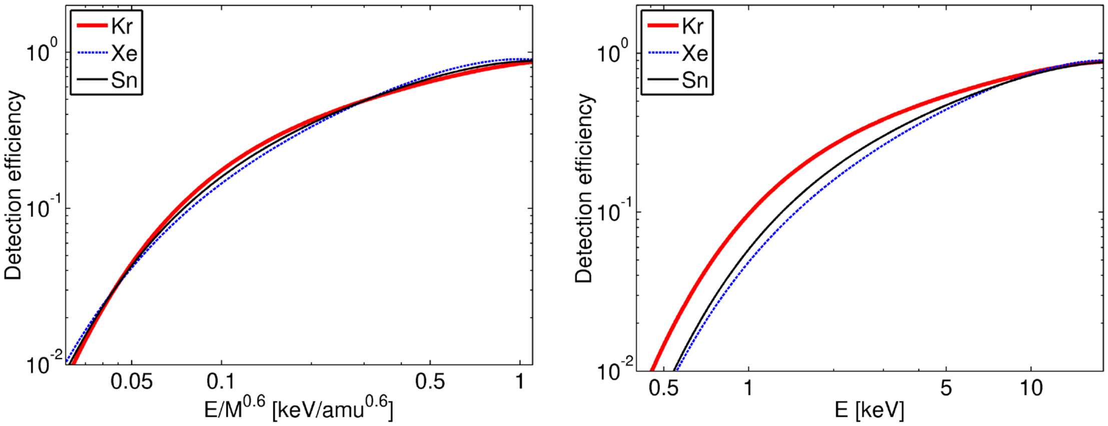

(a) Detection efficiency as a function of $E/M^{0.6}$ (b) Detection efficiency as a function of ion energy

Figure 3.17: Detection efficiency for Kr and Xe ions [58], in addition to detection efficiency data for Sn ions.

Table 3.3: Data used to calculate detection efficiency, γ, as a function of ion energy, E, in keV, and ion mass, M, in amu. Coefficients for Kr and Xe are reprinted from [58]. Data for Sn is scaled from the Kr and Xe data by a least squares fit in the same functional form, as given by the equation for all heavy ions.

$$\log(\gamma) = A + Bx + Cx^2 + Dx^3 + Fx^4$$

Ion	A	B	C	D	F	x
Kr	-1.012	1.962	-2.098	1.476	-0.450	$\log(E)$
Xe	-1.313	2.144	-1.763	1.264	-0.461	$\log(E)$
Sn	-1.233	2.217	-2.094	1.427	-0.456	$\log(E)$
All heavy ions	-0.058	0.126	-0.998	-0.840	-0.456	$\log(E/M^{0.6})$

error in the calculation of dN_Z/dE. This random error is assumed to be present along the vertical axis at each data point in subsequent plots of the ion energy distribution, however it is not plotted to maintain clarity of an otherwise complex figure.

Chapter 4

Mass Ablation from Sn Laser Produced Plasma

Mass ablation from Sn LPP is of significant interest in the development of a commercial EUV x-ray source, as it affects the emitted debris, and minimum mass required per target. In addition, the scaling of mass ablation rate with laser intensity provides insight into the laser absorption and energy transport physics, and can also aid in the benchmarking of radiation hydrodynamics codes. In this chapter, the ion probe described in Chapter 3, and the spectroscopic diagnostics described in Chapter 2, are used as complementary diagnostics to measure mass ablation rate as a function of laser intensity in parameter space relevant to the EUV x-ray source application.

4.1 Background and Literature Review

Extensive research over several decades has been devoted to understanding mass ablation in laser-produced plasma. Most studies are in parameter space relevant to the laser fusion application, in which typical laser wavelengths are 1.06 μm and its harmonics, typical laser intensities are 10^{12} to 10^{15} W/cm^2, and the target atomic number varies from 1 to 14 (H to Si) [60] [61] [62] [63]. However, only a few studies examine mass ablation as relevant to the EUV x-ray source application [25] [64], in which typical laser wavelengths are 1.064 and 10.6 μm, and typical intensities range from approximately 10^{10} to 10^{12} W/cm^2. Selected results of these previous studies are summarized in Table 4.1. It is seen that for laser intensities above $10^{13}\,\mathrm{W/cm^2}$, the mass ablation rate scales as $\dot{m} \propto I_a^{1/3}\lambda_L^{-4/3}$, whereas for laser intensities below $10^{13}\,\mathrm{W/cm^2}$ the mass ablation rate scales as $\dot{m} \propto I_a^{5/9}\lambda_L^{-4/9}$, where $\dot{m}$ is the mass ablation rate, λ_L is the laser wavelength, and I_a is the absorbed laser intensity. At the low laser intensities relevant to the EUV x-ray source application, the absorbed laser intensity is approximately equal to the laser intensity due to strong inverse bremsstrahlung absorption [65]. In addition, the scaling of mass ablation rate with target atomic number, Z, has been determined empirically only for $Z \leq 13$, and is the same at low and high laser intensities [62] [63]. Finally, in the only previous study of mass ablation using a Sn target [25], besides the present investigation [64], a very large spot size was used and only a single data point is acquired in deriving the published scaling law.

Theoretical models of steady-state planar ablation have been developed which are in agreement with the empirically determined scaling laws at both low and high laser intensities [11] [66] [67]. The models differ in the details of laser energy absorption, and energy transport from the critical surface to the ablation front (see Figure 1.1). At high laser intensities, above $10^{13}\,\mathrm{W/cm^2}$, the scaling law is consistent with an ablation model in which laser energy absorption is dominated by collisional absorption localized at the critical surface [11] [66], whereas at lower laser intensities the relevant ablation model assumes nonlocalized collisional absorption before the critical density [11] [67]. Furthermore, at high laser intensities, the consistent ablation model assumes energy transport from the critical surface to the ablation front is inhibited to a small fraction of the free-streaming limit, whereas at low laser intensities the relevant model assumes energy transport to the ablation front is by diffusive conduction of thermal electrons. Accordingly, the scaling law which is derived in this chapter for mass ablation from Sn LPP can be used to gain insight into physical mechanisms of laser energy absorption and energy transport within the hot plasma.

4.2 Experimental Parameters

In the present work, the ablation depth is measured using a 1.064 μm neodymium-doped yttrium aluminum garnet (Nd:YAG) laser at four different laser intensities, from

Table 4.1: Summary of selected scaling laws and numerical approximations for mass ablation rate found in the literature. In the equation for mass ablation rate, the absorbed laser intensity, I_a, has units of $10^{11}\,\mathrm{W/cm^2}$, the laser wavelength, λ_L, has units of μm, and the mass ablation rate, $\dot{m}$, has units of $\mathrm{g/cm^2/s}$. The target atomic number is Z.

Reference	Laser wavelength [μm]	Laser pulse duration [ns]	Spot size [μm]	Laser intensity [$\mathrm{W/cm^2}$]	Target material and type	Mass ablation rate (numerical approximation if available)
Fabbro, *et al.* [60]	1.06, 0.53, and 0.27	0.1 – 2.5	50 – 70	5×10^{13} to 10^{15}	CH, planar	$\dot{m}\approx\left(1.1\times10^{4}\right)I_a^{1/3}\lambda_L^{-4/3}$
Ng, *et al.* [61]	0.53, 0.35 and 0.27	2.0	80	10^{12} to 5×10^{13}	Al, planar	$\dot{m}\propto I_a^{5/9}\lambda_L^{-4/9}$
Dahmani [62]	1.06	0.7	44	10^{13} to 10^{15}	C and Si, planar	$\dot{m}\approx\left(5.5\times10^{3}\right)I_a^{1/3}\lambda_L^{-4/3}Z^{3/8}$
Dahmani and Kerdja [63]	1.06	3.0	96	10^{11} to 4.5×10^{12}	Al, planar	$\dot{m}\approx\left(3.5\times10^{3}\right)I_a^{5/9}\lambda_L^{-4/9}Z^{3/8}$
Fujioka, *et al.* [25]	1.064	10.0	500	10^{11} only	Sn spherical	$\dot{m}\approx\left(2.8\times10^{3}\right)I_a^{5/9}\lambda_L^{-4/3}$
Burdt, *et al.* [64]	1.064	6.5	56	3×10^{11} to 2×10^{12}	Sn, planar	$\dot{m}\approx\left(3.0\times10^{3}\right)I_a^{5/9}\lambda_L^{-4/9}Z^{3/8}$

3×10^{11} to $2 \times 10^{12}\,\mathrm{W/cm^2}$. The minimum of this range is relevant to the EUV x-ray source application, and the maximum of this range overlaps the low end of parameter space relevant to the laser fusion application [61] [63], so that previous analyses developed in the context of the laser fusion application can be applied here as well.

The Nd:YAG laser has a full-width-half-maximum pulse duration of 6.5 ± 0.5 [ns], and is focused onto a planar Sn target in a $1/e^2$ focal diameter of $56 \pm 3[\mu\mathrm{m}]$. The laser intensity is varied by adjusting the laser energy with a waveplate and polarizing beamsplitter in four settings, equal to 53.2 ± 11.0, 150.8 ± 8.7, 250.7 ± 10.8, and 352.7 ± 11.7 [mJ]. The energy of several laser pulses prior and subsequent to those used in collecting data are recorded with a pyroelectric energy monitor and used to calculate the mean value and error in the laser pulse energy. Additional error in the laser pulse energy is manifest from attempting to replicate the four energy settings when irradiating each target installed in the vacuum chamber, which is the most difficult at the lowest nominal laser energy where incremental rotations of the waveplate generate significant variations in the laser energy. Including all sources of error, the laser intensities investigated are 3.3 ± 1.1, 9.4 ± 1.8, 15.7 ± 2.7, and 22.0 ± 3.6 [$10^{11}\,\mathrm{W/cm^2}$].

The targets were made using electron beam evaporation to deposit thin layers of Sn with nanometer precision onto Si wafers several hundred micrometers thick. The Sn layer thickness was monitored during deposition by a quartz crystal thickness monitor, and verified post-deposition with a stylus profiler. A typical surface profile measured over the Si-Sn step is shown in Figure 4.1. Thirteen targets were prepared for the experiments with Sn layer thicknesses from 10 to 500 nanometers, in addition to an uncoated target and a target with a Sn layer several micrometers thick, hereafter referred to as the thick target. Each target was installed in a vacuum chamber evacuated below 10^{-5} torr, and irradiated three times at each laser intensity. Finally, the target was translated in the focal plane before each shot to provide a fresh surface.

The ablation depth is measured by irradiating layered targets with progressively thicker layers of Sn until the signatures of Si ions in the expanding plasma disappear, indicating the ablation depth has been reached or exceeded. The mass ablation rate is then a function of the measured ablation depth, the mass density of the target, and the laser pulse duration. Silicon ions in the expanding plasma are measured directly and

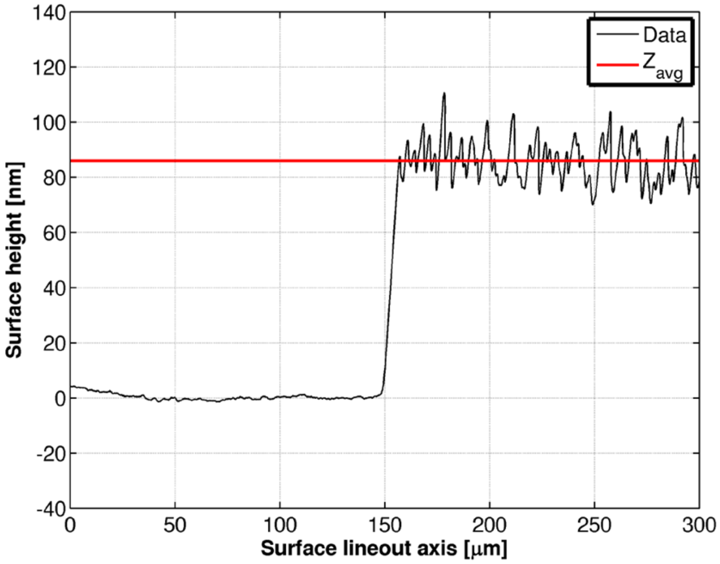

Figure 4.1: Surface profile of an 84 nm Si-Sn step on a layered planar target.

indirectly with three plasma diagnostics – the EUV calorimeter and EUV spectrometer described in Chapter 2, and the ion probe described in Chapter 3. The exact experimental arrangement is shown in Figure 4.2. Previous measurements of mass ablation rate use similar methods, e.g., Dahmani and Kerdja [63], and Dahmani [62] irradiate thin layers of Si and Al deposited onto a polystyrene (CH_2) substrate, and look for signatures of the substrate atoms with x-ray diagnostics. Additionally, other authors measured the mass ablation rate using burn-through measurements of thin films [60], or an array of Faraday cups surrounding the target [61]. However, the use of the ion probe described in Chapter 3 to measure mass ablation rate is a novel approach.

4.3 Experimental Results

The data from the EUV calorimeter are collected into plots of conversion efficiency (CE) as a function of target thickness at each of the four nominal laser intensities, as shown in Figure 4.3. The horizontal lines in the figure represent the limiting values for CE obtained with the thick Sn target at each laser intensity investigated. The limiting value of CE is the highest at $3.3 \times 10^{11}\,\mathrm{W/cm^2}$, and lowest at $2.2 \times 10^{12}\,\mathrm{W/cm^2}$. The exact values for CE at these laser intensities are consistent with previous work which

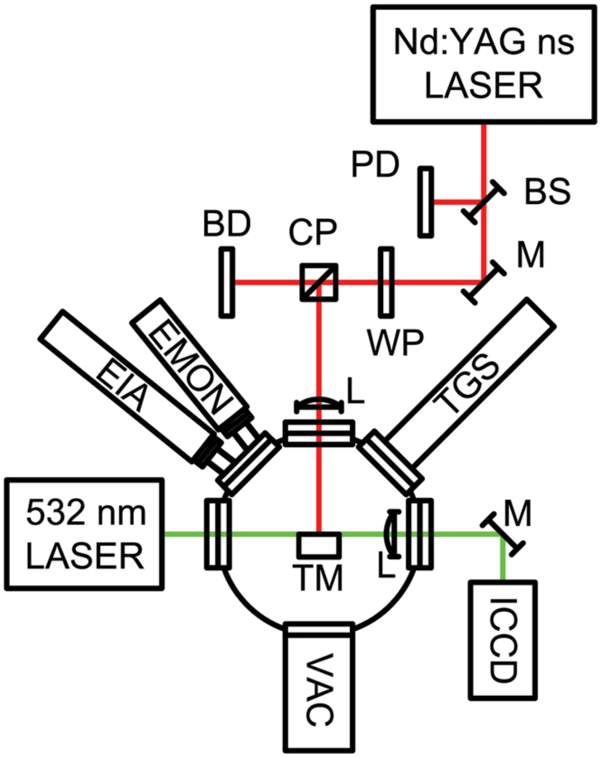

Figure 4.2: The experimental arrangement is shown. BS – beam sampler, PD – photodiode, WP – wave plate, CP – cube polarizer, BD – beam dump, L – lens, M – mirror, TM – target mount, VAC – vacuum pump, ICCD – intensified CCD camera used with 532 nm laser to align the target surface in the focal plane, TGS – transmission grating spectrometer installed at 45° with respect to target normal, EMON – calibrated EUV energy monitor installed at 39° with respect to target normal, EIA – electrostatic ion energy analyzer installed at 51° with respect to target normal.

has investigated the optimal laser parameters for high CE, and the variation is due to enhanced reabsorption of in-band emission as laser intensity increases [68] [69]. The CE at each laser intensity is negligible for the uncoated target, increases with target thickness before the ablation depth, and saturates with some rolloff near the ablation depth. The exact ablation depth is located in a consistent manner for all the curves and is equal to 220, 390, 515, and 620 [nm] at the laser intensities 3.3 ± 1.1, 9.4 ± 1.8, 15.7 ± 2.7, and 22.0 ± 3.6 [$10^{11}\,\mathrm{W/cm^2}$], respectively.

The data from the EUV spectrometer are collected into a single plot at each laser intensity, showing the evolution of the EUV spectrum as the target thickness is increased. The target thickness at which the spectrum is as intense as the spectrum measured using the thick Sn target indicates the ablation depth has been reached or exceeded. For example, Figure 4.4 shows the evolution of the EUV spectrum at the laser intensity 15.7 ± 2.7 [$10^{11}\,\mathrm{W/cm^2}$] as the target thickness is increased. It is seen that when a target with a thickness of 519 nm is irradiated, the EUV spectrum is as intense as the spectrum generated using the thick target, indicating the ablation depth has been reached at this target thickness. This is consistent with the measurement of ablation depth from the calibrated EUV energy monitor, as are the measurements of ablation depth using the EUV spectrometer at the three additional laser intensities.

The ion probe described in Chapter 3 can measure directly ions from both layers of a layered target whose thickness is less than the ablation depth. For example, Figure 4.5a shows a time-of-flight waveform in which 3 charge states of Sn and 2 charge states of Si meet the filter criterion of the probe. It was possible to measure ablation depth by looking for the target thickness at which ions from the base layer were not recorded with the ion energy analyzer, however this process was unrealistically time consuming because both the target thickness as well as the filter criterion of the probe had to be scanned at each laser intensity. A better method of measuring ablation depth with the ion probe was to keep the filter criterion of the probe constant and scan the target thickness until the current generated by the probe was equal to the current obtained using the thick target. For example, Figure 4.5b shows the data from the electrostatic ion energy analyzer using the thick target and a 390 nm target at a laser intensity of 9.4 ± 1.8 [$10^{11}\,\mathrm{W/cm^2}$], indicating the ablation depth has been reached. This result is

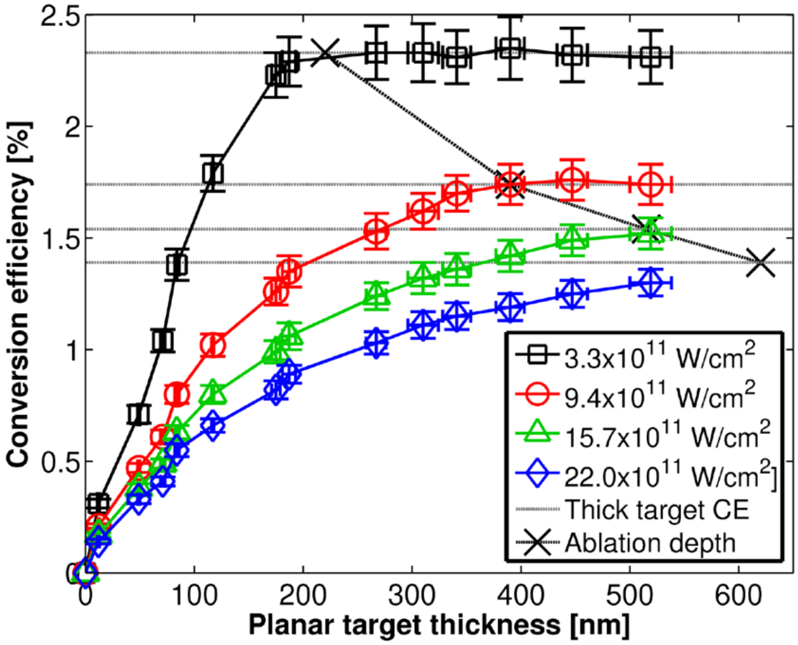

Figure 4.3: Conversion efficiency as a function of planar target thickness at each of the four nominal laser intensities.

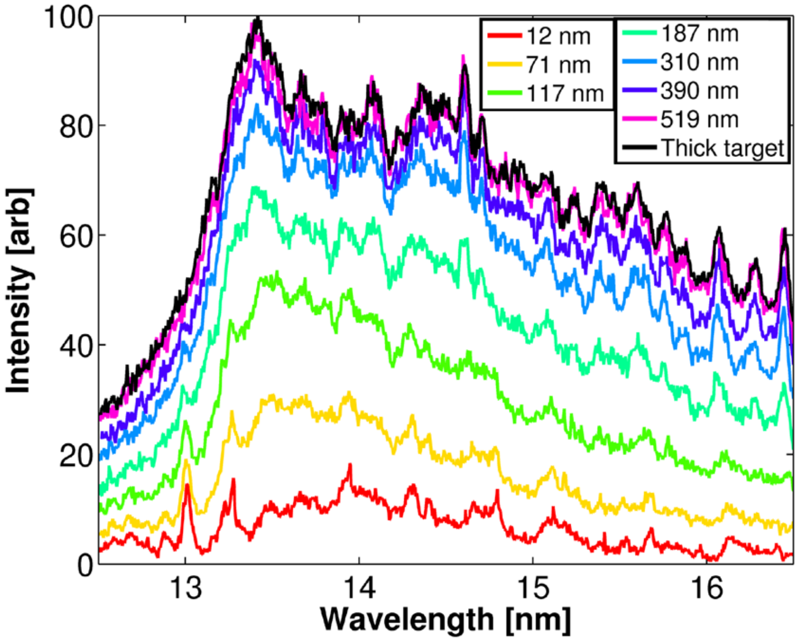

Figure 4.4: Evolution of the EUV spectrum at a laser intensity of 15.7 ± 2.7 $[10^{11}\,\mathrm{W/cm^2}]$ as the target thickness is increased.

consistent with the two spectroscopic diagnostics, as are the remaining measurements from the electrostatic ion energy analyzer.

4.4 Discussion and Conclusions

The spectroscopic and particle diagnostics used in the experiments generate consistent measurements of the ablation depth, $d_a = 220$, 390, 515, and 620 [nm] at laser intensities of 3.3 ± 1.1, 9.4 ± 1.8, 15.7 ± 2.7, and $22.0 \pm 3.6 [10^{11}\,\mathrm{W/cm^2}]$, respectively. This represents a scaling of ablation depth with laser intensity to the $(5/9)^{\mathrm{th}}$ power.

The mass ablation rate is determined from the ablation depth by the relation $\dot{m} = d_a \rho / \tau_L$, where ρ is the density of the target material ($7.31\,\mathrm{g/cm^3}$ for Sn), and τ_L is the laser pulse duration. Because the scaling of mass ablation rate with laser intensity found in the present work is consistent with the scaling found in previous studies in overlapping parameter space, it will be assumed that the scaling of mass ablation rate with laser wavelength and target atomic number are also equivalent to those found in the previous studies [61] [63]. Under this assumption, a numerical approximation for the mass ablation rate can be derived,

$$\left(\frac{\dot{m}}{\mathrm{g/cm^2/s}}\right) = (3 \times 10^3) \left(\frac{I_a}{10^{11}\,\mathrm{W/cm^2}}\right)^{5/9} \left(\frac{\lambda_L}{\mu\mathrm{m}}\right)^{-4/9} Z^{3/8}, \tag{4.1}$$

which is consistent with the numerical approximation found in Dahmani and Kerdja [63] in overlapping parameter space to within 15%. This is an indication that the scaling of mass ablation rate with target atomic number derived in Dahmani and Kerdja [63] using targets with $Z \leq 14$ is valid to the much higher $Z = 50$ used in the present experiment.

The numerical approximation found in the present study is inconsistent with that found in Fujioka, *et al.* [25], from which a numerical approximation for mass ablation rate in the same form as Equation (4.1) can be derived where the numerical factor would be 650. Therefore, under equivalent conditions, (laser intensity, laser wavelength, and target atomic number) the present work predicts the ablation depth would be approximately 4.5 times greater than predicted by the numerical approximation in Fujioka, *et al.* [25]. This distinction in mass ablation rate may result from the influence of the laser focal diameter, which is different by an order of magnitude in the two studies. This

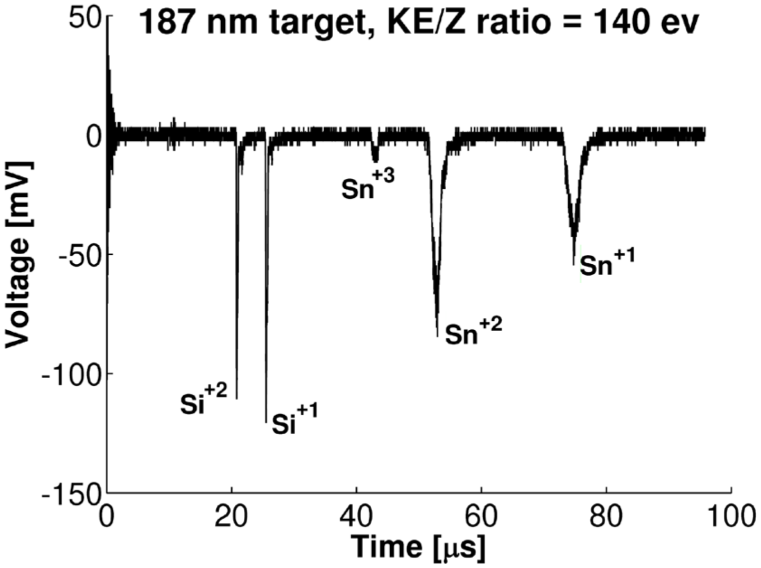

(a) Time-of-flight data using a 187 nm thick target. Each negative-going peak in the waveform represents the arrival of an ion species at the output of the probe meeting the filter criterion ($KE/Z = 140$ eV).

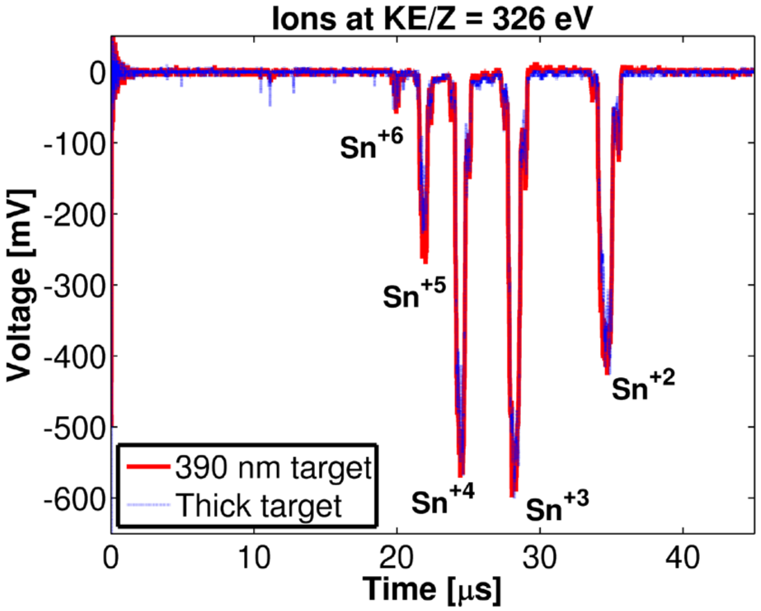

(b) Time-of-flight data for the thick target and a 390 nm target. The signal levels are identical in both waveforms, indicating the ablation depth was reached.

Figure 4.5: Time-of-flight data generated by the ion probe, using layered targets at a laser intensity of 9.4 ± 1.8 [10^{11} W/cm^2].

effect has not been examined in the vast studies of mass ablation rate for the laser fusion application, as these studies all typically use focal diameters in the range 50 to 100 µm [60] [61] [62] [63]. For the case of the present work, in which the laser focal diameter is small compared to that used by Fujioka, *et al.* [25] (56 µm as compared to 500 µm), the component of plasma expansion in the focal plane will be greater, which occurs when the plasma scale length $(n_e/|\nabla n_e|)$ is comparable to the laser focal diameter, where n_e is the plasma electron density. In this case, the plasma exhibits a complex two dimensional expansion [42], whereas in the case where the laser focal diameter is large compared to the plasma scale length the expansion is one dimensional and directed along the target normal. The case in which the plasma expands one dimensionally will restrict the ablation during the laser pulse and thus the mass ablation rate should be lower, as observed in the experiments.

The scaling of mass ablation rate with laser intensity derived here for laser produced Sn plasma, is consistent with a published model of steady-state planar ablation for low laser intensities [11] [67]. This model assumes nonlocalized laser absorption up to the critical density, and energy transport to the ablation front by diffusive conduction of thermal electrons. Other authors have discussed experiments where the EUV-emitting region of a Sn plasma is imaged directly, and shown to extend several hundred micrometers towards the laser axis [70], which confirms the nonlocalized laser absorption model inferred here. The assumption of diffusive conduction of thermal electrons, as opposed to a flux-limited model, is valid when $\lambda_e/L_T \leq 10^{-2}$ is satisfied, where λ_e is the electron mean free path, and L_T is the temperature gradient, $L_T = T/(dT/dx)$ [11] [71]. Over the range of conditions present in Sn plasma for the EUV x-ray source application, this condition may or may not be satisfied, and most hydrodynamics codes therefore calculate thermal conductivity in both the classical model and the flux-limited model, and use the minimum of the two [8] [72]. In recent work using a Nd:YAG laser to generate a Sn plasma, in parameter space similar to the present experiments, the electron mean free path is estimated as $\lambda_e \approx 0.3\,\mu\text{m}$ and the temperature gradient is estimated as $L_T \approx 50\,\mu\text{m}$ [73], which confirms that the energy transport model [11] [67] inferred by the mass ablation measurements here should be correct.

Chapter 4, in part, has been published in Journal of Applied Physics **106** 033310

(2009). The dissertation author was the primary investigator and author of this paper. Co-authors of this article include Sam Yuspeh, Kevin Sequoia, Yezheng Tao, Mark Tillack, and Farrokh Najmabadi, all of whom are associated with the Center for Energy Research at the University of California, San Diego.

Chapter 5

Laser Wavelength Effects on Ion Properties from Laser Produced Sn Plasma

As discussed in Section 1.1, the choice of laser wavelength affects many of the subsequent processes occurring throughout the laser plasma interaction. The initial density of hot plasma is approximately equal to the critical density, set by the laser wavelength, which in turn affects the laser absorption, ionization, and energy transport mechanisms on the nanosecond scale, and the recombination processes up to the microsecond scale. Different applications demand various features in the debris or radiation emitted from the laser plasma interaction, and therefore different laser wavelengths are commonly used. In this chapter, two experiments are discussed which investigate ion properties from Sn plasma produced by both 1.064 μm and 10.6 μm laser radiation. Laser wavelength effects on the charge-state resolved ion energy distributions, as measured in the far expansion zone, are discussed first [74]. Following, the effects of laser wavelength on the spatial evolution of the charge state distribution are discussed [75].

5.1 Laser Wavelength Effects on the Charge-State Resolved Ion Energy Distributions

The EUV x-ray source application places stringent requirements on the lifetime of the EUV collection mirror, such as shown in Figure 1.2 [12]. To meet these requirements, methods to control and manipulate the emitted plasma debris, consisting of ions, electrons, and neutral particles, must be implemented. Electrostatic and magnetostatic repeller fields, background gases, and prepulsing to lengthen the initial density gradient, have all been proven to be effective methods [27] [28] [29]. To achieve further improvements in debris mitigation, the exact distribution of ion species, charge states, and energies must be diagnosed, and the dependence on the incident laser parameters, specifically the laser wavelength, must be understood physically.

5.1.1 Experimental Conditions and Results

The experimental arrangement is shown in Figure 5.1. A planar Sn target is irradiated in one experiment by an Nd:YAG laser and in another by a CO_2 laser. The experiments are conducted in vacuum below 3×10^{-6} torr so charge-exchange with the ambient will be negligible [76]. The target is translated in the focal plane before each shot to provide a fresh surface. The spot size at each laser wavelength is measured by the experimental procedure described in Section 2.2.3. The laser and focusing parameters at each wavelength are summarized in Table 5.1. The conversion efficiency is measured at each laser wavelength with the calibrated EUV calorimeter described in Section 2.3, and is 2% using the Nd:YAG laser and 3% using the CO_2 laser.

The charge state resolved ion energy distributions from Nd:YAG and CO_2 LPP are shown in Figure 5.2a and Figure 5.2b, respectively. These data are time-integrated and represent a solid angle of observation of 7.9×10^{-9} sr (a $100\,\mu$m input pinhole positioned 100 cm from a laser plasma source). Approximately 30 shots under repetitive laser conditions were used in the data analysis at both laser wavelengths.

The ion energy distributions for each charge state at both laser wavelengths are

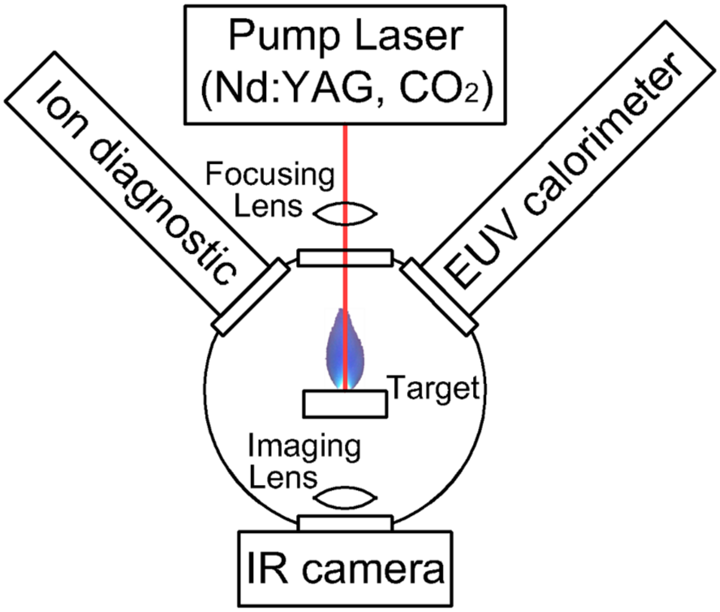

Figure 5.1: Experimental arrangement. The EUV calorimeter and ion diagnostic are positioned at 45 and 51 deg with respect to the laser axis, respectively. In the optical path at each laser wavelength, not shown here, were installed a photodiode and laser energy monitor for real-time monitoring of the laser pulse duration and energy.

Table 5.1: Laser parameters used in the experiments. The pulse duration, τ_L, is calculated using full-width-half-maximum values, and the spot size, d_S, is calculated where the intensity in the focal plane is equal to (1/e^2) of its maximum value. The focusing lens in each experiment is plano-convex with focal length f and f/# given below. The irradiance, I, is calculated from the laser parameters as $I = (E_L/\tau_L)/(\pi d_S^2/4)$, where E_L is the laser pulse energy.

Wavelength [µm]	Pulse Duration [ns]	Pulse Energy [mJ]	Spot Size [µm]	f [cm]	f/#	Irradiance [W/cm^2]
1.064	7	120	80	30	f/15	3.4×10^{11}
10.6	85	120	100	6	f/6	1.8×10^{10}

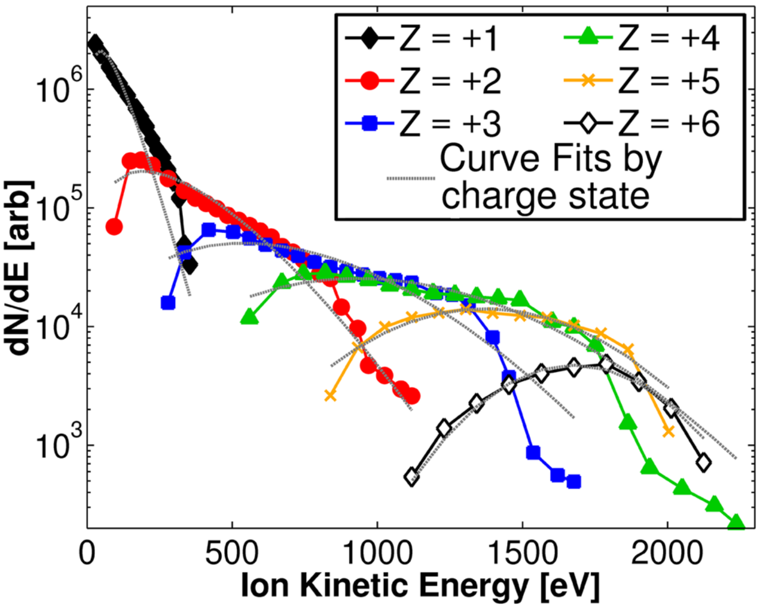

(a) Charge-state resolved ion energy distribution from Sn plasma generated by a 1.064 µm laser

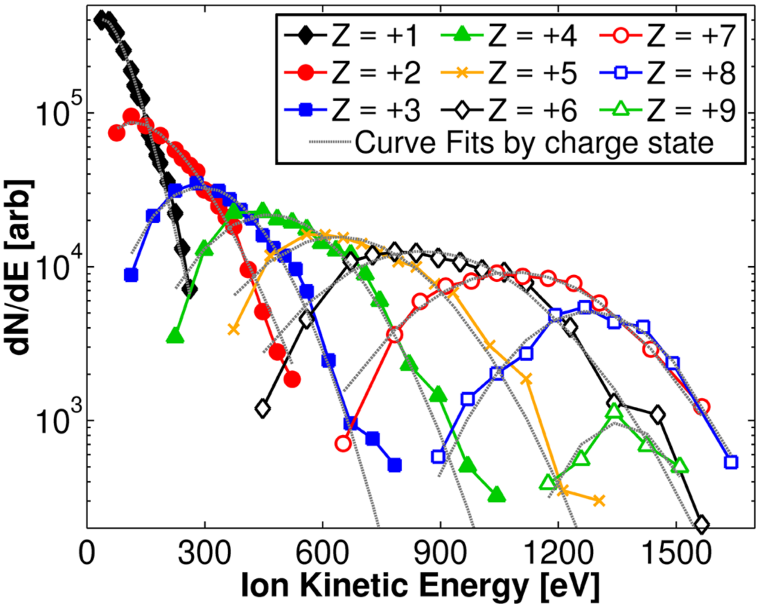

(b) Charge-state resolved ion energy distribution from Sn plasma generated by a 10.6 µm laser

Figure 5.2: Charge-state resolved ion energy distributions from Sn plasma in the parameter space summarized in Table 5.1

fit in a least squares sense by functions of the form

$$f(E_{ion}) = A\,E_{ion}\exp\left[-\left(E_{ion}-\mu\right)^2/(2\sigma)^2\right], \tag{5.1}$$

where f approximates dN/dE, E_{ion} is the ion kinetic energy, and A, μ, and σ are unique fitting parameters for each curve. These curve fits are included as broken gray lines in Figure 5.2, and the closeness of each fit is quantified in Table 5.2. Similar fitting functions along with their physical basis are described in previous experimental and theoretical studies [77] [78] [79]. Using the curve fits to the data at each laser wavelength, the average charge state and average ion energy, as well as the ion concentration and peak ion energy for each charge state can all be calculated; results are found in Table 5.2.

5.1.2 Discussion of Experimental Results

Several general features can be summarized from the experimental results. First, the increase in laser wavelength increases the maximum charge state measured far away from the laser produced plasma (LPP) source. At the moderate laser intensities of the present experiments, a single thermal population of electrons is present and the initial electron density in the corona will approximately equal the critical density, n_{cr}. For the Nd:YAG LPP, $n_{cr} \approx 10^{21}\,\mathrm{cm}^{-3}$, and for the CO_2 LPP, $n_{cr} \approx 10^{19}\,\mathrm{cm}^{-3}$. The lower initial electron density of the CO_2 LPP has a significant effect on the recombination processes during and after the laser pulse. The two mechanisms of recombination in the laser plasmas discussed here include three-body recombination and radiative recombination [81] [82]. In both processes, a free electron recombines with an ion, and a third body (a photon in radiative recombination, a free electron in three-body recombination) is required to conserve energy. A criterion can be derived using the rates for both processes determining which of the two mechanisms is dominant [83]. If the plasma electron density, n_e, electron temperature, T_e, and average charge state, $\bar{Z}$, satisfy the relation

$$\left(n_e/\mathrm{cm}^{-3}\right) \gg \frac{\left(3\times10^{13}\right)\left(T_e/\mathrm{eV}\right)^{3.75}}{\bar{Z}}, \tag{5.2}$$

then three-body recombination is the dominant mechanism. During the laser pulse, this inequality is satisfied for the Nd:YAG LPP, but not for the CO_2 LPP. After the laser pulse, when T_e begins to decay, three-body recombination will quickly become the dominant

Table 5.2: Ion properties calculated from the data and curve fits in Figure 5.2. The closeness of the approximation of f to dN/dE can be quantified by the coefficient of determination, R^2, defined, e.g., in Rao [80]. The peak ion energies are the maxima of the curve fits. These ion properties can be used to estimate the initial electron temperature and elucidate the mechanism of ion acceleration.

Wavelength [μm]	Ions	R^2 [%]	Ion concentration [%]	$\bar{Z}$	Peak ion energy [eV]	Average ion energy [eV]
1.064	Sn^{+1}	94.6	59.3	1.8	45	792
	Sn^{+2}	88.3	20.8		191	
	Sn^{+3}	87.9	10.0		536	
	Sn^{+4}	95.0	6.4		931	
	Sn^{+5}	98.3	2.9		1 369	
	Sn^{+6}	99.0	0.7		1 677	
10.6	Sn^{+1}	99.8	40.1	2.7	41	680
	Sn^{+2}	99.1	20.2		116	
	Sn^{+3}	98.4	10.0		289	
	Sn^{+4}	96.3	8.3		463	
	Sn^{+5}	97.3	7.3		637	
	Sn^{+6}	97.1	6.9		854	
	Sn^{+7}	99.1	4.9		1 084	
	Sn^{+8}	98.3	2.1		1 280	
	Sn^{+9}	95.8	0.3		1 356	

process for both laser plasmas. Since the rate of three-body recombination will depend on the density of free electrons, the laser plasma with the lower initial electron density will experience less recombination. Thus, for the CO_2 LPP higher charge state ions should be found far away from the laser plasma source, as observed in the experiments.

The initial electron temperature, T_e, can be estimated from the ion properties through an expression derived in a hydrodynamic model of laser plasma interactions in a similar parameter regime, as discussed in Puell [84]. The relation is given by

$$E_a = 5\,(\bar{Z}+1)\,T_e, \tag{5.3}$$

where E_a is the average ion energy, and has been applied by several authors in interpretation of data from ion probes [49] [83]. From Equation (5.3) and the values in Table 5.2, T_e is estimated as 37 and 57 eV for the CO_2 and Nd:YAG LPP, respectively. However, the theory in Puell assumes that E_a is evaluated far from the laser plasma source along the target normal, whereas in the experiments E_a is measured far from the laser plasma source but at an angle of 51° with respect to the target normal. It is well know from previous studies that all ion energies are peaked along the target normal, so that ion energies measured at approximately 45° from the target normal are a factor of a few less than those measured along the target normal [37] [85]. In addition, the theory in Puell assumes $\bar{Z}$ is evaluated at a distance from the target surface equal to the laser focal radius, whereas in the experiments $\bar{Z}$ is measured far from the laser plasma source. The effect of recombination during plasma expansion into vacuum is known to reduce $\bar{Z}$ by a factor of a few; this topic is treated in several previous studies as well as in the numerical simulations discussed in the subsequent chapter [86] [87] [88]. Accordingly, the order of magnitude estimates of T_e and the qualitative observation that T_e is higher for the Nd:YAG LPP obtained by using Equation (5.3) with the experimental values for $\bar{Z}$ and E_a are still correct.

The mechanism of ion acceleration can be inferred from a plot of the peak ion energies given in Table 5.2 as a function of charge state, as shown in Figure 5.3. Similar features observed in both curves indicate the ion acceleration mechanism is independent of laser wavelength. Specifically, the peak ion energies increase approximately linearly as a function of charge state and all ion energies greatly exceed the initial thermal electron temperature. These effects have been noted before from plasma produced by ruby

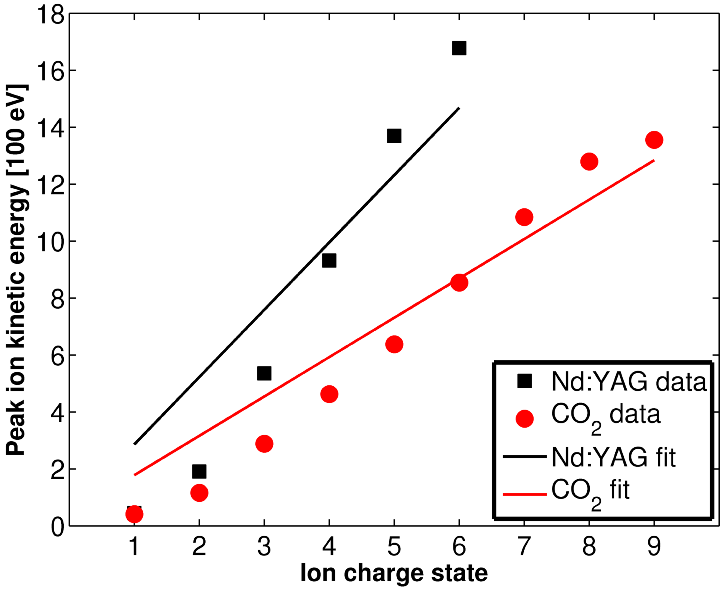

Figure 5.3: Peak ion energy as a function of charge state from Sn plasma produced by Nd:YAG and CO_2 lasers. Equation (5.5) is fit to the data at both laser wavelengths. The coefficients of determination, R^2, of the Nd:YAG and CO_2 curve fits are 87% and 93%, respectively.

and Nd:YAG lasers in similar parameter space [89] [90] [91], however, experimental data showing these features at the 10.6 μm CO_2 laser wavelength are not found in the literature.

An acceleration mechanism leading to the observed features in the ion spectra is the electrostatic model [90] [92]. Electrons heated by the laser through inverse bremsstrahlung transfer energy to ions through collisions on the scale of the electron ion thermalization time, τ_{ei}, given by

$$(\tau_{ei}/s) \approx \left(3.5 \times 10^8\right) \frac{(A/amu)\,(T_e/eV)^{3/2}}{\bar{Z}\,(n_e/\mathrm{cm}^{-3})\ln\Lambda}, \tag{5.4}$$

where A is the atomic mass (118.71 amu for Sn), and $\ln\Lambda$ is the Coulomb logarithm ($\approx$5 for laser plasma) [93]. Because τ_{ei} will be much shorter than the laser pulse duration, electrons and ions obtain equal thermal temperatures during the laser pulse, but due to the mass difference the electrons obtain higher velocities. The electrons then escape the plasma volume thereby creating an electrostatic field which accelerates ions proportional to their charge. As this process repeats several times during the laser pulse, the resultant ion kinetic energies are typically many times the initial thermal electron temperature, as observed in the experiments. A scaling law with physical significance from the electrostatic model is given by

$$E_{ion} = nZT + T, \tag{5.5}$$

where E_{ion} is in eV, Z is the charge state, and T is the initial electron and ion thermal temperatures (assumed equal) in eV [92]. The first term (nZT) represents the repetition of the acceleration process n times during the laser pulse, and the second term (T) represents the conversion of thermal electron temperature into ion kinetic energy through expansion. A least squares fit of Equation (5.5) to the experimental data at both laser wavelengths is included as a solid line in Figure 5.3; the R^2 value quantifying the closeness of each fit is given in the caption. The fitting parameters n and T for the Nd:YAG curve fit are 4.7 and 50 eV, whereas the fitting parameters for the CO_2 curve fit are 3.5 and 40 eV. The effects of recombination during plasma expansion into vacuum, not taken into account in the electrostatic model, prevents better quantitative agreement, suggesting that the electrostatic model cannot be used to completely describe ion acceleration in the laser plasmas studied within.

The laser intensities in the two experiments were different ($1.8 \times 10^{10}\,\mathrm{W/cm^2}$ for the CO_2 LPP and $3.4 \times 10^{11}\,\mathrm{W/cm^2}$ for the Nd:YAG LPP), and were chosen such that CE was optimal in each case (3% for the CO2 LPP and 2% for the Nd:YAG LPP). A significant amount of theoretical work within the EUV x-ray source community has converged on the plasma parameters which optimize CE (see White, *et al.* [17] and references 1-12 therein); these being electron temperature of 30 – 40 eV and electron density of $10^{19}\,\mathrm{cm^{-3}}$. Thus, both laser plasmas studied here contain some region with this combination of plasma parameters. The region with the optimal plasma parameters for the CO_2 LPP is the hottest region of the plasma, as the critical density at this wavelength ($\approx 10^{19}\,\mathrm{cm^{-3}}$) is equal to the optimal electron density. In the case of the Nd:YAG LPP, the critical density ($\approx 10^{21}\,\mathrm{cm^{-3}}$) must decay by two orders of magnitude to reach the optimal electron density. Accordingly, the temperature of the Nd:YAG LPP must also decay from its initial value at the critical density to reach the optimal electron temperature, as temperature and density in an LPP decay simultaneously in space [83]. By this argument, the initial electron temperature of the Nd:YAG LPP should be higher than the optimal temperature. The estimate of 50 – 60 eV inferred from the ion probe data is in agreement.

5.2 Laser wavelength effects on the spatial evolution of the charge state distribution

High charge state ions can be measured meters away in vacuum from a laser produced plasma source at low ($< 10^{12}\,\mathrm{W/cm^2}$) [74], high ($\sim 10^{15}\,\mathrm{W/cm^2}$) [94], and relativistic ($\sim 10^{19}\,\mathrm{W/cm^2}$) [95] intensities. Close to the target surface of a Sn plasma for EUVL, where the plasma temperature is greater than 20 eV and plasma density is greater than $10^{19}\,\mathrm{cm^{-3}}$, atomic models predict the average ion charge state will be greater than 10 [96]. However, the previous measurements discussed in Section 5.1.1 reveal the average ion charge state has decayed to a value much less than 10 in the far expansion zone, dependent on the initial plasma conditions. Complete recombination is prevented by fast plasma expansion to a sufficiently rarefied state where recombination processes become negligible. It is important to understand the effects of recombination during expansion into vacuum, due to the applications demanding specific features in the charge state distribution far from the laser plasma source. For example, in a laser ion source, the high charge state ions are used for extraction and injection into accelerators [94]. Alternatively, in the extreme ultraviolet (EUV) x-ray source application the high charge state ions damage downstream optical components and must be mitigated [97]. Accordingly, the spatial evolution of the charge state distribution has been investigated experimentally at both $1.064\,\mu\mathrm{m}$ and $10.6\,\mu\mathrm{m}$ laser wavelengths.

5.2.1 Experimental Conditions and Results

The distance from the target surface over which the charge state distribution evolves before freezing for subsequent expansion, hereafter referred to as the critical distance, is investigated experimentally. The critical distance is measured by scanning a Faraday cup along the path of plasma expansion; a diagram of the experimental arrangement is shown in Figure 5.4a, and a photograph of the experimental arrangement is shown in Figure 5.4b.

The Faraday cup is electrically biased to measure the time-resolved ion current from the LPP, and the ion current is time-integrated to give the total ionic charge collected by the Faraday cup at the distance L from the target, $Q_i(L)$. This quantity will be a fraction of the total ionic charge emitted into 2π sr, Q_{i0}, as measured at the distance L, related by

$$Q_i = Q_{i0}\left(\Omega_{\text{eff}}/2\pi\right), \tag{5.6}$$

where Ω_{eff} is the effective solid angle of the faraday cup,

$$\Omega_{\text{eff}} = \int_0^{2\pi}\int_0^{\Theta} \cos^p(\theta+\alpha)\sin\theta d\theta d\phi, \tag{5.7}$$

and the integration is over the circular aperture of the Faraday cup, i.e., $\Theta = \tan^{-1}(D/L)$. The normalized angular distribution of emitted ions (symmetric about the laser axis) is represented by $\cos^p(\theta+\alpha)$, which is an empirical fit to experimental data [19]. When the angular distribution is isotropic ($p = 0$), the usual expression for solid angle is recovered.

If the calculated quantity Q_{i0} is constant, within appropriate error bars, as the Faraday cup is scanned away from the target over an interval ΔL, this implies the charge state distribution is frozen into the expansion within ΔL. However, if Q_{i0} is decreasing as the Faraday cup is scanned away from the target over an interval ΔL, this implies the ion populations are recombining to lower charge states within ΔL.

Similar experiments and analyses have been used to demonstrate a decaying charge state distribution up to 15 cm away from a Cu target irradiated by a low intensity XeCl laser [98], and a frozen-in charge state distribution after 82 cm of expansion from various high-Z targets irradiated by a high-intensity iodine laser [94], both to support the laser ion source application. The topic of charge state freezing in LPP has been treated theoretically [8] as well, where a scaling law for the critical distance, L_{CR}, was derived,

$$L_{CR} \propto \frac{T_e^{13/12} v_i^{14/6} \tau_L^{13/6}}{n_{cr}^{8/18} d_S^{8/6}}. \tag{5.8}$$

Typical parameters relevant to the EUV x-ray source application are electron temperature, $T_e \approx$ 30-40 eV, ion velocity, $v_i \approx 2\times10^6\,\text{cm/s}$, and laser spot size, $d_S \approx 100\,\mu\text{m}$, all irrespective of laser wavelength. The critical electron density, n_{cr}, is laser wavelength dependent and differs by two orders of magnitude at $1.064\,\mu\text{m}$ and $10.6\,\mu\text{m}$ wavelengths,

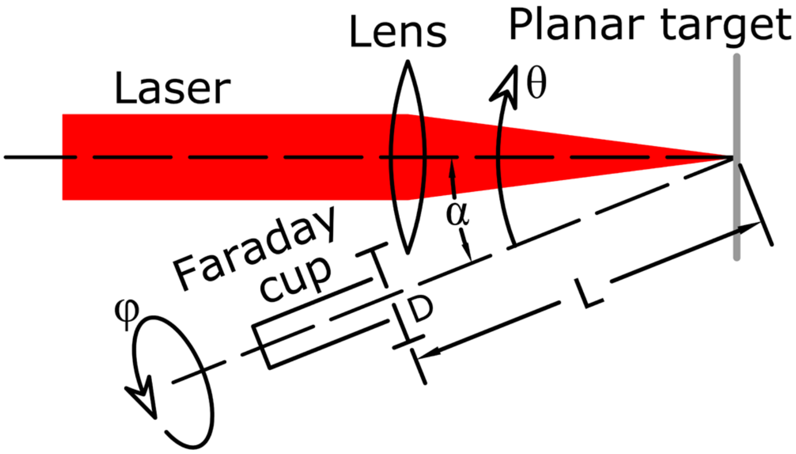

(a) Diagram of the experimental arrangement for measurement of the critical distance.

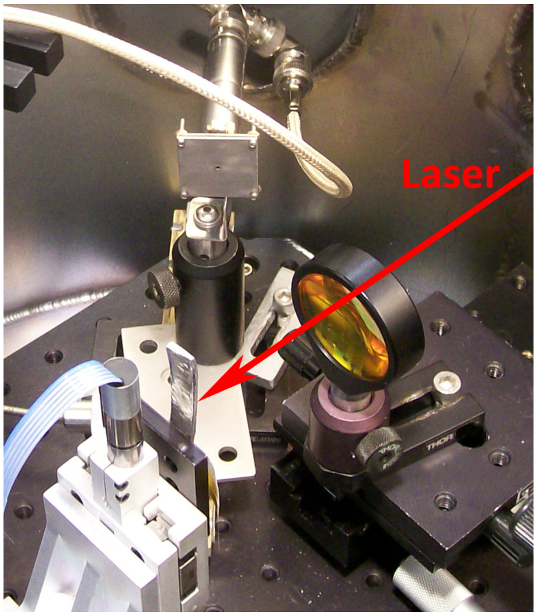

(b) Photograph of the experimental arrangement for measurement of the critical distance.

Figure 5.4: A focused laser irradiates a planar target at normal incidence. A Faraday cup with aperture diameter D is installed at an angle α to the target normal and can be translated distances L along the path of plasma expansion. A spherical coordinate system with zenith angle θ and azimuthal angle ϕ with respect to the Faraday cup translation axis is superimposed.

Table 5.3: Laser parameters used in the experiments. As in Table 5.1, the pulse duration is calculated using full-width-half-maximum values, and the spot size is calculated where the intensity in the focal plane is equal to (1/e^2) of its maximum value.

Wavelength [μm]	Pulse Duration [ns]	Pulse Energy [mJ]	Spot Size [μm]	f [cm]	Irradiance [W/cm^2]
1.064	7	165	60	30	8.3×10^{11}
10.6	35	50	85	6.4	2.5×10^{10}

as given in Section 5.1.2. The pulse duration, τ_L, is generally longer for CO_2 lasers as compared to Nd:YAG lasers. It was estimated by Roudskoy [8] that at moderate laser intensities ($< 10^{15}/\lambda^2$ W/cm^2, where λ is the laser wavelength in μm), L_{CR} would be on the order of centimeters for $\lambda \approx 1\,\mu$m, but could reach up to meters for $\lambda \approx 10\,\mu$m.

The long range over which L_{CR} can vary leads to a few important implications for the EUV x-ray source application. As discussed in Section 1.2.1, the EUV collection mirror is positioned on the order a few tens of cm from the laser plasma source, however measurements of the charge state distribution are necessarily taken 100 cm from the laser plasma source due to diagnostic limitations, as discussed in Section 3.2. If the measurements are to represent the actual charge state distribution at the surface of the EUV collection mirror, the critical distance must be less than a few tens of cm. Furthermore, a long critical distance will motivate the application of an electromagnetic-based ion mitigation scheme.

The critical distance was measured at both laser wavelengths, in parameter space summarized in Table 5.3. Sample Faraday cup waveforms, representing time-resolved ion current, are shown in Figure 5.5a for the experiments at 1.064 μm, and in Figure 5.5b for the experiments at 10.6 μm. A photodiode and laser energy monitor were installed in the optical path in both experiments to ensure repeatable irradiation conditions for each laser pulse. The targets were high-purity (>3N) Sn slabs which were translated in the focal plane before each shot to provide a fresh surface, and all experiments were conducted in vacuum below 3×10^{-6} torr so charge exchange with the ambient was negligible [76].

For the calculation of effective solid angle [Eqn. (5.7)], the functional form of

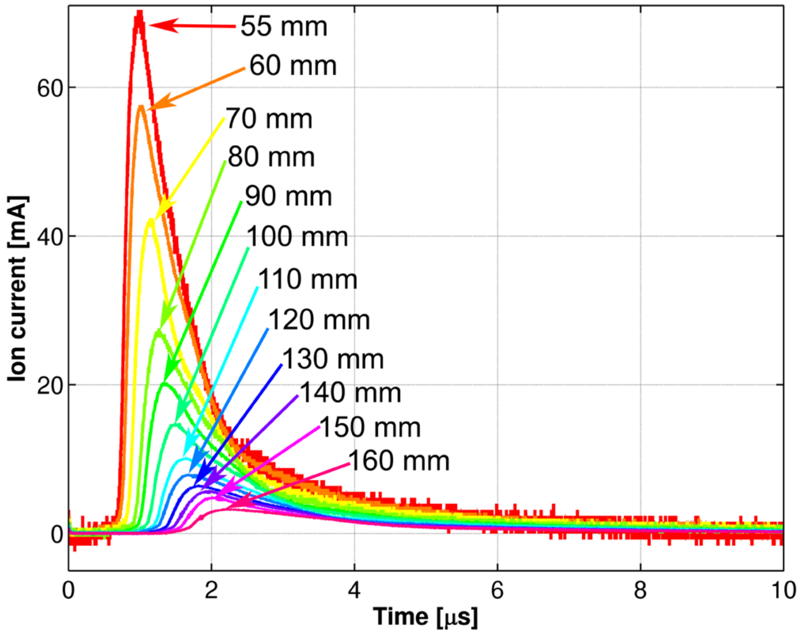

(a) Faraday cup waveforms for a laser wavelength of 1.064 µm

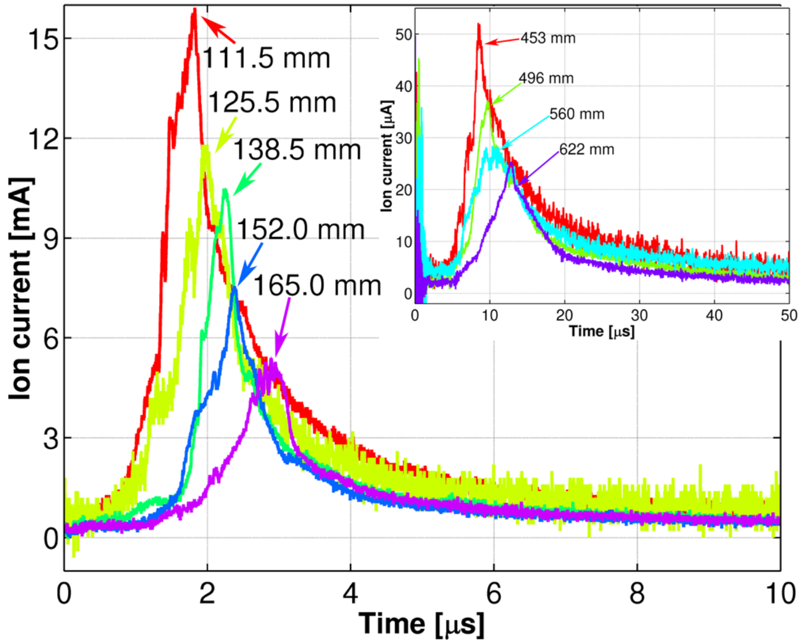

(b) Faraday cup waveforms for a laser wavelength of 10.6 µm

Figure 5.5: Faraday cup waveforms, representing time-resolved ion current, at both laser wavelengths. The distance from the laser plasma source to the Faraday cup aperture, L, is identified for each waveform. Each waveform was integrated to obtain the local charge collected at the distance L, $Q_i(L)$, as appearing in Eqn. (5.6).

the angular distribution of emitted ions must be known, specifically the exponent p in the fitting function $\cos^p(\theta+\alpha)$. Tanaka, *et al.* have measured p for Nd:YAG LPP at intensities on the order of $10^{11}\,\mathrm{W/cm^2}$ to be approximately 2, in agreement with data from other authors in similar parameter space [19] [37].

The angular distribution of emitted ions from the CO_2 LPP was measured directly, as prior data in the parameter space of Table 5.3 was not available. Four identical Faraday cups were installed in a vacuum chamber, each 105 mm from the target, at angles of 27.0°, 37.3°, 52.9°, and 68.4° with respect to the target normal, as shown in Figure 5.6a. The target and CO_2 laser parameters were identical for all experiments. Typical signals recorded simultaneously from all four Faraday cups are in Figure 5.6b, offset from each other but with the same vertical scale. A polar plot of mean ion energies can be generated from the multiple Faraday cup waveforms, and is shown in Figure 5.6c; 0° is the target normal. A function of the form $\lambda_1\cos^p\theta+\lambda_2$ was fit in a least squares sense to the data, and $p = 1.75$ was obtained. The mean ion energies in Figure 5.6c are calculated as

$$\langle E\rangle = \frac{M}{2}\left(\frac{d}{\langle t\rangle}\right)^2, \tag{5.9}$$

where M is the ion mass (118.71 amu for Sn), d is distance from each Faraday cup to the target (105 mm), and

$$\langle t\rangle = \frac{\int_0^\infty t\times v(t)dt}{\int_0^\infty v(t)dt}, \tag{5.10}$$

where $v(t)$ is the measured voltage from the Faraday cup as a function of time. The calculated mean ion energies in Figure 5.6c were averaged from at least 20 shots.

The critical distance at each laser wavelength can be inferred from a plot of Q_{i0}, as described in Equations (5.6) and (5.7), as a function of the distance from the laser plasma source to the Faraday cup aperture. This plot, for the experiments at 1.064 μm and 10.6 μm, is shown in Figure 5.7.

5.2.2 Discussion of Experimental Results

In Figure 5.7, for the data obtained using the Nd:YAG laser, the Faraday cup was scanned from 55 mm to 160 mm on a translation stage inside the vacuum chamber, and over this interval Q_{i0} was constant within the error bars. This indicates the critical

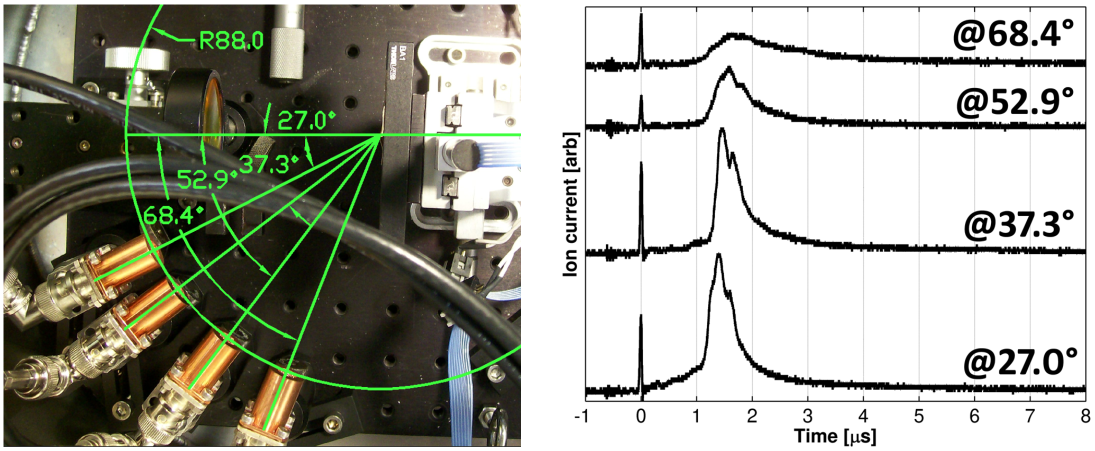

(a) Photograph of the angular distribution experiment. Dimensions in mm and deg are superimposed using CAD software.

(b) Sample Faraday cup waveforms from CO_2 LPP in parameter space of Table 5.3.

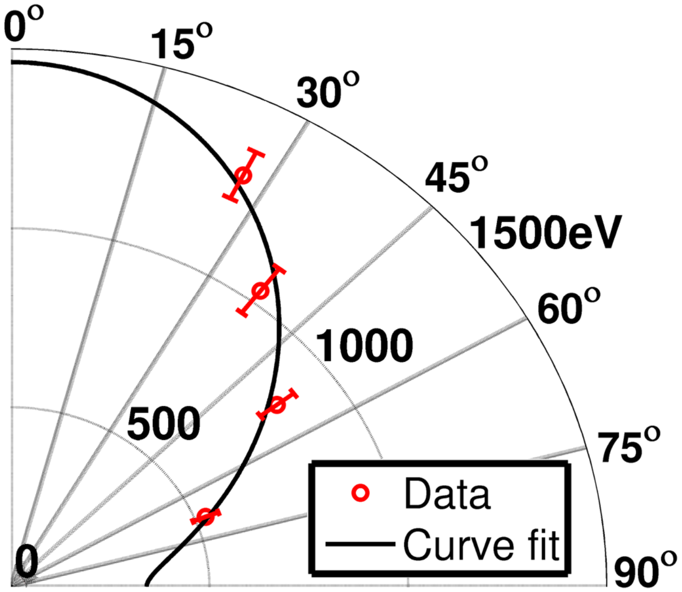

(c) Polar plot of mean ion energy

Figure 5.6: Angular distribution of ion energies from a CO_2 LPP in parameter space of Table 5.3.

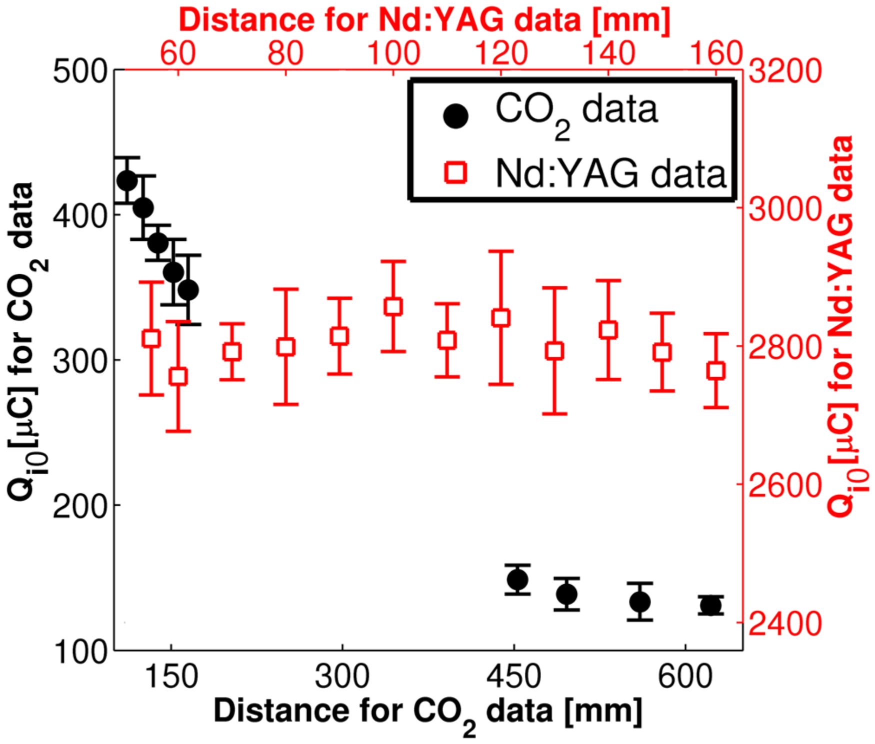

Figure 5.7: Q_{i0} as a function of distance from the Faraday cup to the target. Solid circles represent data using the CO_2 laser; open squares represent data using the Nd:YAG laser. Each data point is the average at least 15 shots. For the Nd:YAG data Q_{i0} is constant within the error bars implying the critical distance is less than 55 mm. For the CO_2 data Q_{i0} is decaying over both spatial intervals investigated, implying the critical distance is greater than 622 mm.

distance is less than 55 mm using the Nd:YAG laser. The exact critical distance could not be measured as the Faraday cup could not be scanned any closer to the target due to power limitations and eventually breakdown within the Faraday cup. The laser intensity used in this experiment ($8.3 \times 10^{11}\,\mathrm{W/cm^2}$) is a few times higher than the optimal laser intensity at this wavelength for the EUV x-ray source application ($\approx 2 \times 10^{11}\,\mathrm{W/cm^2}$) [74], however the scaling law for critical distance [Eqn. (5.8)] predicts at lower laser intensities (lower electron temperature) the critical distance will be even shorter [8]. As a result of the short critical distance, previous measurements of the charge state distribution recorded at distances of 100 cm from the target, should represent the charge state distribution as close as 55 mm from the target surface, which is shorter than the distance at which the x-ray collection optic will be located in a commercial EUV x-ray source.

In Figure 5.7, for the data obtained using the CO_2 laser, Q_{i0} was measured over two spatial intervals. From 112 mm to 165 mm a Faraday cup mounted on a translation stage inside the vacuum chamber was used, and from 453 mm to 622 mm a flange-mounted Faraday cup on a variety of vacuum extensions mounted on the chamber wall was used. The physical differences in the two Faraday cups (aperture size, grid transparency) were taken into account in comparing the data quantitatively. The faraday cup could not be scanned any closer to the target because it was blocked by the short focal length lens in the vacuum chamber, and other experimental apparatus blocked the Faraday cup from extending farther distances. Over both spatial intervals Q_{i0} has a negative slope, indicating the critical distance to be greater than 622 mm, in agreement with the theoretical prediction by Roudskoy [8] that L_{CR} should be on the order of meters for $\lambda \approx 10\,\mu\mathrm{m}$. About 4 to 5 times less charge was emitted from the CO_2 LPP as compared to the Nd:YAG LPP at the same distance, which is consistent with previous studies and due to decreased mass ablation at the longer laser wavelength [64] [20]. Due to the long critical distance of the CO_2 LPP, measurements of the ion charge state distribution at distances of 100 cm from the target [74] will not represent the actual distribution at distances closer to the target; the average ion charge state will be underestimated.

The data in Figure 5.7 obtained using the CO_2 laser can be used to infer the average ion charge state at the target surface in the following procedure. The vertical axis in Figure 5.7 is $Q_{i0}(L)$, representing the total charge emitted by the plasma into 2π sr, as measured at the distance L. If the total number of electrons contained in the plasma is N_e, and e is the electron charge, then $Q_{i0} = eN_e$. The average ion charge state is $\bar{Z} = N_e/N_0$, where N_0 is the total number of heavy atoms (ions and neutrals) contained in the plasma, which is a constant. Thus, $Q_{i0} = eN_0\bar{Z}$, and Q_{i0} is directly proportional to $\bar{Z}$. As a result, if Q_{i0} can be extrapolated to the target surface, then $\bar{Z}$ will vary in the same interval by the same amount.

The data in Figure 5.7 obtained using the CO_2 laser is reproduced in Figure 5.8, and includes a least squares curve fit that is extrapolated to the target surface. The data clearly contains two distinct decay rates, so a fitting function of the form

$$Q_{i0,fit}(d) = \lambda_1 \exp(\lambda_2 d) + \lambda_3 \exp(\lambda_4 d) \tag{5.11}$$

was chosen, where $Q_{i0,fit}$ approximates Q_{i0}, and λ_i, for $1 \leq i \leq 4$, are unique fitting parameters. The coefficient of determination of the fit to the data, R^2, as defined, e.g., in Rao [80], is 99.98%. The extrapolated value of Q_{i0} at the target surface is approximately 5 times the value measured in the far expansion zone.

The average ion charge state 100 cm from the laser plasma source can be calculated in the same procedure as was used in Section 5.1.1. The charge state distribution measured with the ion probe discussed in Chapter 3 is shown in Figure 5.9, and the average ion charge state calculated from the data is $\bar{Z} = 3 \pm 1$, where the error is due to insufficient resolution of the peak of the $Z = +1$ ion energy distribution. An estimate of the average ion charge state at the target surface is 5 times the value measured in the far expansion zone, as Q_{i0} varies by the same amount in the same interval. Thus, an average ion charge state of approximately 15 near the target surface is estimated from the ion properties measured here, which is in agreement with detailed atomic modeling of Sn plasma by Sasaki, *et al.* [96].

An additional implication of the greater than order of magnitude difference in critical distance for the two laser plasmas studied here, is that electrostatic and magnetostatic fields should be more effective at mitigating ions from Sn plasma produced by longer laser wavelengths, in which the plasma retains its high charge state ions over long distances from the target. Published experimental data on the effectiveness of magnetic field mitigation as a function of laser wavelength is not conclusive at this time as to

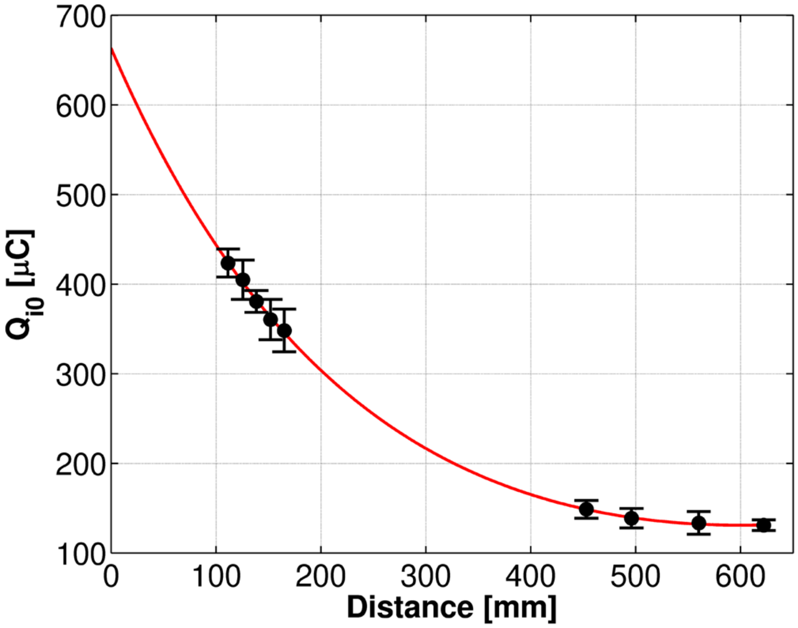

Figure 5.8: A function given by Equation (5.11) is fit in a least squares sense to the data contained in Figure 5.7 obtained using the CO_2 laser, and extrapolated to the target surface.

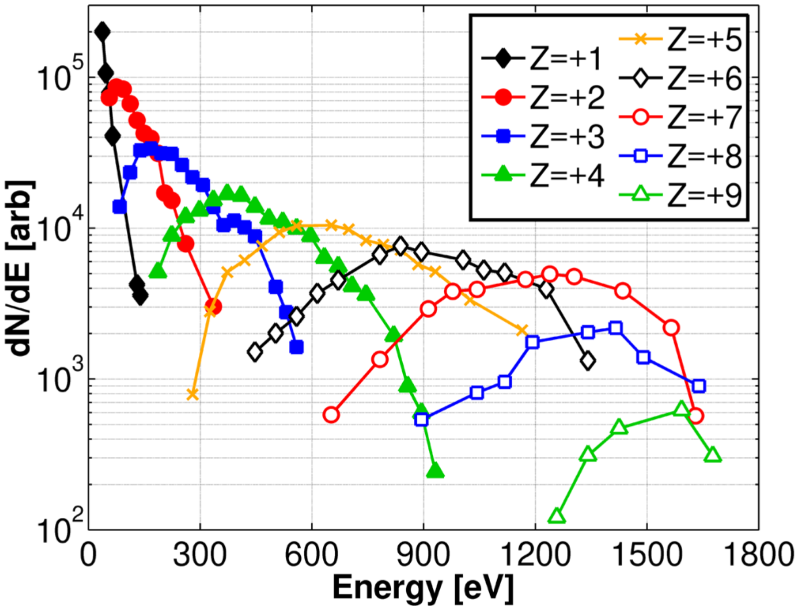

Figure 5.9: Charge-state resolved ion energy distribution measured at a distance of 100 cm from a Sn target irradiated by a CO_2 laser in parameter space summarized in Table 5.3.

which wavelength is best [28] [99]. More detailed experimental comparisons should be carried out to clarify this point.

5.3 Summary of Experimental Results

Several experiments were conducted to investigate the effects of laser wavelength on ion properties from laser produced Sn plasma. At wavelengths of 1.064 µm and 10.6 µm, in parameter space summarized in Table 5.1, the ion energy distribution in the far expansion zone was measured with the ion probe discussed in Chapter 3. Also at both laser wavelengths, in parameter space summarized in Table 5.3, a Faraday cup scanned along the path of plasma expansion was used to measure the distance over which the charge state distribution evolves. The measurements in the far expansion zone were used to infer plasma properties near the target surface. Results are summarized in the following list.

- At both laser wavelengths, ion energies increase approximately linearly as a function of charge state, and all ion energies greatly exceed the initial thermal electron temperature.
- An electrostatic model of ion acceleration [90] [92] qualitatively describes the observed relation between ion energies and charge states.
- Electron temperature, T_e, within the hot plasma can be estimated by fitting an electrostatic model to the data, as described by Equation (5.5). By this procedure, for the CO_2 LPP, $T_e \approx 40\,\text{eV}$, and for the Nd:YAG LPP, $T_e \approx 50\,\text{eV}$.
- At the longer laser wavelength, higher charge state ions are measured in the far expansion zone. This is due to enhanced three-body recombination in the plasma created by the shorter wavelength radiation.
- T_e within the hot plasma can also be estimated in a hydrodynamic model of the laser plasma interaction [84], using quantities calculated from the ion energy distributions measured in the far expansion zone. By this procedure, for the CO_2 LPP, $T_e \approx 37\,\text{eV}$, and for the Nd:YAG LPP, $T_e \approx 57\,\text{eV}$.

- The distance over which the charge state distribution evolves, L_{CR}, is less than 55 mm for Sn plasma produced by a 1.064 µm laser, but greater than 622 mm for Sn plasma produced by a 10.6 µm laser.

- For the CO_2 LPP, the measured decay in Q_{i0}, as described by Equations (5.6) and (5.7), and the measured ion energy distribution in the far expansion zone, as shown in Figure 5.9, can be used to estimate the average ion charge state, $\bar{Z}$, at the target surface. By this procedure, $\bar{Z} \approx 15$ was calculated from the data, which is in agreement with previous theoretical work [96].

Chapter 5, in part, has been published in both Journal of Applied Physics **107** 043303 (2010) and Applied Physics Letters **97** 041502 (2010). The dissertation author was the primary investigator and author of both articles. Contributing to the Journal of Applied Physics article were Yezheng Tao, Mark Tillack, Sam Yuspeh, and Farrokh Najmabadi of the Center for Energy Research at the University of California, San Diego. Nek M. Shaikh of the University of Sindh in Pakistan, and Eli Flaxer of the Tel-Aviv Academic College of Engineering in Israel also were contributing authors. The Applied Physics Letters article in 2010 was co-authored by Yoshifumi Ueno of Komatsu Corporation in Japan, in addition to Yezheng Tao, Sam Yuspeh, Mark Tillack, and Farrokh Najmabadi of the Center for Energy Research at the University of California, San Diego.

Chapter 6

Analytical Models of Ion Expansion into Vacuum

Analytical models of ion expansion into vacuum, in varying levels of complexity, can be used to provide insight into the physical mechanisms responsible for the observed features in the experiments discussed in Chapter 5. An adiabatic model of ion expansion will be shown to predict complete recombination in the far expansion zone. Only a non-adiabatic model, in which a source of energy is included in the analysis, can predict negligible recombination in the far expansion zone, as observed in the experiments.

6.1 Adiabatic Expansion

The decay of temperature, density, and average charge state in space and time can be calculated within an adiabatic model of ion expansion into vacuum. The underlying assumption of the adiabatic model is that internal energy balances the work done by the plasma pressure in a thermally closed system, i.e.,

$$\frac{d\varepsilon}{dt} + p\frac{dV}{dt} = 0, \tag{6.1}$$

where ε is the internal plasma energy, V is the plasma volume, and p is the plasma pressure. Under the ideal gas approximation,

$$p = n_i T_i + n_e T_e, \tag{6.2}$$

where n_i is the number density of ions (including neutrals), T_i is the ion temperature, n_e is the number density of electrons, and T_e is the electron temperature (all temperatures are in energy units). If the plasma is neutral, i.e., $n_e = \bar{Z}n_i$, and if electron and ion temperatures are equal, then

$$p = n_i\,(1+\bar{Z})\,T_e. \tag{6.3}$$

The internal plasma energy is given by

$$\varepsilon = \tfrac{3}{2}T_eN_e + \tfrac{3}{2}T_iN_i, \tag{6.4}$$

where N_e and N_i are the number of electrons and ions, respectively. Under the assumption of plasma neutrality, and equal ion and electron temperatures,

$$\varepsilon = \tfrac{3}{2}T_eN_i\,(1+\bar{Z})\,. \tag{6.5}$$

Equations (6.3) and (6.5) can be applied to Equation (6.1) and manipulated to obtain

$$\frac{dT_e}{T_e} = \frac{2}{3}\frac{dn_i}{n_i}, \tag{6.6}$$

which can be integrated to give

$$T_e(t) = T_{e0}\left(\frac{n_i}{n_{i0}}\right)^{2/3}, \tag{6.7}$$

where n_{i0} and T_{e0} are the constant initial ion density and electron temperature, respectively, at time $t = t_0$. During the laser pulse, laser energy is transferred into random thermal energy of electrons, and thus the subsequent expansion into vacuum will be approximately spherical. Accordingly, the decay of ion density in space will follow the equation

$$n_i(r) = n_{i0}\left(\frac{r}{r_0}\right)^{-3}, \tag{6.8}$$

where r is a radial spatial coordinate, increasing away from the target, and r_0 is the radius at $t = t_0$. Measurements from Faraday cups at different positions along the path of plasma expansion, such as in Section 5.2, demonstrate an approximately constant expansion speed far from the target surface. A constant expansion speed implies $r \propto t$, so that Equation (6.8) can be rewritten as

$$n_i(t) = n_{i0}\left(\frac{t}{t_0}\right)^{-3}. \tag{6.9}$$

Finally, Equation (6.9) can be combined with Equation (6.7) to obtain the temporal decay of electron temperature in the adiabatic model,

$$T_e(t) = T_{e0}\left(\frac{t}{t_0}\right)^{-2}. \tag{6.10}$$

6.1.1 Recombination in the Adiabatic Model

Collisional-radiative recombination in laser produced plasma involves the recombination of an electron with an ion in the presence of a third body to conserve energy. The third body can be a photon, as in radiative recombination, or an electron, as in three-body recombination. Collisional-radiative recombination can be treated within a single theory [100], although the processes of radiative recombination and three-body recombination can be decoupled for simplicity [81] [82]. As previously discussed in Section 5.1.2, three-body recombination will be the dominant mechanism throughout expansion into vacuum. An analytical expression for the three-body recombination rate can be derived [82], and is given by

$$\Re_Z^t = (8.75\times 10^{-27})\,Z^3\, n_e\, T_e^{-9/2} \quad [\mathrm{cm}^3/\mathrm{sec}], \tag{6.11}$$

where Z is the charge state of the recombining ion, n_e has units of cm^{-3}, and T_e has units of eV. The rate at which the number density of electrons is decaying due to three-body recombination is then given by

$$\begin{aligned} \frac{dn_e}{dt} &= -\Re_Z^t\, n_e\, n_i \\ &\propto T_e^{-9/2}\, n_e^2\, n_i. \end{aligned} \tag{6.12}$$

If the temporal decay of density and temperature, as given by Equations (6.9) and (6.10), are combined with the preceding equation for the rate of decay of electron density, it is found that

$$\frac{dn_e}{dt} \propto \left(t^{-2}\right)^{-9/2}\left(t^{-3}\right)^{3} \propto \text{constant}. \tag{6.13}$$

The result is that the initial rate of decay of electron density due to three-body recombination will persist throughout an adiabatic expansion, eventually resulting in complete recombination. The same result can also be noticed by looking at the temporal scaling of the electron-ion collision frequency, $\nu_{ei} \propto n_e\, T_e^{-3/2}$. If the temporal decay of density and temperature for an adiabatic expansion are inserted into the scaling equation for ν_{ei}, it is found that the collision rate is a constant. The result is again, that a plasma expanding adiabatically from an initially collisional state, will remain collisional throughout the expansion, resulting in complete recombination. The fact that high charge state ions can be measured in the far expansion of laser produced plasma implies the expansion must be non-adiabatic.

In addition, the temporal decay of average ion charge state, $\bar{Z}$, in the adiabatic model can also be calculated. If the assumption of plasma neutrality, $n_e = \bar{Z} n_i$, is combined with the equation for the rate of decay of electron density [Eqn. (6.12)], a differential equation for the rate of decay of $\bar{Z}$ is obtained,

$$\frac{d\bar{Z}}{dt} = -(8.75 \times 10^{-27})\,\frac{\bar{Z}^5}{T_e^{9/2}}\,n_i^2. \tag{6.14}$$

As before, the equations for the temporal decay of density and temperature in the adiabatic model [Equations (6.9) and (6.10)] can be combined with the preceding equation for the rate of decay of $\bar{Z}$, and manipulated, to obtain

$$\frac{d\bar{Z}}{\bar{Z}^5} = -(8.75 \times 10^{-27})\,\frac{n_{i0}^2}{T_{e0}^{9/2}}\left(\frac{t}{t_0}\right)^3 dt\,. \tag{6.15}$$

Finally, Equation (6.15) can be integrated to obtain the temporal decay of $\bar{Z}$ in the adiabatic model, given by

$$\bar{Z}(t) = \bar{Z}_0 \kappa^{-1/4}\left[\left(\frac{t}{t_0}\right)^4 + \frac{1}{\kappa} - 1\right]^{-1/4}, \tag{6.16}$$

where $\bar{Z}_0$ is the average ion charge state at $t = t_0$, and the constant κ is

$$\kappa = (8.75 \times 10^{-27})\frac{n_{i0}^2\, t_0\, \bar{Z}_0^4}{T_{e0}^{9/2}}. \tag{6.17}$$

For $t \gg t_0$, the expression for $\bar{Z}(t)$ simplifies to

$$\bar{Z}(t) = \bar{Z}_0\, \kappa^{-1/4}\left(\frac{t}{t_0}\right)^{-1}, \tag{6.18}$$

implying that the average ion charge state will decay to zero in the far expansion zone within the adiabatic model.

6.2 Non-adiabatic Expansion

The non-adiabatic model of ion expansion into vacuum assumes the general form of the energy equation [93],

$$\frac{d\varepsilon}{dt}+p\frac{dV}{dt}=Q, \tag{6.19}$$

which differs from Equation (6.1) due to the inclusion of a source term, Q. The excess energy of three-body recombination, which goes into the free electron population, is the source term in the non-adiabatic model. During three-body recombination, a free electron in a continuum energy state recombines with an ion into a discrete energy level, so that an excess energy, E^*, is transferred to the third body, in this case another free electron. The maximum amount of energy given to the free electron is the ionization potential for the corresponding charge state and ion species. The exact amount of excess energy can be derived by balancing the rates of collisional and radiative descent of an electron captured by an ion into a high excited state, as discussed in detail in Kuznetsov and Raizer [86]. The expression for E^* derived in Ref. [86], and used by many subsequent authors in their calculations [93] [88] [101] [102], is given by

$$\left(\frac{E^*}{\mathrm{eV}}\right)=(1.1\times 10^{-3})\,Z^{2/3}\left(\frac{n_e}{\mathrm{cm}^{-3}}\right)^{1/6}\left(\frac{T_e}{\mathrm{eV}}\right)^{1/12}. \tag{6.20}$$

The source term, Q, in Equation (6.19) is related to E^* through the three-body recombination rate [Eqn. (6.11)], as given by

$$Q=\Re_Z^t\,n_e\,N_i\,E^*, \tag{6.21}$$

where the units of Q are energy per unit time. Including the source term, using the ideal gas approximation, and assuming plasma neutrality, the energy equation [Eqn. (6.19)] can be manipulated to obtain a non-linear differential equation for electron temperature,

$$\frac{dT_e}{dt}=-2\frac{T_e}{t}-\frac{d\bar{Z}/dt}{1+\bar{Z}}\left(\frac{2}{3}E^*+T_e\right). \tag{6.22}$$

Together, Equations (6.22), (6.14), and (6.6) represent a coupled, nonlinear set of first-order differential equations for n_i, T_e, and $\bar{Z}$ which can be integrated numerically. A typical example of the temporal evolution of T_e and $\bar{Z}$ is shown in Figure 6.1. The important results from the figure are that, in a nonadiabatic expansion, electron temperature decays with time initially as t^{-2}, but transitions later in time to a t^{-1} decay. The average ion charge state, $\bar{Z}$, decays early in time, but later approaches a constant, nonzero value, supporting the experimental results from Section 5.1.1. The asymptotic behavior of T_e and $\bar{Z}$ in a nonadiabatic expansion under similar initial conditions, has been investigated by other authors as well, through numerical simulation [86], and by an analytical approach [8] [103], where the same general features in the decay of T_e and $\bar{Z}$ are derived.

The temporal scaling of the collision frequency and the rate of decay of electron density in the non-adiabatic model, provide insight into the simulation results in Figure 6.1. If $T_e \propto t^{-1}$ and $n_i \propto t^{-3}$ are combined with Equation (6.12) for the rate of decay of electron density, it is found that

$$\frac{dn_e}{dt} \propto \left(t^{-1}\right)^{-9/2} \left(t^{-3}\right)^{3} \propto t^{-9/2}, \tag{6.23}$$

that is, eventually in the expansion the electron population will no longer decay due to three-body recombination. The electron-ion collision frequency, $\nu_{ei} \propto n_e T_e^{-3/2}$, scales in the non-adiabatic model as $\nu_{ei} \propto t^{-3/2}$, implying that eventually the plasma will become collisionless and thus collisional recombination will be negligible.

In summary, the non-adiabatic model differs from the adiabatic model in that a source term due to excess energy released in three-body recombination must be included in the analysis. The effect of the source term is to slow the adiabatic, t^{-2} decay of electron temperature to a t^{-1} decay after some initial expansion. This results in $\bar{Z}$ approaching a nonzero value in its asymptotic limit, as well as in the collision frequency, and the rate of decay of electron density due to recombination, decaying with time. For these reasons, the experimental results in Chapter 5 can only be described in a non-adiabatic model of ion expansion into vacuum. Numerical simulations of Sn plasma in a non-adiabatic model are described in the subsequent chapter.

Chapter 6, in part, has been published in Journal of Applied Physics **107** 043303 (2010). The dissertation author was the primary investigator and author of the article. Contributing were Yezheng Tao, Mark Tillack, Sam Yuspeh, and Farrokh Najmabadi of the Center for Energy Research at the University of California, San Diego. Nek M. Shaikh of the University of Sindh in Pakistan, and Eli Flaxer of the Tel-Aviv Academic

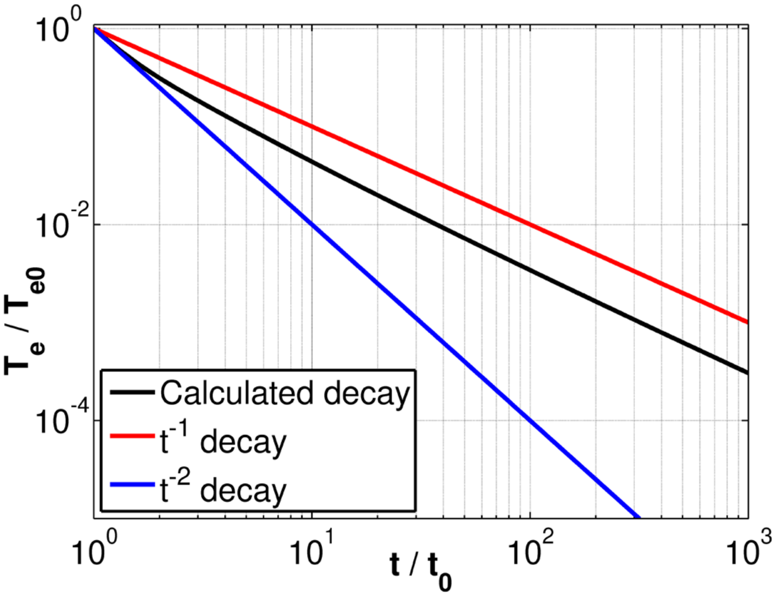

(a) Decay of T_e in the nonadiabatic model.

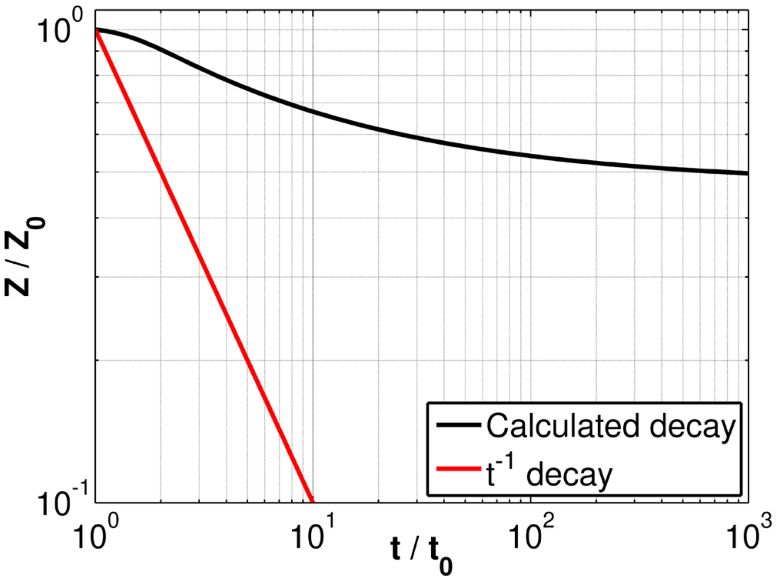

(b) Decay of $\bar{Z}$ in the nonadiabatic model.

Figure 6.1: Decay of T_e and $\bar{Z}$ in the nonadiabatic model. The initial conditions for the simulation are $n_{i0} = 10^{18}\,\mathrm{cm}^{-3}$, $T_{e0} = 40\,\mathrm{eV}$, $\bar{Z}_0 = 10$, and $t_0 = 10\,\mathrm{ns}$. Some authors claim that under all initial conditions, the limiting value for $\bar{Z}$ will be nonzero [8], whereas other authors claim that in certain cases the plasma can recombine completely in the nonadiabatic model [86]. In any case, under a range of initial conditions relevant to the present experiments, the limit of $\bar{Z}$ always approaches a nonzero value.

College of Engineering in Israel also were contributing authors.

Chapter 7

Numerical Models of Ion Expansion into Vacuum

In the previous chapter, analytical models of ion expansion into vacuum were described, with the conclusion that only a non-adiabatic model could predict incomplete recombination in the far expansion zone, as observed in the experiments. In this chapter, the non-adiabatic model is applied to the specific case of a laser-produced Sn plasma, in parameter space relevant to the extreme ultraviolet x-ray source application. A zero-dimensional (0D) model is discussed first, in which the time evolution of the electron population, electron and ion temperatures, and all ion populations are simulated. The results of the 0D model verify some of the features observed in the experiments, however ion energy distributions cannot be calculated within a 0D model, and therefore a one-dimensional (1D) model is also implemented. The 1D model uses the 0D model as a component in its algorithm, and combines Lagrangian hydrodynamics to follow the expansion of the domain over several orders of magnitude. The ion energy distributions simulated in the 1D model only qualitatively reproduce the features observed in the experiments, due to imprecise initial conditions and the many assumptions in the code.

7.1 Background and Literature Review

Numerical simulations of plasma expansion into vacuum from an assumed initial state can be used to provide insight into the physical mechanisms responsible for the observed ion energy distributions far from the laser plasma source. The decay of an ionized H gas cloud into vacuum was first investigated by Kuznetsov and Raizer [86], in which the freezing of average ion charge state in the far expansion zone was demonstrated. Those simulations were subsequently extended to the case of a fully-ionized Al plasma by Voronov and Chernyshev [88], and to a multi-species SiO_2 plasma by Goforth and Hammerling [101], where both models were zero-dimensional. In each of these previous models, the transition in the decay of electron temperature with time from t^{-2} to approximately t^{-1}, and freezing of the average ion charge state, were both observed. One-dimensional models, such as those for a LiH plasma in Mattioli [87], and for a C plasma in Kunz [104], are able to simulate recombination effects within different plasma regions having different velocities, enabling better agreement with experiment. Finally, computationally expensive, two-dimensional simulations, such as those in Roudskoy [8] and Baranov, *et al.* [105], are able to quantitatively reproduce experimental data recorded by ion probes for high-Z plasma produced by 1 µm to 10 µm radiation, for intensities below $10^{15}/\lambda^2$ W/cm^2, where λ is the laser wavelength in µm. These multi-dimensional codes are typically used in the development of laser ion sources generating an optimal yield of high charge state and high energy ions for accelerator applications [31] [106].

7.2 Collisional-Radiative Steady State Model

The initial conditions used in simulations of ion expansion into vacuum are typically assumed at a time when the laser heating has finished, in order to avoid complexities associated with modeling phenomena during the laser pulse, such as the short hydrodynamic time step. At the end of the laser pulse, the collisional-radiative (CR) model described in Colombant and Tonon [3] can be used to determine the local ionization distribution as a function of the local temperature and density of either electrons or ions. The CR model prevails when excitation balances de-excitation, and recombination balances ionization, in both collisional and radiative processes. The CR model can be applied to laser-produced plasma at $n_e = 10^{21}\,\mathrm{cm}^{-3}$ for $T_e \geq 10\,\mathrm{eV}$, and at $n_e = 10^{19}\,\mathrm{cm}^{-3}$ for $T_e \geq 3\,\mathrm{eV}$ [3] (n_e is electron density, T_e is electron temperature) – conditions which are satisfied in coronal Sn plasma relevant to the EUV x-ray source application. Indeed, other authors modeling laser-produced Sn plasmas have employed the CR model in their calculations [107] [108]. The equations defining the CR model satisfy the steady-state condition for n_k, the number density of k-times ionized Sn atoms, given by

$$\begin{aligned}\frac{dn_k}{dt} = &+ n_e\, n_{k-1} S(k-1) \\ &- n_e\, n_k \left[S(k) + \alpha_r(k) + n_e\, \alpha_{3b}(k)\right] \\ &+ n_e\, n_{k+1} \left[\alpha_r(k+1) + n_e\, \alpha_{3b}(k+1)\right] = 0.\end{aligned} \tag{7.1}$$

Increases in the population of charge state k are due to collisional ionization in the $k-1$ state, as expressed by the first term, and by radiative and three-body recombination in the $k+1$ state, as expressed by the third term. Depopulation of charge state k is due to ionization into the $k+1$ state, and recombination into the $k-1$ state, as expressed by the second term. The plasma is assumed optically thin in the CR model, so that photoionization is not included in the model. The atomic rates for collisional ionization, S, in $[\mathrm{cm}^3/\mathrm{s}]$, radiative recombination, α_r, in $[\mathrm{cm}^3/\mathrm{s}]$, and three-body recombination, α_{3b}, in $[\mathrm{cm}^6/\mathrm{s}]$, are given in Colombant and Tonon [3], and depend upon the charge state, k, the local electron temperature, and atomic data. Ionization potentials for all charge states of Sn, as required in the atomic rate calculations, are tabulated in Cummings, *et al.* [16], and in Carlson, *et al.* [109]. Additional data required in the atomic rate calculations include the ion mass, and the number of outershell electrons as a function of ionization state, which is obtained from the electron configuration for a Sn atom [110].

Equation (7.1) can be manipulated to obtain a recurrence relation between adjacent ionization levels,

$$\frac{n_{k+1}}{n_k} = \frac{S(k)}{\alpha_r(k+1) + n_e \alpha_{3b}(k+1)}, \tag{7.2}$$

so that if the local electron temperature, electron density, and atomic data are known, Equation (7.2) can be used to obtain the fractional ionization distribution explicitly. However, in calculating the initial conditions for the one-dimensional simulations, the local ion density (including neutrals), n_H, is known, rather than the local electron density, which complicates the calculation of the ionization distribution. A similar problem has been solved by Zaghloul, *et al.* [111] to obtain a solution to the Saha equation when the electron density is not given explicitly, and the general method will be applied here for the CR model. The fractional population of charge state k is α_k, where $\alpha_k = n_k/n_H$, and $\sum_{k=0}^{Z} \alpha_k = 1$, where Z is the highest charge state ion present in the plasma (not necessarily the atomic number). The average ion charge state, $\bar{Z}$, is then

$$\bar{Z} = \sum_{k=1}^{Z} k\,\alpha_k, \tag{7.3}$$

and the plasma neutrality condition implies $n_e = \bar{Z} n_H$. Equation (7.2) can then be manipulated to obtain

$$\alpha_{k+1} = \alpha_k \frac{S(k)}{\alpha_r(k+1) + \bar{Z} n_H\, \alpha_{3b}(k+1)} = \alpha_k f_{k+1}, \tag{7.4}$$

or, alternatively,

$$\alpha_k = \alpha_0 \prod_{i=1}^{k} f_i, \tag{7.5}$$

where the definition of f_i is contained in Equation (7.4). The preceding equation can be combined with Equation (7.3) to obtain

$$\alpha_0 = \bar{Z} \left(\sum_{k=1}^{Z} k \prod_{i=1}^{k} f_i \right)^{-1}. \tag{7.6}$$

If the condition $\sum_{k=0}^{Z} \alpha_k = 1$ is put in the form

$$1 - \left(\sum_{k=1}^{Z} \alpha_k \right) - \alpha_0 = 0, \tag{7.7}$$

and Equations (7.5) and (7.6) are substituted, a single transcendental equation for $\bar{Z}$ is obtained, given by

$$1 - \bar{Z} \left(\sum_{k=1}^{Z} k \prod_{i=1}^{k} f_i \right)^{-1} \left[1 + \sum_{k=1}^{Z} \prod_{i=1}^{k} f_i \right] = 0, \tag{7.8}$$

where it is noted that $f_i = f_i(\bar{Z}, n_H, k, T_e)$, in addition to dependence on atomic data. The transcendental equation for $\bar{Z}$ can be solved easily using an implicit method, α_0 can subsequently be calculated explicitly using Equation (7.6), and finally α_k for $1 \leq k \leq Z$ can all be calculated using Equation (7.5). By this procedure, the entire fractional ionization distribution can be calculated without explicit knowledge of the local electron density.

Some examples of fractional ionization distributions for Sn plasma calculated using the CR model are shown in Figure 7.1. In each example, electron temperature is scanned from 10 eV to 100 eV, and in Figure 7.1a the electron density is held constant at $n_e = 10^{20}\,\mathrm{cm}^{-3}$, whereas in Figure 7.1b the ion density is held constant at $n_H = 10^{20}\,\mathrm{cm}^{-3}$.

7.3 Zero-Dimensional Simulations of Ion Expansion into Vacuum

A set of nonlinear, coupled differential equations based on the non-adiabatic model described in Chapter 6, is described here to model the time evolution of Sn plasma during its expansion into vacuum. The objective of the simulations is to reproduce some of the experimental observations summarized in Section 5.3 in a simple, zero-dimensional model. The initial conditions used for the model correspond to an assumed initial state of Sn plasma produced by both a Nd:YAG and CO_2 laser, in parameter space of the experiments described in Chapter 5.

7.3.1 Initial Conditions

Several assumptions are required to model ion expansion into vacuum from a laser-produced Sn plasma in a simple, zero-dimensional model. As discussed previously, the laser heats plasma electrons, and electrons transfer energy to ions on the scale of the electron-ion thermalization time, τ_{ei}, given by

$$(\tau_{ei}/s) \approx \left(3.5\times10^{8}\right)\frac{(A/amu)\,(T_e/eV)^{3/2}}{\bar{Z}\,(n_e/\mathrm{cm}^{-3})\ln\Lambda}, \tag{7.9}$$

where A is the atomic mass (118.71 amu for Sn), and $\ln\Lambda$ is the Coulomb logarithm (≈ 5 for laser plasma) [93]. The simulation begins at a time t_0 when electrons and ions have thermalized, and the exact value $t_0 = 2\,\tau_{ei}$ was used. The plasma at $t = t_0$ is assumed to be spherical, with homogeneous properties, and an initial diameter equal to the laser focal diameter. Indeed, soft x-ray imaging of laser-produced Sn plasma confirms the initial plasma size to be approximately equal to the laser focal diameter [112].

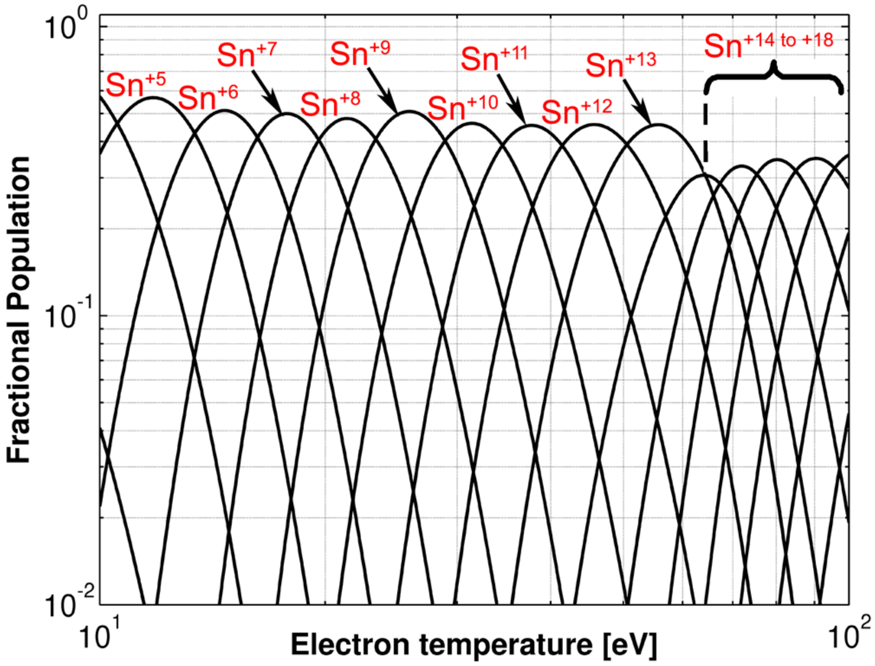

(a) Fractional ionization distribution for $n_e = 10^{20}\,\mathrm{cm}^{-3}$

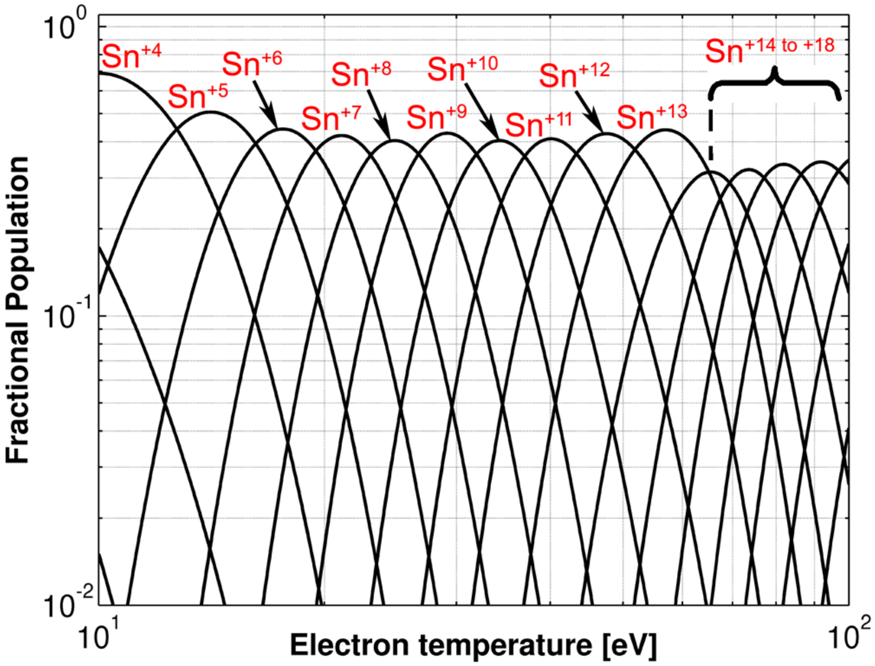

(b) Fractional ionization distribution for $n_H = 10^{20}\,\mathrm{cm}^{-3}$

Figure 7.1: Fractional ionization distributions for Sn plasma calculated using the CR model [3].

Table 7.1: Initial conditions used in the 0D simulations, λ_L is the laser wavelength.

λ_L	$n_{e,0}$	$T_{e,0}$	Ion Population Fractions								
[μm]	[cm^{-3}]	[eV]	+9	+10	+11	+12	+13	+14	+15	+16	$\bar{Z}_0$
1.064	10^{21}	60			0.02	0.17	0.42	0.27	0.10	0.02	13.3
10.6	10^{19}	40	0.02	0.14	0.43	0.34	0.07				11.3

The initial electron density, $n_{e,0}$, and electron temperature, $T_{e,0}$, within the plasma are set according to the two laser wavelengths which are modeled. As discussed previously, the initial density will approximately equal the critical density, so for a laser wavelength of 1.064 μm, $n_{e,0} = 10^{21}\,\mathrm{cm}^{-3}$, and for a laser wavelength of of 10.6 μm, $n_{e,0} = 10^{19}\,\mathrm{cm}^{-3}$. The experimental results in Chapter 5 indicated the initial electron temperature to be higher at the shorter laser wavelength, which has subsequently been confirmed by other authors using a different diagnostic approach [113]. Accordingly, for a laser wavelength of 1.064 μm, $T_{e,0} = 60\,\mathrm{eV}$, and for a laser wavelength of 10.6 μm, $T_{e,0} = 40\,\mathrm{eV}$.

At each laser wavelength, the initial conditions for $T_{e,0}$ and $n_{e,0}$ can be used to calculate the initial fractional ionization distribution by the procedure described in Section 7.2. From the initial ionization distribution, the initial average ion charge state, $\bar{Z}_0$ can also be calculated. A summary of these initial conditions at both laser wavelengths is given in Table 7.1. The electron-thermalization time, τ_{ei} can be calculated using the data in the table, and t_0 for the simulation is twice this value. Therefore, at a laser wavelength of 1.064 μm, $\tau_{ei} = 290\,\mathrm{ps}$ and $t_0 = 580\,\mathrm{ps}$; and at a laser wavelength of 10.6 μm, $\tau_{ei} = 19\,\mathrm{ns}$ and $t_0 = 38\,\mathrm{ns}$.

7.3.2 Model Ordinary Differential Equations

The boundary of the initial domain is assumed to expand spherically for all time at a constant speed equal to the plasma sound speed, given by

$$c_{S,0} = \sqrt{\frac{\bar{Z}_0\, T_{e,0}}{M_i}}, \tag{7.10}$$

where M_i is the ion mass. For $\lambda_L = 1.064\,\mu\text{m}$, the sound speed is $c_{S,0} = 2.5 \times 10^6\,\text{cm/s}$, whereas for $\lambda_L = 10.6\,\mu\text{m}$, the sound speed is $c_{S,0} = 1.9 \times 10^6\,\text{cm/s}$. At any time t in the simulation, the radius of the domain will be $R = c_{S,0}\,t$.

A set of ordinary differential equations (ODEs) are solved to determine the plasma dynamics for $t > t_0$. Rate equations for the number of ions in each charge state are given by

$$\frac{dN_k}{dt} = \left(\frac{dN_k}{dt}\right)_c + \left(\frac{dN_k}{dt}\right)_r + \left(\frac{dN_k}{dt}\right)_i, \tag{7.11}$$

where the subscript k takes values from 0 (representing the neutral population) to $+Z$ (the highest ionization state within the plasma). The subscript c refers to the rate of change of N_k due to three-body recombination, r to radiative recombination, and i to collisional ionization. The three-body recombination rate is derived in Gurevich and Pitaevskiĭ [82], whereas the radiative recombination rate in Allen [81] and the collisional ionization rate in McWhiter [114] both represent empirical fits to a compilation of experimental data. All of these atomic rates have since been used by many authors in similar calculations, e.g., [8] [88] [101] [103] [105]. Using these atomic rates for the various processes considered, the terms in Equation (7.11) can be written as

$$\left(\frac{dN_k}{dt}\right)_c = (8.8 \times 10^{-27})\, n_e^2 T_e^{-9/2} \left[(k+1)^3 N_{k+1} - k^3 N_k\right] \tag{7.12}$$

$$\left(\frac{dN_k}{dt}\right)_r = (2.7 \times 10^{-13})\, n_e T_e^{-3/4} \left[(k+1)^2 N_{k+1} - k^2 N_k\right] \tag{7.13}$$

$$\left(\frac{dN_k}{dt}\right)_i = (2.4 \times 10^{-6})\, n_e T_e^{1/4} \left[\frac{\xi_{k-1}}{I_{k-1}^{7/4}} \exp\left(-\frac{I_{k-1}}{T_e}\right) N_{k-1} - \frac{\xi_k}{I_k^{7/4}} \exp\left(-\frac{I_k}{T_e}\right) N_k\right], \tag{7.14}$$

where $[dN_k/dt] = \text{s}^{-1}$, $[n_e] = \text{cm}^{-3}$, and $[T_e] = \text{eV}$. The ionization potential for charge state k is I_k in units of [eV], and the number of outershell electrons for charge state k is ξ_k. Each term represents both population and depopulation of the charge state k. For the neutral state, terms representing recombination into lower states and ionization from lower states must clearly be omitted; a similar modification is necessary for the highest ionization state considered.

The preceding rate equations represent a set of $Z+1$ ODEs in $Z+3$ independent variables (N_k for $0 \le k \le Z$, n_e, and T_e). At each time step, the total number of electrons,

N_e, is determined through the plasma neutrality condition, and $n_e = N_e/V$, where V is the plasma volume determined through the plasma radius at each time step.

For the simulation at each laser wavelength, t_0 is less than the laser pulse duration used in the corresponding experiment. To model the high thermal conductivity during the laser pulse, the electron temperature is held constant during the laser pulse duration, which is an assumption used by other authors in similar models of ion expansion into vacuum [88] [104]. The validity of this assumption is verified in the following procedure by estimating the electron temperature gradient length, $L_T \equiv T_e \,/\, \frac{\partial T_e}{\partial x}$, and comparing it to the laser focal diameter. In the steady-state ablation regime, as described in Section 1.1, the inward and outward heat fluxes will be balanced. The inward heat flux, Q_{in}, can be estimated as the heat flux due to classical conduction of thermal electrons [115],

$$Q_{in} = \kappa \frac{\partial T_e}{\partial x} \quad \left[\frac{\text{erg}}{\text{s cm}^2}\right], \tag{7.15}$$

where κ is the Spitzer thermal conductivity in units of [erg $\text{s}^{-1}\,\text{cm}^{-1}\,\text{K}^{-1}$], given by

$$\kappa = \left(2.83\times10^6\right)\frac{T_e^{5/2}}{Z\ln\Lambda}, \tag{7.16}$$

where T_e has units of [eV]. The outward heat flux, Q_{out}, can be estimated as [67]

$$Q_{out} = p\,c_S \quad \left[\frac{\text{erg}}{\text{s cm}^2}\right], \tag{7.17}$$

where p is the plasma pressure in units of [erg/cm^3], and c_S is the plasma sound speed in units of [cm/s]. By balancing Equations (7.15) and (7.17), and using expressions given previously for the plasma pressure [Eqn. (6.3)] and the plasma sound speed [Eqn. (7.10)], an estimate for the electron temperature gradient, L_T, can be derived,

$$L_T \approx \left(2\times10^{28}\right)\frac{T_e^2\sqrt{M_i}}{(1+Z)\ln\Lambda\, n_e} \quad [\text{cm}], \tag{7.18}$$

where $[T_e] = \text{eV}$, $[n_e] = \text{cm}^{-3}$, $M_i = 1.97\times10^{-22}\,\text{g}$ for a Sn atom, and $\ln\Lambda \approx 5$ for laser plasma. Applying the initial conditions summarized in Table 7.1, $L_T \approx 140\,\mu\text{m}$ for the simulation of the Nd:YAG LPP, and $L_T \approx 7300\,\mu\text{m}$ for the simulation of the CO_2 LPP. In each case, the estimate for the electron temperature gradient length exceeds the laser focal diameter, so that the assumption of constant electron temperature within the plasma at $t = t_0$ is reasonable. Finally, the estimate here of L_T for the CO_2 LPP is exceedingly large, which adds evidence in support of recent experiments suggesting that plasma expansion for a CO_2 LPP cannot be sufficiently described within a classical model [112].

The calculation of T_e at each time step, following the time duration when it is held constant, is where the non-adiabatic model is introduced. As discussed in Chapter 6, the full energy equation, including a source term representing the excess energy of three-body recombination, must be utilized to properly model ion expansion from laser-produced plasma. In the notation of the present chapter, the full energy equation can be written as

$$\frac{dT_e}{dt} = -\left(2\frac{T_e}{t}\right) - \left(\frac{2}{3}\frac{Q}{1+N_e/N_H}\right) \tag{7.19}$$

where $N_H = \sum_{k=0}^{Z} N_k$ is the total number of heavy atoms within the plasma. The source term due to the excess energy of three-body recombination, Q, in units of [eV/s], is given by

$$Q = \frac{1}{N_H}\sum_{k=1}^{Z} E_k^* \left[\left(\frac{dN_k}{dt}\right)_c + \left(\frac{dN_k}{dt}\right)_i\right], \tag{7.20}$$

where E_k^* in units of [eV] was given previously in Equation (6.20). The preceding equation for Q will be negative in a plasma that is recombining, so that the second term in Equation (7.19) will represent a source of energy.

At the start of the simulation, electron and ion temperatures are assumed equal, however this condition may not persist throughout the simulation. Differences in the two temperatures can be modeled by the addition of a temperature relaxation term to the energy equation. Accordingly, the energy equation for electrons becomes

$$\frac{dT_e}{dt} = -\left(2\frac{T_e}{t}\right) - \left(\frac{2}{3}\frac{Q}{1+N_e/N_H}\right) + \frac{T_i - T_e}{\tau_{ei}}, \tag{7.21}$$

where T_i is the ion temperature, and τ_{ei} is the electron-ion thermalization time given previously in Equation (7.9). An additional ODE is then required for the evolution of ion temperature, and its term include adiabatic expansion and temperature relaxation only, as given by

$$\frac{dT_i}{dt} = -\left(2\frac{T_i}{t}\right) + \frac{T_e - T_i}{\tau_{ei}}. \tag{7.22}$$

The previous equations represent a nonlinear set of coupled ODEs for the evolution of electron and ion temperatures, and all ion populations. A stiff algorithm must be

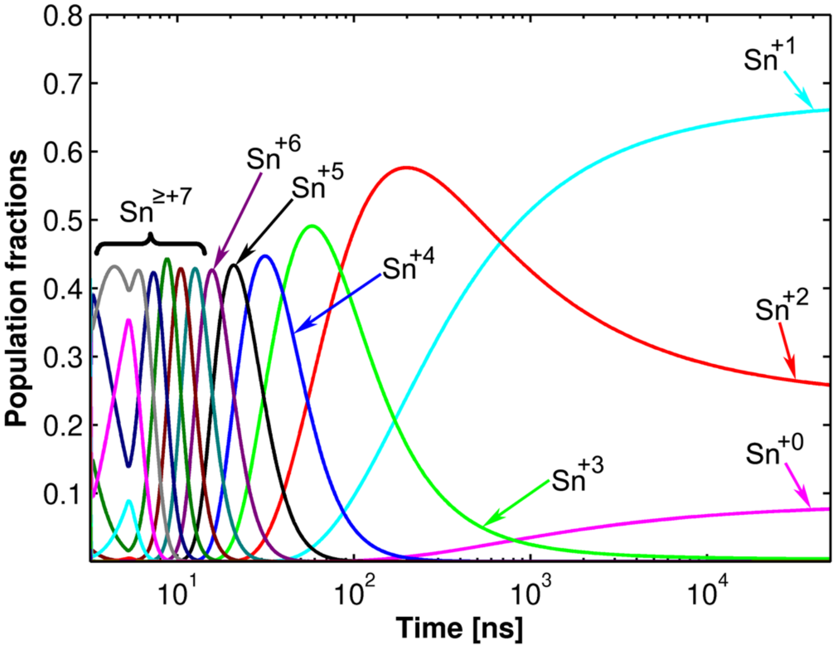

Figure 7.2: Temporal evolution of population fractions for each charge state of a Sn plasma produced by a 1.064 µm laser.

used to integrate the system due to the wide range of time scales characteristic of the various processes included. A commercial ODE solver, *ode15s* [116], in the MATLAB environment was utilized to integrate the equations.

7.3.3 Simulation Results

The 0D model was solved for initial conditions relevant to a Sn plasma produced by a 1.064 µm laser, as summarized in Table 7.1. The time evolution of the population fractions, from the initial values determined by the CR model, to a time at which the population fractions have stopped evolving, is shown in Figure 7.2. The main result from the figure is that after the initial charge state distribution undergoes considerable changes during expansion, it freezes into a state where the plasma consists primarily of Sn^{+0}, Sn^{+1}, and Sn^{+2} atoms. Freezing of the charge state distribution is due to the term in the electron energy equation representing the excess energy of three-body recombination, i.e., when the second term in Equation (7.21) is set to zero, the plasma always recombines completely.

The 0D model was also solved for initial conditions relevant to a Sn plasma

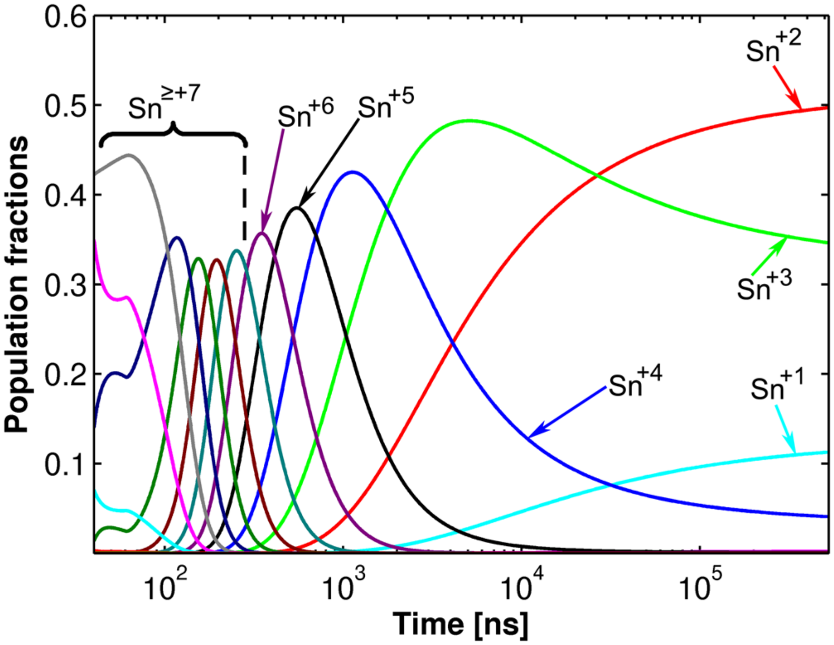

Figure 7.3: Temporal evolution of population fractions for each charge state of a Sn plasma produced by a 10.6 µm laser.

produced by a 10.6 µm laser, as summarized in Table 7.1. The temporal evolution of the population fractions for this simulation case is shown in Figure 7.3. Similar to the $\lambda_L = 1.064\,\mu\mathrm{m}$ simulation case, the charge state distribution undergoes considerable changes in the early expansion phase, and then stops evolving in the far expansion zone. However, for the $\lambda_L = 10.6\,\mu\mathrm{m}$ simulation case, the plasma is retaining higher charge state ions, in this case up to Sn^{+4} ions; which agrees qualitatively with the experimental measurements in Chapter 5. As before, if the term in the electron energy equation representing the excess energy of three-body recombination is set to zero, the plasma will recombine completely in the simulation.

To provide additional insight into the simulation results, the electron-ion collision frequency, ν_{ei}, as a function of time is plotted in Figure 7.4 for each simulation case. A derivation of ν_{ei} can be found, e.g., in Chen [117], and is given in cgs units by

$$\nu_{ei} = \frac{\pi\, n_e\, e^4}{m_e^{1/2}\, T_e^{3/2}} \ln\Lambda \quad \left[\mathrm{s}^{-1}\right], \tag{7.23}$$

where $e = 4.80 \times 10^{-10}$ statcoulomb and $m_e = 9.11 \times 10^{-28}\,\mathrm{g}$. As discussed previously in Chapter 6, ν_{ei} is a constant in an adiabatic expansion, but will decay with time in a non-adiabatic expansion. This transition between the two general types of expansion can be seen for the $\lambda_L = 10.6\,\mu\text{m}$ simulation case (in Figure 7.4b), where ν_{ei} is approximately constant in the earliest phase of expansion before subsequently decaying. This implies the early phase of expansion is approximately adiabatic, and the excess energy of three-body recombination is not yet an important mechanism. In the more dense plasma (the $\lambda_L = 1.064\,\mu\text{m}$ simulation case), ν_{ei} is decaying throughout the entire simulation, implying the expansion is always non-adiabatic. In this simulation case, recombination is enhanced due to the high initial density, and the excess energy of three-body recombination is an important mechanism for the entire simulation as it depends directly on the recombination rate. Finally, a comparison of Figures 7.4a and 7.4b show that ν_{ei} is higher for the simulation at the shorter laser wavelength, as expected in the more dense plasma.

The decay of ion and electron temperatures in both simulations cases is plotted in Figure 7.5. For the $\lambda_L = 10.6\,\mu\text{m}$ case, T_e initially decays with time as t^{-2} before subsequently transitioning to a t^{-1} decay, which is consistent with the previous result that ν_{ei} is approximately constant only in the early expansion phase. For the $\lambda_L = 1.064\,\mu\text{m}$ case, T_e is decaying with time approximately as t^{-1} throughout the entire expansion, which is also consistent with the previous simulation result for the decay of ν_{ei} in this case. In each simulation case, the ion temperature deviates from the electron temperature only in the far expansion zone, which occurs when the simulation time becomes comparable to the electron-ion thermalization time. After this deviation occurs, the electron temperature will always exceed the ion temperature, because the excess energy of three-body recombination is a source term in the electron energy equation. By the time electron and ion temperatures begin to deviate, most of the changes in the charge state distribution have already taken place, which implies that separation of ions and electrons in the expanding plasma will be a negligible effect.

7.3.4 Deficiencies of the 0D model

Although the 0D model was able to reproduce some of the features observed in the experiments discussed in Chapter 5, and provide insight into the physics of ion expansion, many deficiencies are necessarily present in a simple, zero-dimensional model.

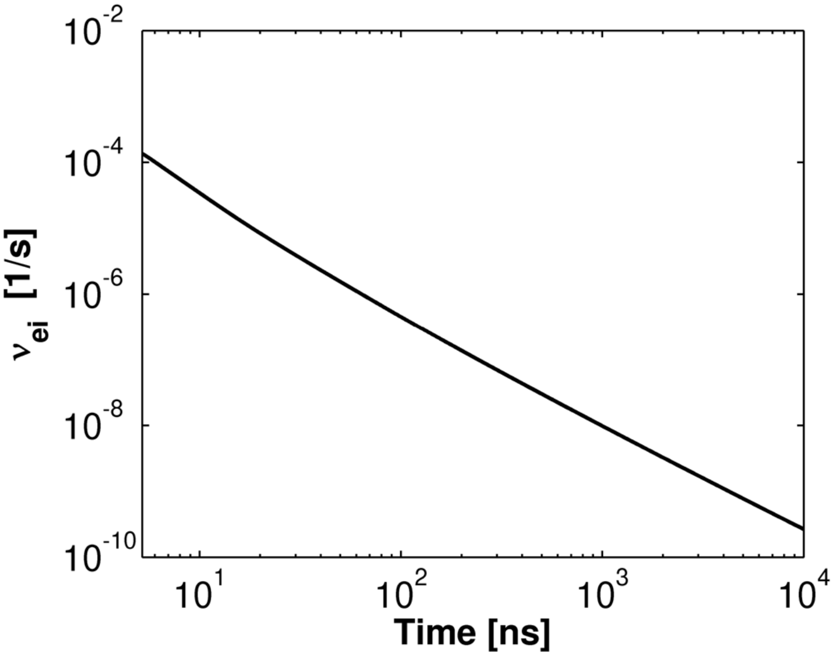

(a) Decay of ν_{ei} for the $\lambda_L = 1.064\,\mu\text{m}$ case.

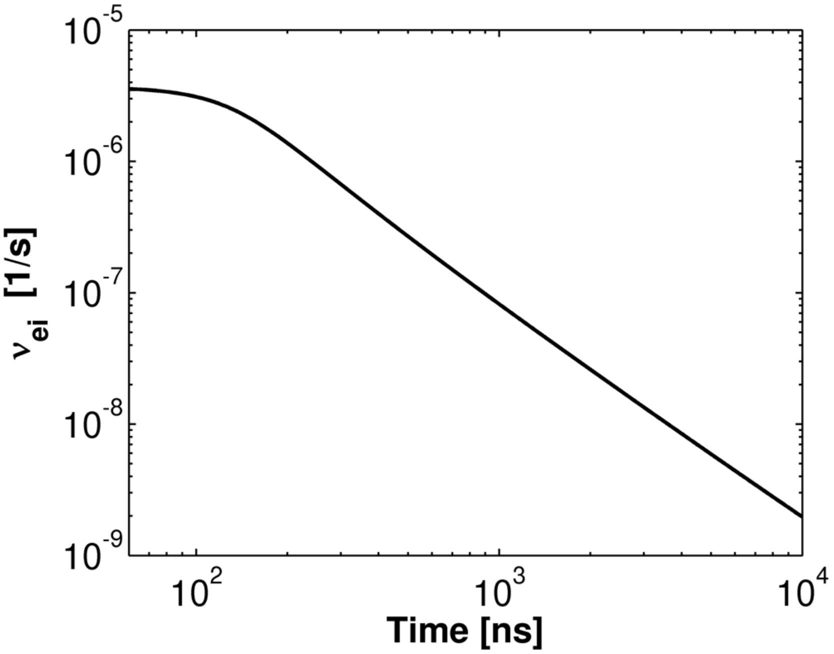

(b) Decay of ν_{ei} for the $\lambda_L = 10.6\,\mu\text{m}$ case.

Figure 7.4: Decay of electron-ion collision frequency, ν_{ei}, as a function of time for both simulation cases.

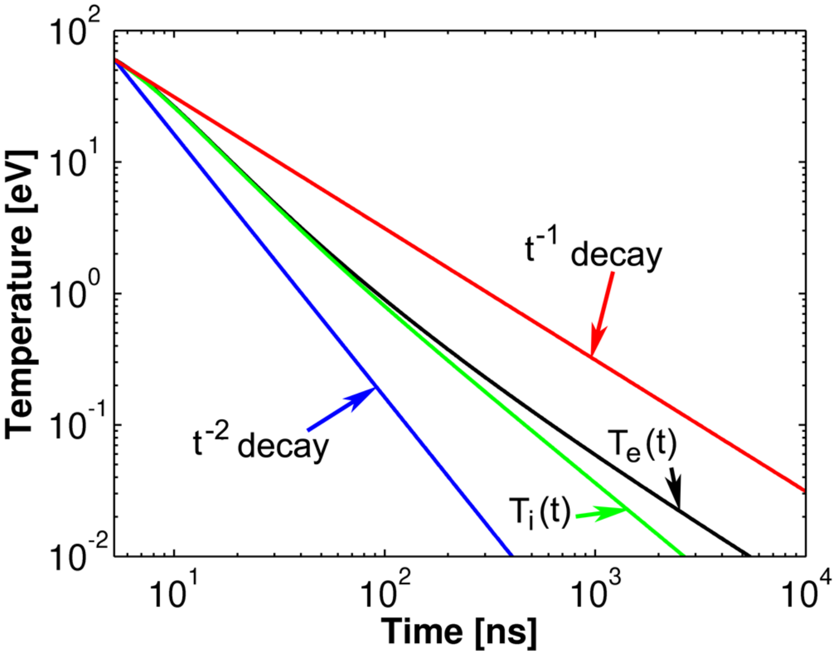

(a) Decay of T_e and T_i for the $\lambda_L = 1.064\,\mu\mathrm{m}$ case.

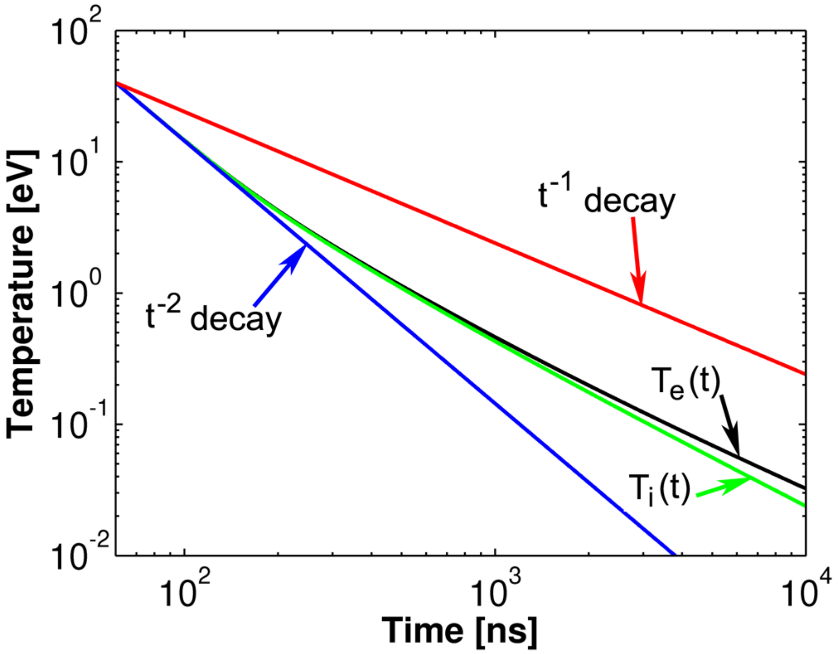

(b) Decay of T_e and T_i for the $\lambda_L = 10.6\,\mu\mathrm{m}$ case.

Figure 7.5: Decay of electron temperature, T_e, and ion temperature, T_i, as a function of time for both simulation cases.

A significant assumption is that the plasma has homogeneous properties, and expands spherically for all time. In the laboratory, however, gradients in both temperature and density will be present [21] [118], and for spatial scales on the order of the laser focal diameter two-dimensional expansion profiles can be measured [22] [42]. In addition, the 0D model does not include any spatial separation of the different components of the plasma, i.e., all electrons are available to recombine with all ions for all time. This is one possible reason why the charge states simulated in the far expansion zone were lower than those measured in the experiments in Chapter 5. In addition, the rates for the various atomic processes considered, in addition to the calculation of the excess energy of three-body recombination, are all approximations themselves. The absence of photo-ionization from the atomic processes considered also introduces error in the model, especially in light of the fact that reabsorption of EUV light is known to occur in laser-produced Sn plasma [18] [22]. Finally, the initial conditions for the 0D simulations were assumed from physics-based considerations, and were not taken from either experiment, or from another code simulating the plasma during the laser pulse. All of these approximations introduce error in the 0D model, and for this reason the model was unable to quantitatively replicate the previous experimental measurements. Nevertheless, the 0D model is able to reproduce some of the qualitative aspects of the previous experiments, and the model provides a convincing understanding of how the initial plasma conditions such as density and temperature affect the recombination rate and ion properties throughout the entire expansion.

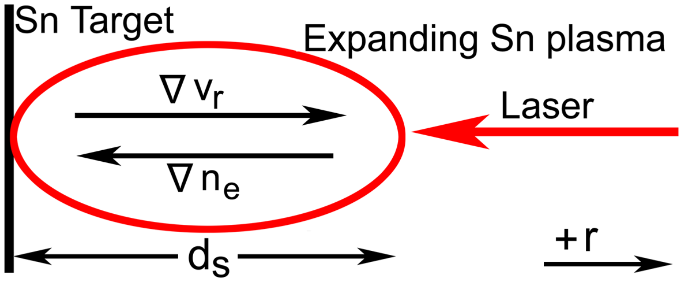

Figure 7.6: One-dimensional simulation geometry at $t = t_0$.

7.4 One-dimensional Simulations of Ion Expansion into Vacuum

The zero-dimensional simulations discussed in the previous section are inherently unable to model the spatial separation of different charge states within an expanding plasma. As measured in Chapter 5, however, higher charge state ions have higher velocities, implying that spatial separation is an important feature in the expansion of laser-produced Sn plasma. In addition, ion energy distributions cannot be simulated within a 0D model, and thus direct comparisons with the measurements of ion energy distributions discussed previously cannot be made. For these reasons, a more complex, one-dimensional model of ion expansion into vacuum is described in this section. The spatial expansion is driven by the plasma pressure gradient, and modeled in a Lagrangian grid that expands several orders of magnitude throughout the simulation.

7.4.1 Simulation Geometery and Initial Conditions

The initial conditions for the 1D simulations are assumed at a time t_0 when the laser heating is negligible, to avoid complexities associated with modeling the plasma dynamics during the laser pulse. At $t = t_0$, the situation described graphically in Figure 7.6 is assumed to exist. The interaction of a high intensity laser and a Sn target generates a spherically expanding plasma with spatial scale on the order of the laser focal diameter, d_S. The speed gradient, ∇v_r, points away from the target, and the electron density gradient, ∇n_e, points towards the target. Accordingly, atoms with high kinetic energy are initially in a region of low electron density, where the recombination rate (depending on n_e) is comparatively low. The opposite is true for atoms close to the target surface, i.e., they are in a region with a comparatively high recombination rate. Thus, the model assumed here will result in higher energy ions retaining the highest ionization states, without considering any electric field. This *recombination model* of ion acceleration has been applied in a similar approach by other authors to simulate the expansion of C and Al plasma [104] [119], and will be compared in a subsequent section with the electrostatic model of ion acceleration described previously in Section 5.1.2.

The initial spatial profile of electron density is modeled as an exponential decay with scale length l_S, as given by

$$n_e\left(r, t = t_0\right) = n_{e,0} \exp\left(-r/l_S\right), \tag{7.24}$$

where $n_{e,0}$ is the peak initial electron density, and r is the radial spatial coordinate in the 1D model, increasing away from the target. Indeed, interferometric measurements close to the target surface confirm that an exponential decay can be fit to the actual density profile [42] [113]. The initial speed distribution is assumed to have a linear profile [93] [120], given by

$$v_r\left(r, t = t_0\right) = 3\, c_{S,0}\left(\frac{r}{r_0}\right), \tag{7.25}$$

where r_0 is the initial plasma radius, and the factor of 3 is equal to $\frac{2}{\gamma-1}$, where $\gamma = \frac{5}{3}$ is the ratio of specific heats for a plasma. The expression for the initial plasma sound speed, $c_{S,0}$, was defined previously in Equation (7.10). As in the 0D simulations, the initial spatial profile of electron temperature is assumed constant throughout the domain due to high thermal conductivity during the laser pulse, i.e., $T_e\left(r, t = t_0\right) = T_{e,0}$. The initial spatial profile of ion temperature is identical to the electron temperature profile at $t = t_0$, as the initial electron-ion thermalization time will be small compared to t_0. As in the 0D simulations, electron and ion temperatures can deviate at later times, and are coupled through a temperature relaxation term in the energy equation.

The initial distribution of atoms (ion and neutrals) and electrons in the 1D Lagrangian grid with N cells is assigned in the following procedure. The average ionization state at $r = 0$ is $\bar{Z}_0$, and is calculated using the CR model from the initial electron temperature and density. The peak heavy atom density is then $n_{H,0} = n_{e,0}/\bar{Z}_0$, and the initial spatial profile of atom density, $n_H\left(r, t = t_0\right)$, is also assumed to be an exponential decay with gradient scale length l_S. The total number of heavy atoms, $N_{H,\text{total}}$, contained within the simulation domain ($0 \leq r \leq r_0$) is obtained by integrating $n_H(r)$ over the entire domain, i.e.,

$$N_{H,\text{total}} = \int_0^{r_0} 4\pi r^2 n_{H,0} \exp(-r/l_S)\, dr, \tag{7.26}$$

where spherical expansion is assumed. Each cell in the 1D Lagrangian grid will contain an identical number of atoms, so that the number of heavy atoms per cell, N_C, will be given by $N_C = N_{H,\text{total}}/N$. The radius of the first Lagrangian cell, r_1, must therefore satisfy

$$N_C = \int_0^{r_1} 4\pi r^2 n_{H,0} \exp(-r/l_S)\, dr, \tag{7.27}$$

resulting in an implicit equation for r_1 which can be solved numerically. The radius of the second Lagrangian cell, r_2, must satisfy

$$N_C = \int_{r_1}^{r_2} 4\pi r^2 n_{H,0} \exp(-r/l_S)\, dr, \tag{7.28}$$

which results in an implicit equation for r_2. Proceeding in this manner, all of the Lagrangian radii at $t = t_0$ can be calculated, so that each cell contains the same number of atoms.

After the Lagrangian radii have been calculated, the speed of each cell boundary can be calculated from Equation (7.25). Only radius and speed are defined at the cell boundaries; all other quantities are assumed to be homogeneous within each cell, as shown in Figure 7.7. The quantities computed within the j^{th} cell, at the k^{th} time step, include the average ionization state $\bar{Z}\big|_j^k$, plasma pressure $p\big|_j^k$, mass density $\rho\big|_j^k$, electron temperature $T_e\big|_j^k$, ion temperature $T_i\big|_j^k$, number of electrons $N_e\big|_j^k$, and the number of m-times ionized atoms $N_m\big|_j^k$ for $0 \leq m \leq Z$, where Z is the highest ionization state.

The initial atom density within each cell can be computed from the total number of atoms for each cell (a constant), and the inner and outer Lagrangian radii, which are used to calculate the cell volume. At this point, the CR model can be used to calculate the distribution of ionization states within each cell from the local atom density and electron temperature, as discussed in Section 7.2. This step in the algorithm to initialize the 1D simulations requires most of the computation time. From the initial charge state distribution, the initial average ionization state can be calculated, and through the plasma

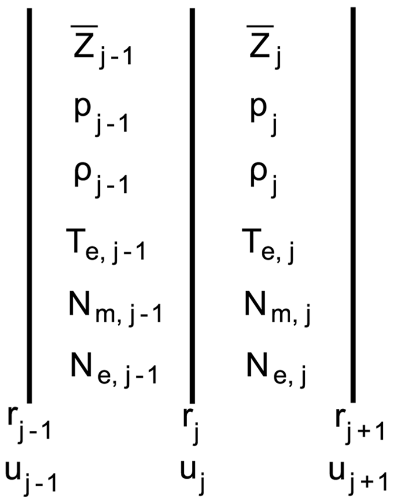

Figure 7.7: Lagrangian grid used in the 1D simulations at the time step k.

neutrality condition, the initial number of electrons within each cell can be calculated. Equation (6.3) is then used to calculate the plasma pressure within each cell, and the initial mass density within each cell is calculated as

$$\rho_j = \frac{1}{V_j}\left(M_i N_C + m_e N_{e,\,j}\right), \tag{7.29}$$

where m_e is the electron mass and V_j is the j^{th} cell volume. At this point, the algorithm to assign all necessary initial values for the 1D Lagrangian grid shown in Figure 7.7 has been described, and the simulation can proceed.

7.4.2 Lagrangian Hydrodynamics Solver

Throughout the simulation, each cell in the Lagrangian grid retains its unique identity assigned at $t = t_0$, which in this case is a constant number of atoms. Accordingly, mass is not transported across cell boundaries in the Lagrangian simulation. To account for this, cell radii in the Lagrangian grid must always be expanding, and in addition, the speed of each cell boundary must be always be increasing. The calculations to update the radius and speed of each cell boundary at each time step are carried out in the hydrodynamics (HD) solver.

Expansion of the Lagrangian grid is driven by the plasma pressure gradient computed at each cell boundary, i.e.,

$$\left(\left. \frac{du}{dt} \right|_{j}^{k} \right) = -\frac{1}{\left. \rho \right|_{j}^{k}} \left(\left. \frac{dp}{dr} \right|_{j}^{k} \right). \tag{7.30}$$

The pressure gradient calculated at the cell boundaries is a function of the midpoint radii, and the pressure within surrounding cells, as given by

$$\left(\left. \frac{dp}{dr} \right|_{j}^{k} \right) = \frac{\left. p \right|_{j+\frac{1}{2}}^{k} - \left. p \right|_{j-\frac{1}{2}}^{k}}{\left. r \right|_{j+\frac{1}{2}}^{k} - \left. r \right|_{j-\frac{1}{2}}^{k}}, \tag{7.31}$$

where the midpoint radius is

$$\left. r \right|_{j+\frac{1}{2}}^{k} = \frac{\left. r \right|_{j+1}^{k} - \left. r \right|_{j}^{k}}{2}, \tag{7.32}$$

and $\left. p \right|_{j+\frac{1}{2}}^{k}$ is the pressure within each cell (defined in Figure 7.7 as just $\left. p \right|_{j}^{k}$ for simplicity). The mass density must also be calculated at the cell boundaries, and the average of adjacent values within cells is used.

The time step for stability is calculated by ensuring the Courant condition is met, i.e., that disturbances do not move fast enough to cross cell boundaries. Local disturbances move at the local speed of sound, given by

$$\left. c_S \right|_{j}^{k} = \sqrt{\frac{\left. \bar{Z} \right|_{j}^{k} \left. T_e \right|_{j}^{k}}{M_i}}. \tag{7.33}$$

The time step will then be given by

$$\left. \Delta t \right|_{j}^{k} \leq \frac{\left. r \right|_{j+1}^{k} - \left. r \right|_{j}^{k}}{\left(\left. u \right|_{j+1}^{k} - \left. u \right|_{j}^{k} \right) + \left. c_S \right|_{j}^{k}}, \tag{7.34}$$

where the speeds of adjacent cell walls, which can be on the order of the sound speed, have been taken into account. A unique time step for each cell is calculated in this procedure, and the minimum of all calculated time steps must be used. For later times in the simulation, the time step is further reduced, so that between any subsequent time steps the maximum Δr for all cells is no greater than 1 cm. This is necessary, because in the post-simulation analysis various quantities along the path of expansion are calculated, and spatial resolution better than 1 cm is desired. Finally, the evolution of the various hydrodynamic quantities can be plotted in the post-simulation analysis to ensure the calculations for all quantities were indeed stable.

The radius and speed of each cell boundary are updated in time by a method with second-order accuracy known as the Leapfrog method. In this numerical procedure, the radius and speed at each cell boundary leap over each other in time at half integer time steps, i.e.,

$$u\Big|_j^{k+1/2} = u\Big|_j^{k-1/2} + \left(\frac{du}{dt}\Big|_j^k \right) \Delta t\Big|_j^k , \tag{7.35}$$

$$r\Big|_j^{k+1} = r\Big|_j^k + \left(u\Big|_j^{k+1/2} \right) \Delta t\Big|_j^k . \tag{7.36}$$

The Leapfrog method has the advantages of second-order accuracy and the simplicity of an explicit method. As will be shown subsequently in the simulation results section, the 1D simulations are capable of reproducing the experimental data only qualitatively, due to the imprecise assumption of initial conditions and the various other assumptions in the code. In light of this, second-order accuracy for the HD solver is sufficient.

7.4.3 Rate Equation Solver

After the initial conditions have been assigned, as described in Section 7.4.1, and the HD solver has updated the speed and radii at cell boundaries and defined a hydrodynamic time step, as described in Section 7.4.2, a system of nonlinear ODEs is integrated to update all other quantities within each cell for the duration of the time step. Specifically, the ODE set contains rate equations for the evolution of each ion species, in addition to energy equations for both electrons and ions, which is the same system solved for the 0D simulations described in Section 7.3, but with a few important modifications. The ODEs must be integrated within each cell and at every time hydrodynamic time step. In the 1D simulations, a minimum of 10^2 cells are used, and the simulations require on the order of 10^3 time steps, therefore for every 1D simulation, the 0D simulation is repeated on the order of 10^5 times. The temporal limits of integration for the first time step, which are the same for all cells, are from t_0 to $t_0 + \Delta t\Big|^{k=1}$. For any subsequent time step, the system of ODEs must be integrated from a time t_1 to t_2, where

$$\begin{aligned} t_1 &= t_0 + \sum_{k=1}^{N_T} \Delta t \Big|^{k} , \\ t_2 &= t_0 + \sum_{k=1}^{N_T+1} \Delta t \Big|^{k} , \end{aligned} \tag{7.37}$$

and N_T represents the number of elapsed time steps ($N_T = 0$ for the first time step). The system of rate equations for the evolution of each ion species can be applied in the same formulation used for the 0D simulations [(Equations (7.11), (7.12), (7.13), and (7.14)]. The ODEs representing the electron and ion energy equations must be modified slightly for application in the 1D simulations. The modified electron energy equation is

$$\frac{dT_e}{dt} = -2T_e \frac{dr/dt}{r} - \frac{2}{3} \frac{Q}{1+\bar{Z}} + \frac{T_i - T_e}{\tau_{ei}} , \tag{7.38}$$

and the modified ion energy equation is

$$\frac{dT_i}{dt} = -2T_i \frac{dr/dt}{r} + \frac{T_e - T_i}{\tau_{ei}} . \tag{7.39}$$

7.4.4 Algorithm and Details of the Calculation

The algorithm for a single time step in the 1D simulations is described graphically in Figure 7.8. The quantities in (1) and (2) in the figure, at the k^{th} time step, represent either the initial conditions, as described in Section 7.4.1, or the output from a previous time step. The code first updates radii and speed for all cell boundaries, and computes the time step in the HD solver, as described in Section 7.4.2. The rate equation solver is then applied within each cell, as described in Section 7.4.3. The inputs to the rate equation solver include the cell radius at adjacent time steps [in (1) and (3) in the figure], in addition to the quantities in (2) at the k^{th} time step. The rate equation solver updates the number of each ion species, number of electrons, and electron temperature within each cell to obtain the quantities in (4) at the $k+1$ time step. From these calculations, the average ion charge state at the $k+1$ time step is calculated. Finally, from the output of the HD solver and the updated average ion charge state, values for pressure and mass density at the $k+1$ time step can be calculated [(6) in the figure].

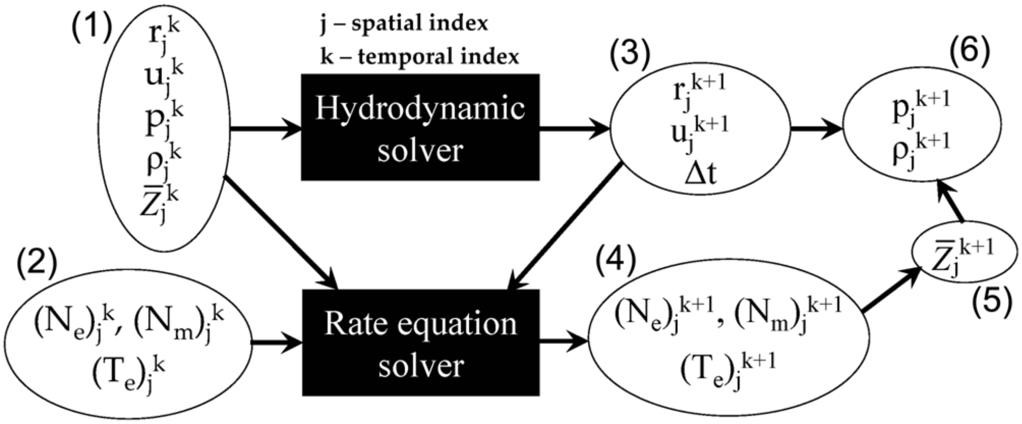

Figure 7.8: Algorithm to update variables in the 1D simulations for the k^{th} time step.

The lower limit on the number of cells required for the initial Lagrangian grid is set by stability in the simulation output. For example, the expansion of a C plasma was simulated as the initial number of cells was varied from 100 to 300, as shown in Figure 7.9. Clearly, for the initial conditions of this simulation, more than 300 cells are required for stability in the output. In general, as the scale length assumed for the initial exponential decay of density is reduced, variations in plasma properties occur over shorter spatial intervals, and more cells will be required in the Lagrangian grid.

Simulations were carried out in the MATLAB environment, again utilizing the built-in ODE solver *ode15s* [116]. The simulation time varied with the number of Lagrangian cells and number of ion species included in the simulation. For example, simulations were carried out to model the expansion of C plasma, in order to reproduce numerical results from a similar code by Kunz [104]; the numerical results in Figure 7.9 are an example. These simulations for C plasma ($Z = 6$) typically require no longer than an hour of computation time, depending on the number of Lagrangian cells. The computation time increases when the code is applied to higher Z plasma. In the case of Sn plasma, where the atomic number is 50, the requisite number of ion species to include in the code is determined by looking for the ionization state at which population fractions calculated in the CR model become negligible. For a Sn plasma at a temperature and density relevant to the EUV x-ray source application, approximately 23 ionization states must be included in the code. For these simulations, approximately 2 to 5 hours of computation time is required, depending on the number of Lagrangian cells, and on the distance up to which the domain is assigned to expand before stopping the simulation. A typical value for the initial radius of the simulation domain is 100 μm, and the 1D code can model the plasma dynamics over distances of tens of cm.

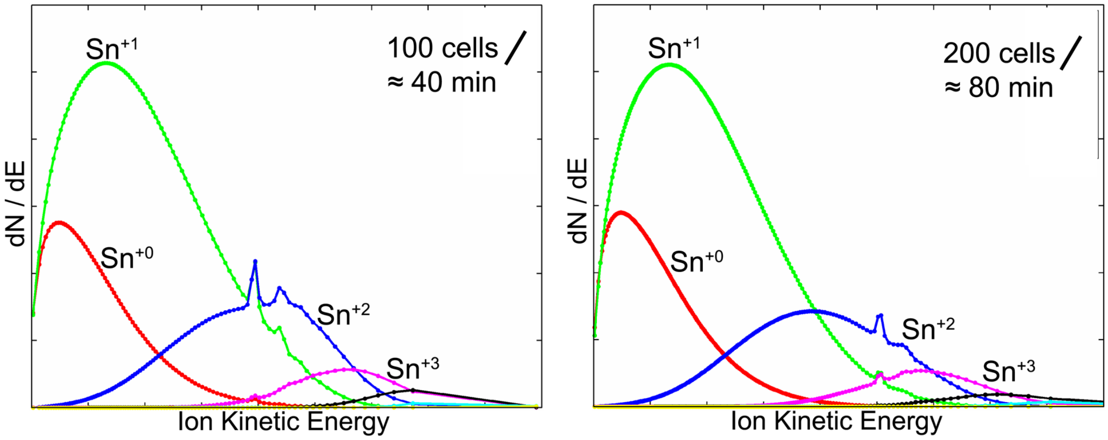

(a) Simulation with $N = 100$ cells (b) Simulation with $N = 200$ cells

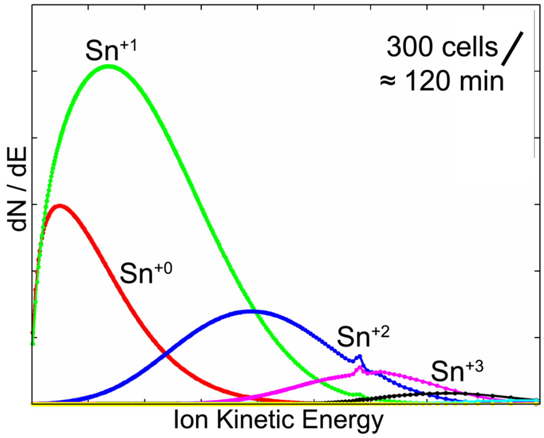

(c) Simulation with $N = 300$ cells

Figure 7.9: Simulations of the ion energy distribution in the far expansion zone of expanding C plasma. The number of cells included in the initial Lagrangian grid clearly has an effect on stability, in addition to the requisite computation time. For the initial conditions of these simulations, more than 300 cells are required for stability. As the scale length for the initial exponential decay of density is increased, fewer cells will be required for a stable simulation.

7.4.5 Simulation Results

Two primary cases were modeled in the 1D simulations, corresponding to Sn plasma produced by both 1.064 µm and 10.6 µm lasers. The same initial conditions used in the 0D simulations and summarized in Table 7.1, are also used as initial conditions for the 1D simulations, but with a few differences. In the 1D simulations, each cell is characterized by the unique properties described in Figure 7.7, whereas in the 0D simulations, homogeneous properties throughout the domain are assumed. The density and temperature given in Table 7.1 at both laser wavelengths therefore represent the peak initial values in the 1D simulations. Only the peak initial density and temperature varied between the two simulation cases; all other initial conditions were kept constant. For both simulation cases, the initial plasma radius is $r_0 = 100\,\mu\mathrm{m}$, and the initial density gradient scale length is $l_S = 20\,\mu\mathrm{m}$. For both simulation cases, 200 Lagrangian cells are sufficient for a stable output, and approximately 4 hours of computation time are required to allow the first Lagrangian radius to expand to a distance of 20 cm.

The simulation results are described primarily through plots of the charge-state resolved energy distribution, as recorded by simulated detectors at various distances from the laser plasma source. These calculations require interpolation of the simulated data across cell boundaries, as all the Lagrangian radii can never exactly equal the desired detector distance. For example, the calculated radii for 3 adjacent cells over 4 subsequent time steps are given in Table 7.2. For each cell, a unique time step at which the cell radius first exceeds the detector distance can be located. If the simulated detector distance is 5 cm, then in the example, the radius of the 7th cell exceeds the detector distance at the 238th time step, and by an amount 32% greater than the interval in radius between the 238th and previous time step. Accordingly, all other values of interest must be interpolated by the same amount, and this algorithm must be repeated for all cells, and for each nominal detector distance.

The ion energy distribution for the $\lambda_L = 1.064\,\mu\mathrm{m}$ simulation case in the far expansion zone is shown in Figure 7.10, and can be compared to the experimental measurement using the Nd:YAG laser shown in Figure 5.2a. In both experiment and simulation, higher charge state ions have higher energies, and all ion energies greatly exceed the initial thermal electron temperature. The exact simulated values for dN/dE, in addition to

Table 7.2: Calculated Lagrangian radii for 3 adjacent cells over 4 subsequent time steps.

Time Step Index	7^{th} Cell Radius [cm]	8^{th} Cell Radius [cm]	9^{th} Cell Radius [cm]
235	4.48	4.70	4.91
236	4.67	4.90	5.11
237	4.87	5.11	5.33
238	5.06	5.30	5.53

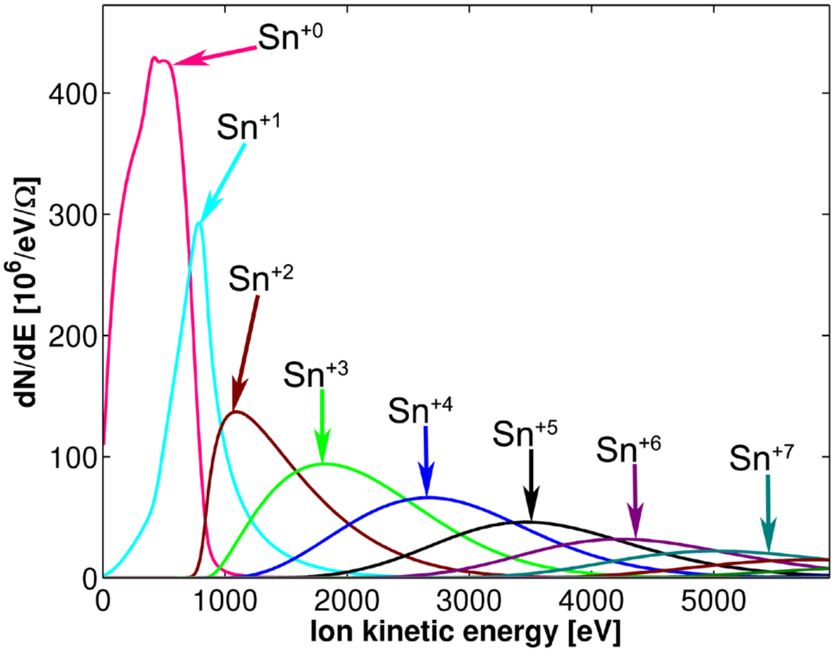

Figure 7.10: Ion energy distribution for the $\lambda_L = 1.064\,\mu$m simulation case, as recorded by a simulated detector 10 cm from the laser plasma source.

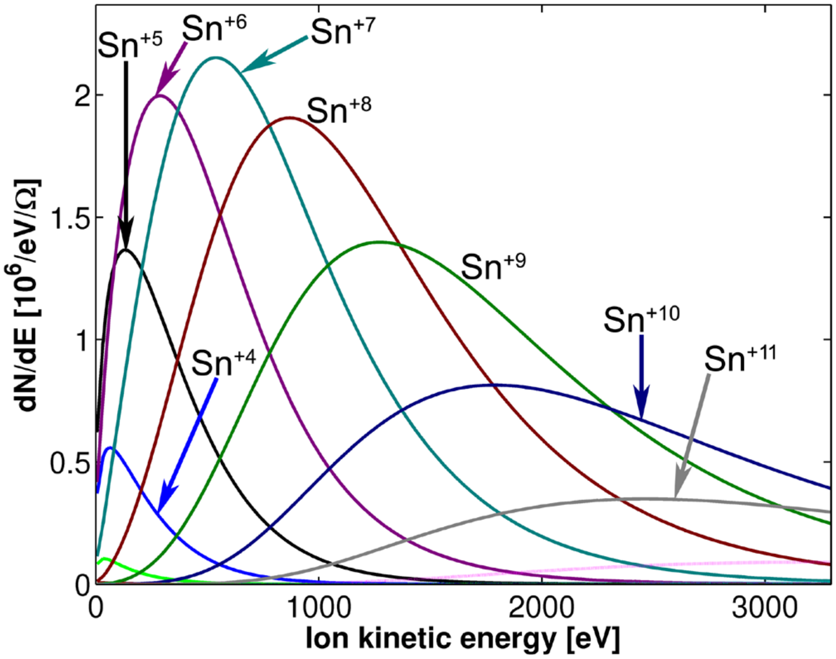

Figure 7.11: Ion energy distribution for the $\lambda_L = 10.6\,\mu\text{m}$ simulation case, as recorded by a simulated detector 10 cm from the laser plasma source.

the relative relationship in dN/dE between the different ionization states, do not agree between experiment and simulation. Specific reasons the code is only reproducing qualitative aspects of the experiments are discussed subsequently. The simulated ion energy distribution in the far expansion zone for the $\lambda_L = 10.6\,\mu\text{m}$ simulation case is shown in Figure 7.11, and can be compared to the experimental measurement using the CO_2 laser shown in Figure 5.2b. As before, the relations between charge state, ion energy, and initial thermal electron temperature all agree qualitatively with the experimental results. In addition, higher charge state ions are present in the simulation at the longer laser wavelength, which agrees with the observed dependence of average ionization state on laser wavelength from the experiments (c.f. Section 5.1.1).

In addition to the simulation of ion properties in the far expansion zone, the 1D code can simulate ion properties over a range of distances along the path of plasma expansion. This is an extension of the experiments, where the ion energy distribution had to be measured 100 cm from the laser plasma source due to diagnostic limitations. The minimum distance at which ion properties can be simulated must be greater than the outer radius of the domain at the first time step, so that each Lagrangian cell expands past the simulated detector at a subsequent time step. Due to this limitation, the significant changes to the ion energy distribution occurring within the initial plasma volume cannot be resolved even in the simulation. In Figure 7.12, the simulated spatial evolution of the ion energy distribution for the $\lambda_L = 1.064\,\mu\text{m}$ simulation case is plotted, where each subfigure represents data at increasing distances from the laser plasma source, commencing at 200 µm. The same plot for the $\lambda_L = 10.6\,\mu\text{m}$ simulation case is shown in Figure 7.13.

As seen in Figure 7.12 representing the spatial evolution for the $\lambda_L = 1.064\,\mu\text{m}$ simulation case, most of the changes to the ion energy distribution are occurring within the first few mm of expansion. After 5 mm of expansion, no further evolution of the ion energy distribution can be noticed. In the case of Figure 7.13 representing the spatial evolution for the $\lambda_L = 10.6\,\mu\text{m}$ simulation case, the population of 6-times ionized Sn atoms is noticeably increasing as the simulated detector is scanned from 1 to 10 cm, in addition to other subtle changes over this distance. In both simulation cases, the initial charge state distribution, as determined by the collisional-radiative steady state model, has evolved significantly before it is first recorded by a simulated detector at 200 µm.

For each simulated detector distance, a total amount of charge contained within the plasma can be calculated. The spatial evolution of this quantity for each simulation case can be compared with the experimental results described in Section 5.2, where the distance over which the charge state distribution is evolving was measured. It was found in this previous experimental section that at the longer laser wavelength, the charge state distribution was evolving over longer distances. Figure 7.14 represents the total charge contained in the plasma as recorded by a simulated detector at various distances from the laser plasma source for both simulation cases. The data is plotted up to 1 cm in subfigures 7.14a and 7.14c, and up to 10cm in subfigures 7.14b and 7.14d. The total charge contained within the plasma is seen to evolve over a longer distance for the $\lambda_L = 10.6\,\mu\text{m}$ simulation case, although the differences in the two simulation cases are not as obvious as the differences in the same plot from the experimental measurements (c.f. Figure 5.7). Specific reasons for these simulation results are discussed in the subsequent section.

As demonstrated in Figures 7.10 to 7.14, the 1D code is reproducing the qual-

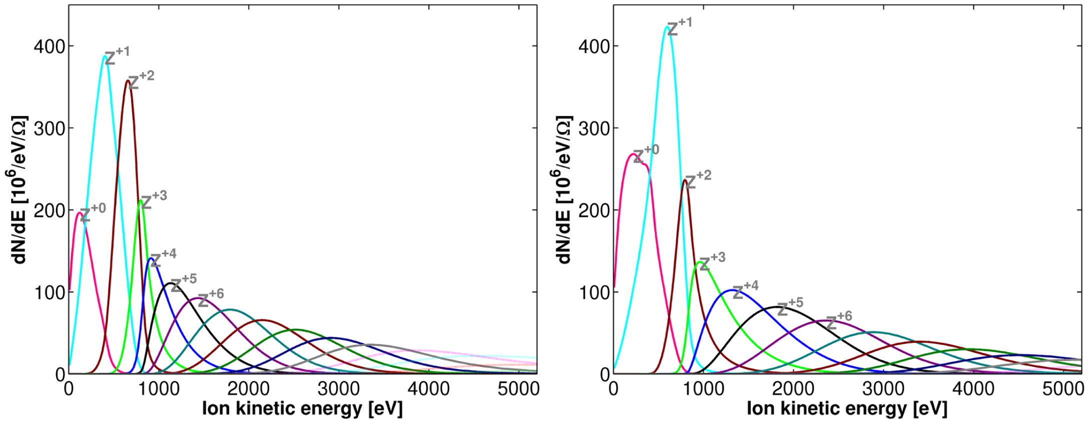

(a) $D = 0.02\,\mathrm{cm}$ (b) $D = 0.05\,\mathrm{cm}$

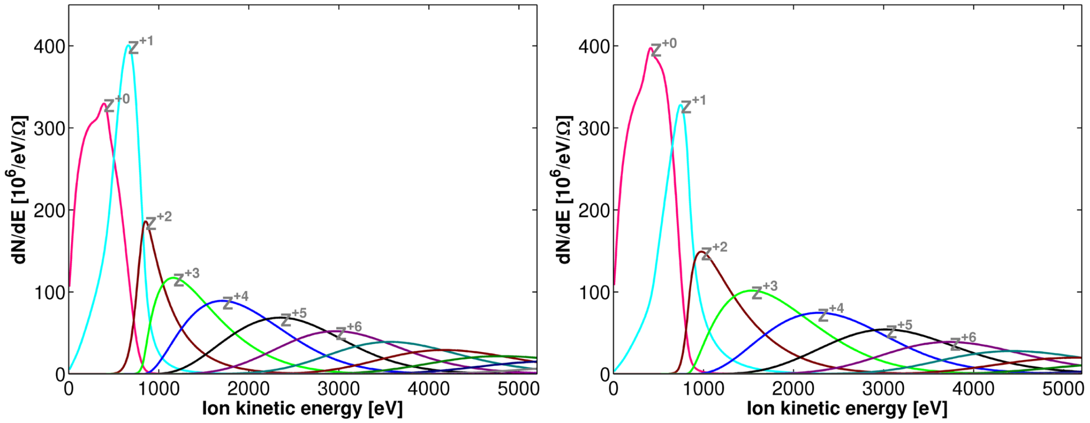

(c) $D = 0.10\,\mathrm{cm}$ (d) $D = 0.50\,\mathrm{cm}$

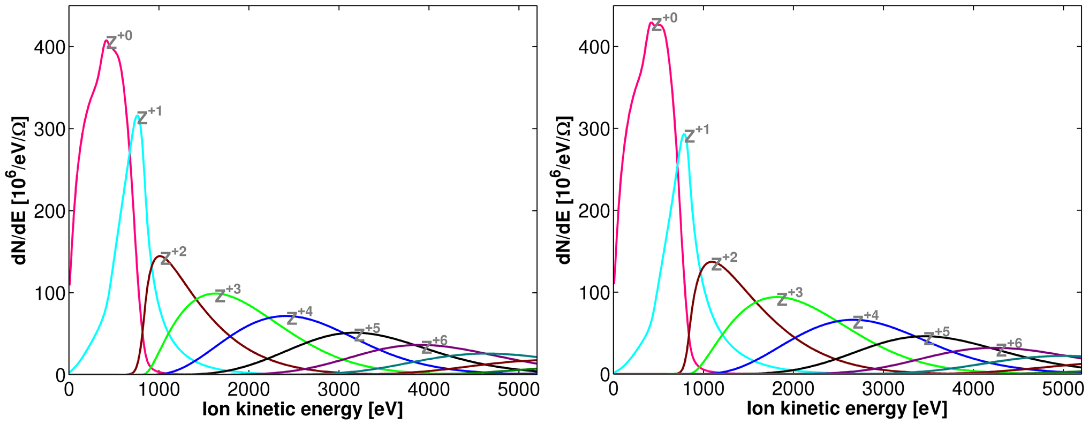

(e) $D = 1.00\,\mathrm{cm}$ (f) $D = 10.00\,\mathrm{cm}$

Figure 7.12: Evolution of the ion spectrum as recorded by a simulated detector at distances D along the path of plasma expansion, for the $\lambda_L = 1.064\,\mu\mathrm{m}$ simulation case.

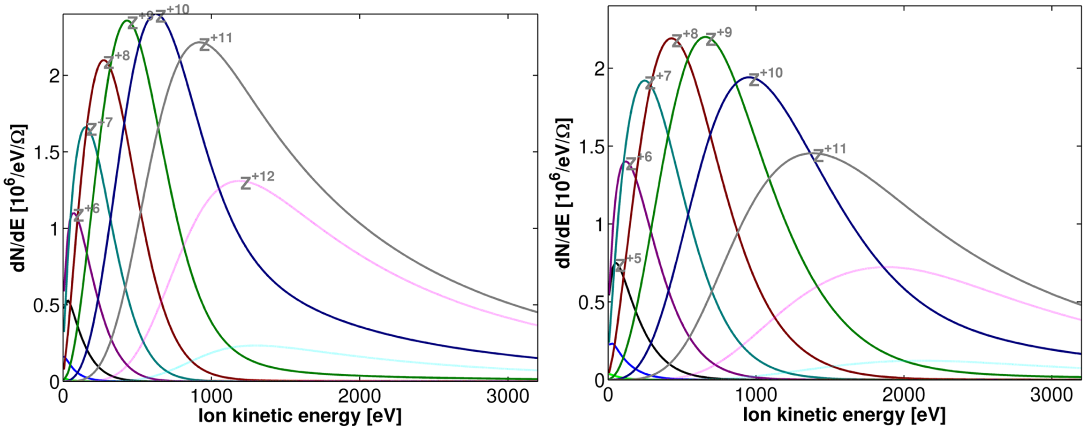

(a) $D = 0.02\,\mathrm{cm}$ (b) $D = 0.05\,\mathrm{cm}$

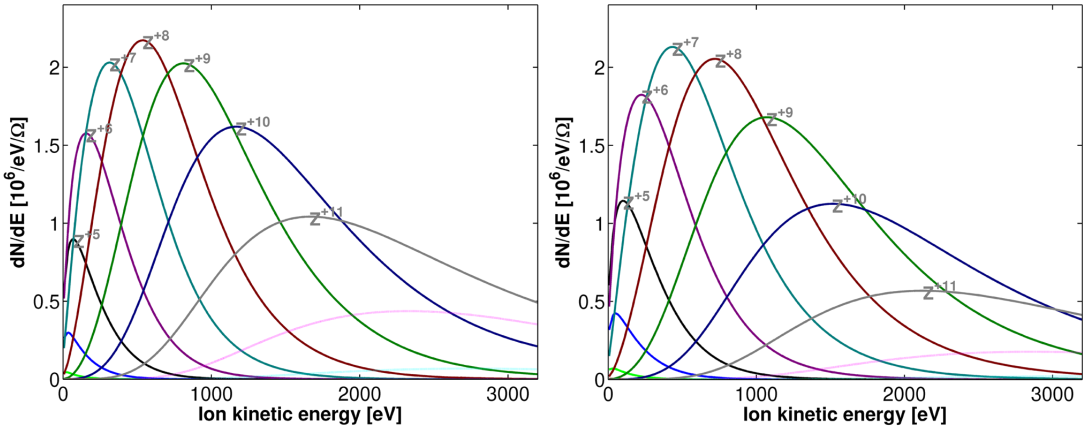

(c) $D = 0.10\,\mathrm{cm}$ (d) $D = 0.50\,\mathrm{cm}$

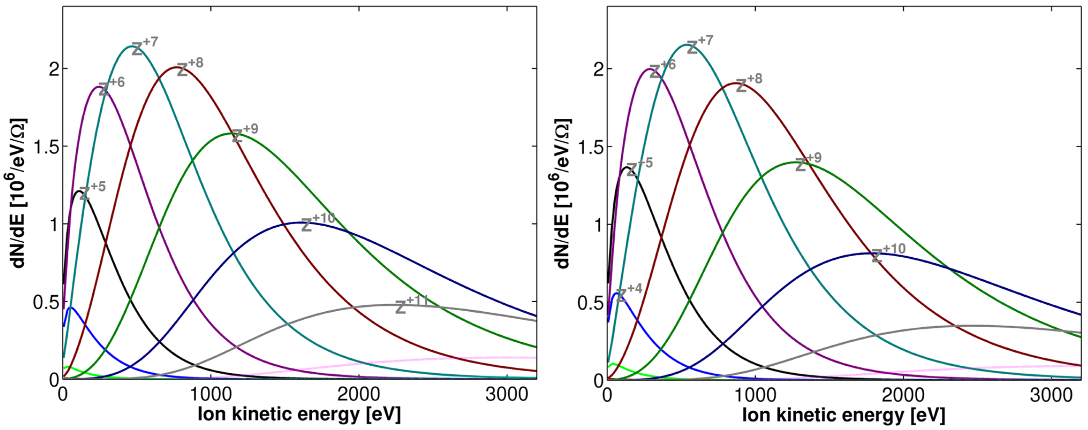

(e) $D = 1.00\,\mathrm{cm}$ (f) $D = 10.00\,\mathrm{cm}$

Figure 7.13: Evolution of the ion spectrum as recorded by a simulated detector at distances D along the path of plasma expansion, for the $\lambda_L = 10.6\,\mu\mathrm{m}$ simulation case.

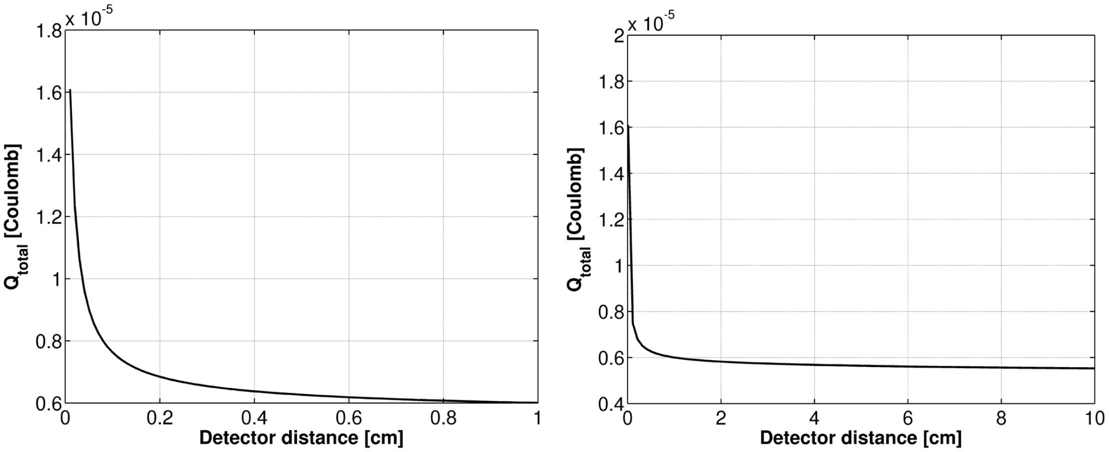

(a) $\lambda_L = 1.064\,\mu\mathrm{m}$ simulation case, $D \leq 1\,\mathrm{cm}$ (b) $\lambda_L = 1.064\,\mu\mathrm{m}$ simulation case, $D \leq 10\,\mathrm{cm}$

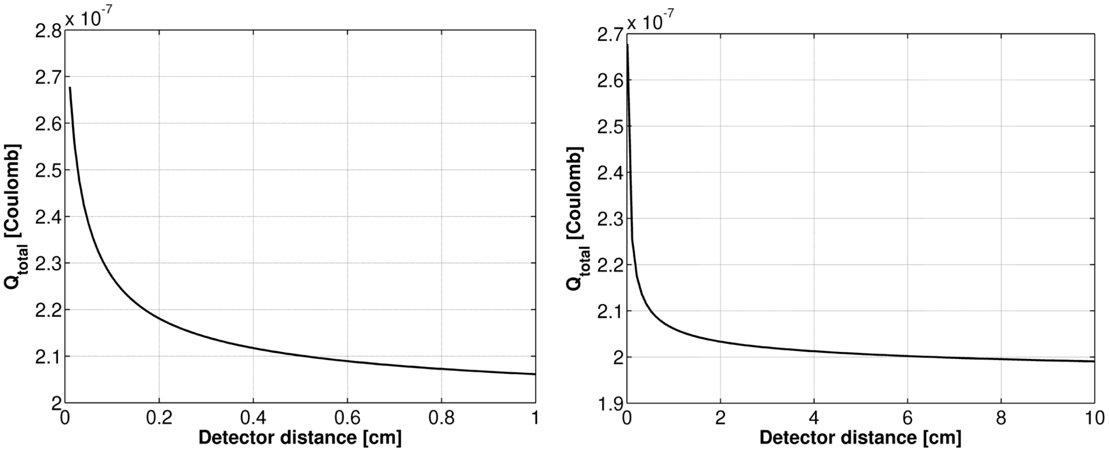

(c) $\lambda_L = 10.6\,\mu\mathrm{m}$ simulation case, $D \leq 1\,\mathrm{cm}$ (d) $\lambda_L = 10.6\,\mu\mathrm{m}$ simulation case, $D \leq 10\,\mathrm{cm}$

Figure 7.14: Simulation of the evolution of total charge contained in the plasma as recorded by a simulated detector at various distances, D, along the path of plasma expansion.

itative relationships observed in the experiments between ionization state, ion energy, laser wavelength, and the critical distance. Accordingly, the code can be used to predict qualitative relationships only between other quantities. Many of these have already been described in previous sections. For example, the transition in the decay of temperature with time from an adiabatic, t^{-2} decay to a nonadiabatic, t^{-1} decay can be demonstrated in the 1D model, but was previously demonstrated in Section 7.3.3 describing results of the 0D model. Additionally, the differences in the evolution of the electron-ion collision frequency for both simulation cases correspond with the previous results from the 0D model. The dependence of the simulated ion energy distributions in the far expansion zone on the initial plasma conditions is also as expected. As the initial electron temperature is reduced, the initial recombination rates increase [c.f. Equation (7.12) and (7.13)], and lower ionization states will be present after the ion energy distribution has stopped evolving; lowering the initial electron density has the same effect. The initial electron temperature also has a direct relationship to the simulated ion energies, as the initial sound speed $\left(\propto T_{e,0}^{1/2}\right)$ is used to set the initial speed distribution. Finally, when the excess energy of three-body recombination is set to zero in the simulations, the plasma will always recombine completely, which is the same behavior observed in the 0D simulations.

7.4.6 Deficiencies of the 1D model

The 1D model reproduced the results of the 0D model, and extended its capabilities by allowing for simulation of the ion energy distribution over a range of distances along the path of plasma expansion. The 1D model also reproduced many of the features observed in the experimental measurements, however its results are still qualitative only due to several deficiencies in the model. Specific features that do not agree quantitatively between experiment and simulation include the following.

- The relative relationships between the simulated values for dN/dE in the ion energy distribution for each ionization state do not agree in experiment and simulation.

- The lowest ionization states in the experimental measurements of the ion energy distribution had the highest values for dN/dE, which was not observed for the $\lambda_L = 10.6\,\mu\text{m}$ simulation case.

- The simulation result that higher ionization states have higher ion energies occurs only when the initial density gradient scale length is sufficiently short compared to the initial plasma radius.
- The differences in the spatial evolution of the charge state distribution at both laser wavelengths are much more subtle in the simulation as compared to the experiments.

As in the 0D simulations, the primary deficiency of the 1D simulations is that the initial conditions are assumed, rather than taken from experiment or transferred from another code simulating the plasma dynamics during the laser pulse. In addition, the outer radius of the initial domain is assumed to equal to the laser spot size, and the plasma initially outside of the domain is not included in the simulation. However, previous experiments and simulations have shown the profile of electron temperature at the peak of the laser pulse to include a steep gradient close to the target, a region of approximately isothermal conditions on the scale of the laser spot size, and then an exponential decay over several hundred μm [113] [121]. Those regions with a varying electron temperature, which are not included in the 1D code, certainly contribute to all of the observed quantitative discrepancies between experiment and simulation. The assumptions of a linear initial speed distribution, and an exponentially decaying initial density distribution, have all been verified through previous experiments and simulations [113] [121] [120], and should not contribute to the observed quantitative error as much as the assumption on the initial temperature profile.

The 1D code is inherently unable to model the effects of the near Gaussian intensity profile of the incident laser. At the periphery of the Gaussian spatial profile of the beam, plasma will be created at a much lower temperature, resulting in the production of ions with lower ionization states. The absence of these ions from the simulations is certainly a reason why Sn atoms with low ionization states were not observed in the $\lambda_L = 10.6\,\mu\text{m}$ simulation case. Plasma expansion in the focal plane is also inherently absent in a 1D model, which results in additional error. For Sn plasma relevant to the

EUV x-ray source application, previous experiments have demonstrated complex 2D expansion effects, including an anisotropic temperature profile [42]. As the three-body recombination rate is proportional to $T_e^{-9/2}$, any inaccuracies in the simulation of electron temperature has a profound effect on recombination throughout the expansion.

For both simulation cases, the initial density gradient scale length was 20 µm, and the initial plasma radius was 100 µm. As the former is increased, the initial plasma becomes increasingly homogeneous in density. As electron temperature is already assumed to be homogeneous in the initial plasma, the initial recombination rates will become increasingly homogeneous as the initial density gradient scale length is increased. Accordingly, the code will only predict the qualitative relationship that higher ionization states have higher ion energies when the initial density gradient scale length is sufficiently short compared to the initial plasma radius. This condition could be relaxed if the initial simulation domain is extended spatially. Indeed, experiments have shown that at the end of the laser pulse, the plasma has expanded by several times the initial laser spot size [42] [113] [121]. However, analytical expressions for density, temperature, and speed, as required in the assumption of initial conditions, are only valid on the scale of the laser spot size [88] [93] [120]. Applying results of a reliable 1D simulation during the laser pulse as the assumed initial conditions for the 1D code described here could mitigate this issue.

In addition, deficiencies present in the 0D simulations are also present in the 1D simulations. Specifically, the recombination and ionization rates, as well as the expression for the excess energy of three-body recombination, are all either derived under various assumptions, or fit to previous experimental data. Photoionization is also not included in the 1D model, even though reabsorption of EUV light is known to occur in Sn plasma relevant to the EUV x-ray source application [18] [22]. In light of all of these deficiencies, the 1D code is still a valuable simulation tool which enables a thorough understanding of the physical mechanisms responsible for the observed qualitative behavior of the plasma.

Chapter 7, in part, was previously reported in Journal of Applied Physics **107** 043303 (2010). The dissertation author was the primary investigator and author of this article. Contributing authors were Yezheng Tao, Mark Tillack, Sam Yuspeh, and Farrokh

Najmabadi of the Center for Energy Research at the University of California, San Diego. Nek M. Shaikh of the University of Sindh in Pakistan, and Eli Flaxer of the Tel-Aviv Academic College of Engineering in Israel also were contributing authors.

Chapter 8

Conclusions and recommendations for future studies

This work describes the application of radiation and particle plasma diagnostics, in addition to analytical and numerical analysis, to study ion emission and expansion in laser-produced Sn plasma. Lasers used for the relevant applications vary in wavelength and, accordingly, a primary focus of the present work is to determine the laser wavelength effects on ion properties throughout plasma expansion into vacuum. Chapter 1 summarizes some of the important processes occurring throughout the laser plasma interaction, and reviews the relevant applications. Chapter 2 describes the available experimental apparatus, including the Nd:YAG and CO_2 laser systems and beam diagnostics, the target chamber and ancillaries, and all available plasma diagnostics. Chapter 3 describes in significant detail the design and realization of the custom ion diagnostic utilized to record the species, energies, and charge states of ions in expanding plasma.

The scaling of mass ablation rate with laser intensity is measured for the case of a Nd:YAG LPP in Chapter 4. The experimental results are consistent with a model of steady-state planar ablation for low laser intensities which assumes nonlocalized laser absorption up to the critical density, and energy transport to the ablation front by diffusive conduction of thermal electrons [11] [67]. An obvious extension of this work is to repeat the experiments for a laser wavelength of 10.6 µm. The experiments, as conducted in Chapter 4, require the repetition of laser conditions as at least 10 different targets of varying thickness are positioned in the chamber, which in turn requires a laser source with repeatable beam properties over a timeframe of several days. This experimental method is not well-suited for application with the laboratory-built CO_2 laser source described in Section 2.2.2, due to several issues such as variations in gas properties and ambient laboratory conditions, which can cause significant variations in beam properties over a timeframe of several days. A better experimental method to measure the mass ablation rate for the case of a CO_2 LPP, obtaining the ablation rate in single laser pulse using a thick target, utilizes an array of plasma calorimeters, time-of-flight charge collectors, and ballistic pendula, as described in previous studies [61] [122] [123]. These diagnostic capabilities would, however, have to be added to the current experimental apparatus.

An extension of the work described in Chapter 4 utilizing current diagnostic tools within the laboratory would be to investigate the effects of a varying laser spot size on the mass ablation rate, using a 1.064 µm laser. As described in Section 4.4, a numerical approximation for mass ablation rate derived from an experiment utilizing a 500 µm laser spot size [25] differs by a factor of 4 from the numerical approximation derived in Chapter 4, in which the laser spot size is 56 µm. The observed trend between the two experiments is that as laser spot size is reduced, the mass ablation rate increases, which is thought to occur due to increased plasma expansion in the focal plane. In order to verify this hypothesis, a single experiment should be conducted where the laser spot size is varied as irradiance is held constant. Mass ablation rate can be measured by the method described in Chapter 4, and the two-dimensional density profile should be measured by interferometry simultaneously in order to reveal the expansion profile. A difficulty in conducting this experiment is that laser energy would have to vary with the square of the laser spot size in order to maintain constant laser irradiance. In addition, a significant amount of data would have to be acquired if the layered-target method is to be used to measure mass ablation rate. The method described previously to measure mass ablation rate in a single laser pulse using a thick target could also be used but, as before, this would require the development of additional diagnostic capabilities.

Experiments to describe laser wavelength effects on ion properties throughout plasma expansion into vacuum, utilizing the Nd:YAG and CO_2 laser systems, are described in Chapter 5, with results summarized in Section 5.3. A significant limitation of these experimental results is the angular resolution. The ion probe is installed permanently at an angle of 51° with respect to target normal, so that all ion energy distributions represent data at a single angle in an anisotropic expansion [42]. The angular distribution of average ion energy was measured with an array of Faraday cups using the CO_2 laser, as described in Section 5.2.1, and has previously been measured by other authors using a Nd:YAG laser [19] [37]. However, measurements of the angular distribution of charge state and energy for each ion species in the expanding plasma would both improve the physical understanding of ion emission and expansion, and provide valuable data towards the commercial development of the EUV x-ray source application. Rotating the approximately 40 kg vacuum vessel containing the ion probe around the target normal is not a realistic solution for obvious reasons, so to conduct this experiment additional capabilities must be added to the current experimental apparatus. Specifically, a custom opto-mechanical stage should be developed to rotate the target inside the vacuum chamber while maintaining laser irradiation in focus and along the target normal; such a device has recently been described by other authors [124]. If the stage for angular resolution could be added to the current experimental apparatus then, e.g., the total energy carried by each ion species in all directions could be diagnosed, which would lead to a much better understanding of the energy balance in the laser-plasma interaction. In addition, the data could improve estimates of lifetime and erosion over the entire surface area of an EUV collection mirror positioned in the far expansion zone. Finally, the custom opto-mechanical stage could be utilized with all other diagnostics, so that, e.g., angular resolution of total EUV energy and the EUV spectrum could easily be diagnosed in future experiments.

An extension of the experiments discussed in Chapter 5 utilizing the current experimental apparatus is to measure the ion spectrum with and without a prepulse. As discussed in previous publications [29] [125], a low-intensity prepulse irradiating the target approximately 1 μs before the main pulse extends the initial density gradient scale length, which in turn reduces the internal plasma electric field thereby reducing space-charge acceleration of plasma ions. In previous experiments, the prepulse has been shown to reduce the average energy carried by all ions, as measured by a Faraday cup, by a factor of 10 [29]. Measurements of the charge state and energy distribution for each ion species in the expanding plasma, with and without a prepulse, have not been conducted. This data could be acquired using the ion probe discussed in Chapter 3, the Nd:YAG laser system discussed in Section 2.2.1, and one of a few additional Nd:YAG lasers in the current experimental apparatus to generate the prepulse. The data could reveal additional insights into the process of ion acceleration with a prepulse by revealing, e.g., if all ion energies are reduced by the same factor and how the ion energy distribution for each charge state depends on the prepulse beam properties. Conducting this experiment with angular resolution would further improve the physical understanding and value of the data to the EUV x-ray source community, however, this would require development of the custom opto-mechanical stage described previously.

Another limitation of the experimental data discussed in Chapter 5 is that neutral species are not considered, as they could not be detected with the current experimental apparatus based on charge collectors and electrostatic filtering of charged particles. Detection of neutral atoms in expanding plasma could be accomplished in future experiments using both spectroscopic and particle diagnostics. The technique of laser-induced fluorescence (LIF) utilizes a dye laser to generate fluorescence at a longer laser wavelength in the Sn^{+0} population, which is recorded by a CCD camera. A recent study utilizing the LIF technique demonstrated neutral particle emissions from a Nd:YAG LPP that were approximately 100 times the amount from a CO_2 LPP, in the parameter space of the EUV x-ray source application [126]. Error in the LIF method of diagnosing neutral emissions is introduced from continuum plasma emission at the fluorescence wavelength, calibration of the fluorescent photon to neutral atom ratio for the CCD camera, and scattering and absorption of the LIF laser by the plasma. A more direct method to diagnose neutral emissions in expanding plasma, which has not yet been applied within the EUV x-ray source community, is by the electrostatic filtering of ions and electrons to isolate the neutral component of the expanding plasma, which can subsequently be detected; similar probes have been described in the literature [127] [128]. The primary limitation of this diagnostic technique is that plasma density must be sufficiently low for complete separation of all ions and electrons, which in turn restricts the proximity to a high-density laser-produced plasma source. The proximity is also limited by the necessity for radial separation of expanding plasma radiation and expanding plasma particles, as a detector would be sensitive to both. The implementation of such a probe would be very similar to that of the ion probe discussed in Chapter 3. Specifically, a neutral atom probe would have to be mounted and aligned in a separate vacuum chamber at least 100 cm from the laser plasma source. In addition, such a probe would require high voltage inputs, and would require a detector sensitive to neutral Sn atoms with a known detection efficiency. If the neutral atom energies are too low for detection, a separate ionization and acceleration chamber may be necessary. The neutral atom probe described here could also be used with the custom opto-mechanical stage described previously to add angular resolution capabilities. All of this would greatly enhance the physical understanding of ion emission, acceleration, and recombination processes in the plasma, and could support the development of mitigation schemes for neutral atoms in the EUV x-ray source application.

The analytical and numerical analyses described in Chapter 6 and Chapter 7 verified the qualitative features observed in the experiments, and provided many additional insights into the physics of ion emission and expansion throughout expansion into vacuum. The 0D code discussed in Section 7.3 extends the analytical analysis described in Chapter 5, and the 1D code discussed in Section 7.4 extends the 0D code, so that the subsequent discussion addresses extension of the 1D code only. The most restrictive assumption in the 1D code is that initial conditions are assumed from physics-based considerations, rather than taken from experimental data or another radiation-hydrodynamic code simulating the plasma during the laser pulse. To couple experimental results to initial conditions in the 1D code, the temperature, density, and speed profile for the first few hundred μm would all have to be measured. The spatial decay of temperature close to the target surface can be measured by spectroscopic methods, such as the Boltzmann diagram and Stark broadening methods [129] [130]. The spatial decay of density can be measured by both spectroscopic and interferometric methods [42] [113]. In addition, time-of-flight spectroscopic methods can be used to measure the speed distribution close to the target surface [129] [131]. However, generating an accurate representation of the spatial profile of temperature, density, and speed close to the target surface by experimental methods is difficult due to the necessity of repeating experimental conditions as different diagnostic methods are applied, in addition to the several assumptions required to apply spectroscopic diagnostic techniques, such as the existence of local thermodynamic equilibrium and an optically thin plasma. A better technique to couple more realistic initial conditions to the 1D code is to use a bench-marked radiation hydrodynamics code to provide the initial density, temperature, and speed distributions. Radiation-hydrodynamic codes that have been used in previous studies to generate reliable approximations of the speed, density, and temperature distributions for laser-produced Sn plasma relevant to the EUV x-ray source application include MEDUSA [17], MED103 [132], STAR [120], HEIGHTS [133], HYADES [134], and h2d [42] [113].

Another modification to the 1D code extending its capabilities would be to incorporate two-fluid hydrodynamics. Currently, the code assumes that ions and electrons are accelerated together by a plasma pressure gradient which is a function of the combined ion and electron pressure, and that each Lagrangian cell is electrically neutral. These assumptions do not allow the code to simulate any spatial separation of electrons and ions, which may become an important mechanism once the electron-ion thermalization time exceeds the simulation time. In order to implement two-fluid hydrodynamics, separate grids for ions and electrons would be added, each with uniquely defined cell radii and speed at each boundary. Each cell boundary would advance in space and time by the respective pressure gradient, and the Leapfrog method discussed in Section 7.4.2 could again be utilized for the discretization. After each time step, both grids would be combined into a single, intermediate grid with a number of cells equal to the sum of cells in the electron and ion grids. The rate equations for the evolution of electron temperature, ion temperature, and number population for each ion species would then be integrated on the intermediate grid. Each cell in the intermediate grid would not necessarily be electrically neutral, so that Maxwell's equations would have to be solved and an additional acceleration on each cell wall would have to be considered. The two-fluid code described would result in a more accurate simulation of plasma dynamics in the far expansion zone, but as before, would most likely reproduce qualitative features only due to the approximation of initial conditions, the approximation of atomic rates, and the absence of plasma expansion in the focal plane in a 1D simulation.

Appendix A

Operation of the Ion Probe

This appendix summarizes the operating procedure for the custom-built ion probe discussed in Chapter 3. The most important consideration throughout operation of the ion probe is that it is contained in its own vacuum vessel with gate valves on both sides. Before any gate valves are opened, the pressure on each side of the valve must be equal. The ion probe must always be stored in vacuum, as atmospheric conditions will damage the channel electron multiplier.

A.1 Ion Probe Alignment

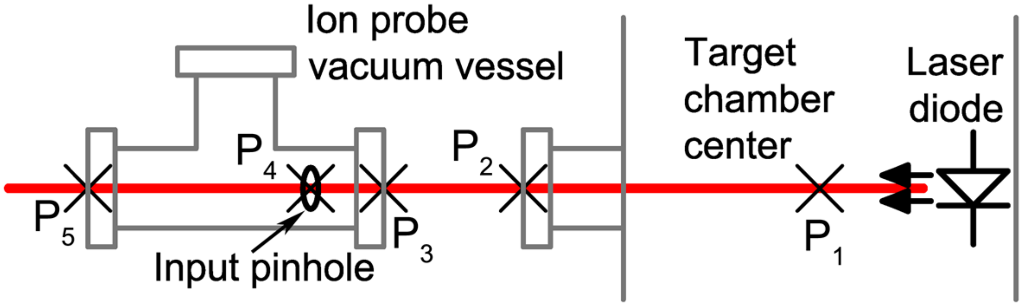

Figure A.1: Simplified schematic of the vacuum apparatus illustrating the alignment procedure for the ion probe, not to scale.

This first step in the operation is to ensure the probe is aligned to target chamber center (TCC). The following procedure can be used, or can be bypassed if the probe is assumed to be in alignment already, which can be verified if a high signal level is being generated. The five spatial locations labeled as P_1 to P_5 on the simplified schematic of the vacuum apparatus in Figure A.1 will all be collinear if the ion probe is properly aligned. An alignment laser can be made to intersect P_1, representing TCC, and P_2, which can be the intersection of thin threads made into crosshairs on the output of the vacuum port. In order to access the vacuum port at P_2, the vacuum extension from P_2 to P_3 will have to be removed (the procedure for bringing the ion probe vacuum vessel to atmospheric pressure is given subsequently). If the probe is aligned, the alignment laser intersecting P_1 and P_2 should also intersect P_3, representing crosshairs at the entrance vacuum port of the ion probe vacuum vessel, and P_4, representing the $100\,\mu$m input aperture to the ion probe. After the alignment laser intersects P_4, it will be scattered by the ion probe; the alignment laser can only intersect the crosshairs at P_5 if the ion probe is removed from its vacuum vessel. If TCC is lost for some reason, the previous location along the axis of the ion probe can be recovered by setting the alignment laser to intersect P_2, P_3, and P_4.

A.2 Ion Probe Vacuum System

The ion probe vacuum system is used in the following four modes:

- P_{store} – Store the ion probe under a moderate vacuum (less than a few torr)
- P_{atm} – Vent the ion probe to atmospheric pressure
- $P_{\text{vac, expt}}$ – Pump the ion probe to high vacuum (a few 10^{-7} torr) while the target chamber is also at high vacuum
- $P_{\text{vac, no expt}}$ – Pump the ion probe to high vacuum (a few 10^{-7} torr) while the target chamber is at a different pressure

The ion probe vacuum system controls include the following components, as shown in the photograph of the vacuum apparatus in Figure A.2, and in the photograph including vacuum controllers in Figure A.3.

- GV1 – manually-operated gate valve between the target chamber and the vacuum extension (at point P_2 in Figure A.1).

- GV2 – gas-operated gate valve between the rear end of the ion probe vacuum vessel and turbo pump (at point P_5 in Figure A.1). GV2 is controlled by the OPEN / CLOSE switch shown in Figure A.2, and requires a high-pressure air input of 80 to 90 psi, and a 115 VAC electrical input.

- Probe vent valve – manually-operated up-to-air valve shown in Figure A.2.

- Turbo pump vent valve – manually-operated up-to-air valve shown in Figure A.2.

- Turbo pump – Pfeiffer TPH/U 050 turbomolecular pump shown in Figure A.2.

- Turbo pump controller – Pfeiffer TCP 040 turbomolecular pump controller shown in Figure A.3.

- IHVG – High vacuum Ion gauge shown in Figure A.2.

- ILVG – Low vacuum convection gauge shown in Figure A.2.

- FPG – Convection gauge to monitor turbo pump foreline pressure shown in Figure A.2.

- Backing pump – Edwards E2M1.5 rotary vane vacuum pump used as an exhaust pump for the turbo pump, not shown in any figures.

- Foreline valve – Manually-operated valve between the FPG and vacuum tubing leading to the backing pump, not shown in any figures.

- FPG controller – Controller for FPG, shown in Figure A.3. At the present time, the controller/gauge is producing unreliable pressure data at the low end of its scale (less than a few torr).

The properties of the ion probe vacuum system controls are described in the Table A.1 for each of the four possible modes of the vacuum system. The operation of vacuum gauges are not described, but should follow standard procedure (e.g. only turn on the ion gauge under high vacuum). The backing pump is assumed to be turned ON/OFF with the turbo pump.

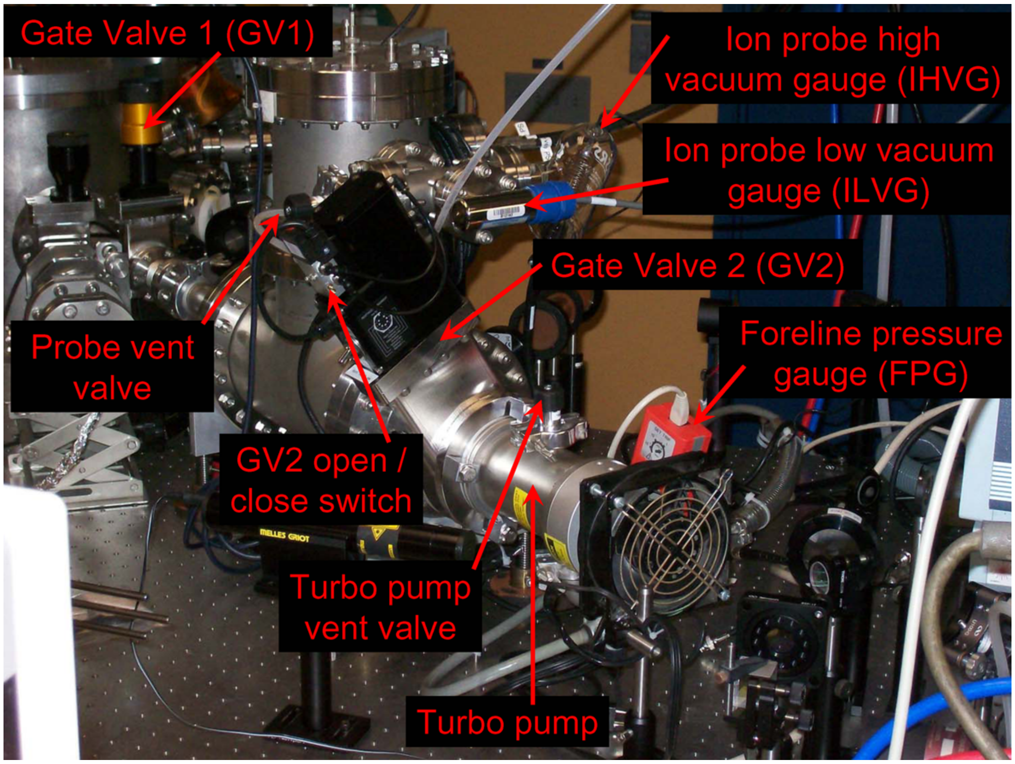

Figure A.2: Photograph of ion probe vacuum vessel with vacuum components labeled.

Table A.1: Properties for components of the vacuum system controls in the various modes of the vacuum system.

Mode	GV1	GV2	Probe vent valve	Turbo pump vent valve	Turbo pump	Foreline valve
P_{store}	CLOSE	CLOSE	CLOSE	CLOSE	OFF	CLOSE
P_{atm}	CLOSE	OPEN	OPEN	OPEN	OFF	CLOSE
$P_{\text{vac, expt}}$	OPEN	OPEN	CLOSE	CLOSE	ON	OPEN
$P_{\text{vac, no expt}}$	CLOSE	OPEN	CLOSE	CLOSE	ON	OPEN

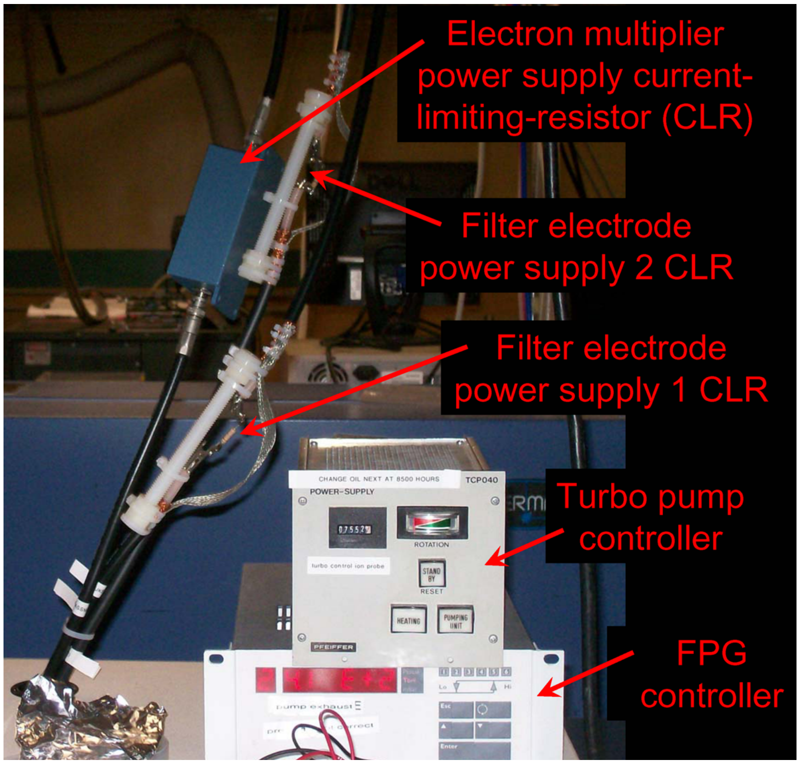

Figure A.3: Photograph of top of power supply cabinet showing vacuum controllers and current-limiting-resistors.

The vacuum system must be transferred back and forth between modes in the following order if an experiment is to be conducted:

$$P_{\text{store}} \longrightarrow P_{\text{atm}} \longrightarrow P_{\text{vac, no expt}} \longleftrightarrow P_{\text{vac, expt}} \longleftrightarrow P_{\text{vac, no expt}} \longrightarrow P_{\text{store}}\,,$$

or in the following order if an experiment is not being conducted:

$$P_{\text{store}} \longrightarrow P_{\text{atm}} \longrightarrow P_{\text{vac, no expt}} \longrightarrow P_{\text{store}}\,.$$

The vacuum system is transferred from the storage mode (P_{store}) to the atmospheric mode (P_{atm}) in the following procedure.

1. Verify GV1 and GV2 are closed
2. Slowly open the probe vent valve
3. Open the turbo pump vent valve if it is not already opened; note that the foreline valve should be closed for this entire procedure
4. GV2 can be opened after pressure is atmospheric on both sides

After both the turbo pump and ion probe vacuum vessel are at atmospheric pressure, pumping to high vacuum can begin. The vacuum system is transferred from the atmospheric mode (P_{atm}) to the high vacuum mode ($P_{\text{vac, no expt}}$) in the following procedure.

1. Verify GV1 is closed and GV2 is open; verify the foreline valve is closed
2. Close the probe vent valve and close the turbo pump vent valve
3. Turn on the fan behind the turbo pump – it requires 115 VAC.
4. Turn on the backing pump by plugging in the power cable to 115 VAC line voltage.
5. Let the backing pump run for a few minutes to ensure the tubing up to the foreline valve is evacuated and oil-free.
6. Verify the FPG controller is turned on and the reading is something on the order of atmospheric pressure (recall the FPG and FPG controller system is not currently working correctly)

7. Open the foreline valve to begin pumping both the turbo pump and the ion probe vacuum vessel to a rough vacuum.
8. Wait until the pressure in the ion probe vacuum vessel, as recorded by the ILVG is approximately a few torr – this should take no longer than two minutes if the vacuum system is leak-free.
9. Turn on the turbo pump by depressing *PUMPING UNIT* on the turbo pump controller. The lamp behind the button may illuminate and turn off and then on again a few times before it remains on.
10. Watch everything closely as the turbo pump spins up to top speed – this should take a few minutes. Pay particular attention to the temperature of the turbo pump – it should be cool to the touch.
11. The pressure as measured by the ILVG should drop below the minimum of its domain (10^{-4} torr) after about 20 to 30 minutes of pumping. At this time, the IHVG can be turned on to measure the high vacuum.
12. Note: GV2 always remains open and the backing pump and turbo pump fan always remain on when the system is at high vacuum.

At this stage, the ion probe vacuum vessel is at high vacuum and is isolated from the target chamber by GV1. An experiment can be conducted by transferring modes from $P_{\text{vac, no expt}}$ to $P_{\text{vac, expt}}$ in the following procedure.

1. Measure the pressure in the ion probe vacuum vessel by IHVG and measure the pressure in the target chamber (pumped externally) with another high vacuum gauge
2. If the two are approximately equal and less than a few 10^{-6} torr, GV1 can be opened and the experiment conducted.

The ion probe can be transferred back and forth between the modes $P_{\text{vac, no expt}}$ and $P_{\text{vac, expt}}$ by opening and closing GV1 (opened only if pressure is equalized on both sides). The ion probe vacuum vessel is transferred back to the storage mode ($P_{\text{vac, store}}$) from the high vacuum mode ($P_{\text{vac, no expt}}$) in the following procedure.

1. Verify GV1 is closed.
2. Verify that IHVG is turned off by using the controller.
3. Close GV2 using the GV2 OPEN/CLOSE switch. An audible *click* is heard to verify the gate valve has closed. GV2 can be open and closed a few times to verify its operation. If GV2 is connected to 115 VAC and the air pressure is at 80-90 psi it should be operating correctly.
4. Close the foreline valve and depress *PUMPING UNIT* on the turbo pump controller – the lamp behind the button will turn off.
5. Turn off the backing pump by unplugging it.
6. The turbo pump will begin to spin down by itself. It must be assisted in braking by introducing air in the system – if it spins down under high vacuum then turbo pump oil will flow onto the blades.
7. Open the turbo pump vent valve very, very slowly as the turbo pump spins down. Opening of the valve is verified by the pressure reading on the FPG controller rising slowly. The turbo pump should brake at a pressure no higher than a few 100 mtorr.
8. After the turbo pump has braked completely, bring its pressure to atmosphere by opening the turbo pump vent valve fully, then close the valve for storage.
9. Turn off the turbo pump fan.
10. The pressure within the ion probe vacuum vessel should rise no higher than a few torr over a time period of several days due to internal outgassing. If the pressure is rising higher, there is a leak somewhere.

A.3 Data Acquisition Procedure

After the ion probe vacuum vessel and target chamber are under a sufficient high vacuum, experiments can be conducted. First, verify the high voltage (HV) cables from the power supply control rack shown in Figure A.4 are connected through the current-limiting-resistors shown in Figure A.3 to the correct HV feedthroughs on the ion probe vacuum vessel shown in Figure A.5. The current-limiting-resistor for the Glassman HV power supply is properly contained in a grounded Ponoma box, whereas the two current-limiting-resistors for each filter electrode power supply are not enclosed. Extra attention should be paid to ensure the current-limiting-resistor for each filter electrode power supply is properly and safely connected.

At this point, the ion probe control rack can be turned ON using the switch shown in Figure A.4; the fan inside the control rack should turn on automatically. The control rack contains three high voltage power supplies – 2 identical Fluke 415B power supplies to generate the bipolar voltage on the filter electrodes, and a Glassman custom power supply that utilizes the custom controller shown in Figure A.4. Before turning on the power supplies, ensure the HV ENABLE switch on each control panel is turned OFF; at this point turn on all three power supplies. The Fluke 415B power supplies use tube amplifiers and thus take about 20 to 30 seconds to warm up; the white lamp next to the HV ENABLE switch will illuminate after this warm-up period. According to the manual for the Fluke 415B power supply, it must be turned ON for 20 to 30 minutes before voltage stability reaches its rated value (0.0005% or 5 mV, whichever is greater).

Before applying voltage to the electron multiplier using the Glassman HV power supply, it must be terminated into a load. This can be accomplished by connecting the signal out cable shown in Figure A.5 to a $50\,\Omega$ oscilloscope channel. The signal preamplifier (SP) shown in Figure A.5 requires the SP power supply to be turned ON. Before switching the HV ENABLE switch on the EMPS control system to ON, verify the voltage control potentiometer is rotated to 0%; also verify the multi-meter adjacent to the control system is turned ON and set to monitor a DC voltage. The DC voltage monitored by the multi-meter represents the high voltage from the Glassman PS reduced by a factor of 500. The HV ENABLE switch can be set to ON, at which point the multi-meter should read exactly 0. The voltage control potentiometer can now be rotated very slowly as the HV to the electron multiplier is increased. The typical voltage used in the experiments is 1875 V, which implies the multi-meter should display 3.75 V.

The final step before collecting data is to set the desired voltage on the filter electrodes. The equation relating the applied voltage to the KE/Z ratio derived in Chapter 3 is rewritten here as

$$\frac{KE}{Z} = 4.75 \times 2V_{BP}, \tag{A.1}$$

where V_{BP} is the bi-polar voltage (the setting for each power supply). As discussed previously in Chapter 3, there is a static error in the calculated KE/Z ratio of approximately 0.6% of the nominal value. Note that the bipolar voltages required to diagnose ions from Sn LPP in parameter space of the EUV x-ray source application are not exceedingly large. For example, to diagnose ions with a KE/Z ratio of 100 eV (typically a minimum setting), only 10.5 V is required on each power supply. Finally, as discussed in the Fluke 415B manual, to vary the voltage first turn off the HV ENABLE switch then change the voltage setting then turn back on the HV ENABLE switch.

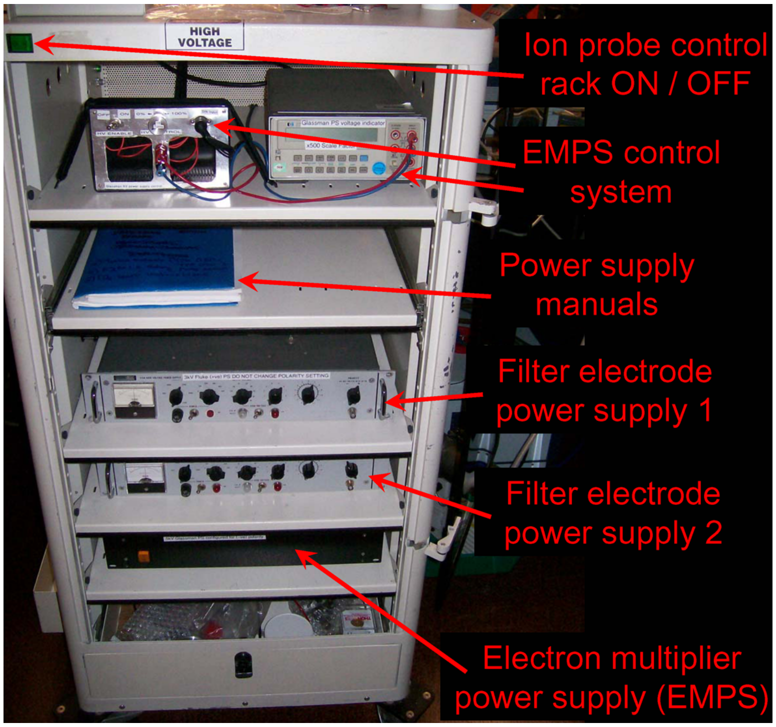

Figure A.4: Photograph of power supply cabinet for the ion probe electrodes and detector.

The electrical supplies to the ion probe are turned off in the following procedure. First, if the experiment is finished close GV1 to isolate the ion probe vacuum vessel from the target chamber. The electrical supplies should be turned off before transferring the vacuum system to the storage mode. The first step is to turn down the voltage on the Glassman power supply using the voltage control potentiometer. Following, the HV ENABLE switches on all three power supplies can be set to OFF, then all three power supplies can be turned OFF. Finally, the ion probe control rack power can be set to OFF, and the cabinet door closed (the top hinge is currently not working properly and may have to be compressed with a vise-grip wrench in order to be properly closed). The power to the signal preamplifier must also be turned OFF, and the signal out cable should be stored next to the ion probe vacuum vessel. At this point, the vacuum system can be transferred to the storage mode.

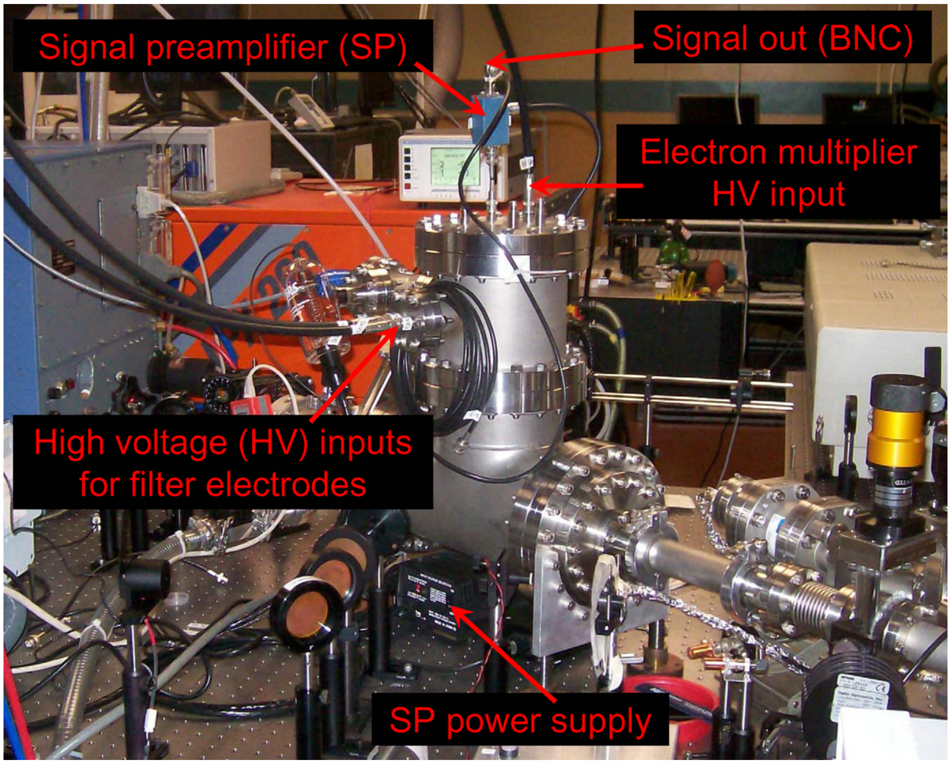

Figure A.5: Photograph of ion probe vacuum vessel with electrical components labeled.

Bibliography

[1] S. ATZENI and J. M. TER VEHN, *The Physics of Inertial Fusion: Beam Plasma Interaction, Hydrodynamics, Hot Dense Matter*, Oxford University Press, 2004.

[2] P. R. WILLMOTT and J. R. HUBER, *Reviews of Modern Physics* **72**, 315 (2000).

[3] D. COLOMBANT and G. F. TONON, *Journal of Applied Physics* **44**, 3524 (1973).

[4] F. AMIRANOFF, S. BATON, D. BERNARD, B. CROS, D. DESCAMPS, F. DORCHIES, F. JACQUET, V. MALKA, J. R. MARQUÈS, G. MATTHIEUSSENT, P. MINÉ, A. MODENA, P. MORA, J. MORILLO, and Z. NAJMUDIN, *Physical Review Letters* **81**, 995 (1998).

[5] G. MAINFRAY and G. MANUS, *Reports on Progress in Physics* **54**, 1333 (1991).

[6] W. KRUER, *The Physics of Laser Plasma Interactions*, Westview Press, 2003.

[7] H. R. GRIEM, *Plasma Spectroscopy*, McGraw-Hill, 1964.

[8] I. ROUDSKOY, *Laser and Particle Beams* **14**, 369 (1996).

[9] N. BASOV, G. VERGUNOVA, E. GAMALIT, V. GASILOV, N. DEMCHENKO, A. ISAKOV, A. KOLOGRIVOV, Y. MERKULIEV, V. ROZANOV, A. SAMARSKY, G. SKLIZKOV, V. TISHKIN, A. FAVORSKY, and A. SHIKANOV, *Journal of Experimental and Theoretical Physics* **84**, 564 (1983).

[10] M. H. KEY, W. T. TONER, T. J. GOLDSACK, J. D. KILKENNY, S. A. VEATS, P. F. CUNNINGHAM, and C. L. S. LEWIS, *Physics of Fluids* **26**, 2011 (1983).

[11] M. H. KEY, Energy Transport in Laser-Produced Plasmas, in *Physics of Laser Plasma*, edited by A. M. RUBENCHIK and S. WITKOWSKI, North-Holland, Amsterdam, 1991, Elsevier Science Publishers.

[12] C. W. GWYN, R. STULEN, D. SWEENEY, and D. ATTWOOD, *Journal of Vacuum Science and Technology B* **16**, 3142 (1998).

[13] R. C. SPITZER, T. J. ORZECHOWSKI, D. W. PHILLION, R. L. KAUFFMAN, and C. CERJAN, *Journal of Applied Physics* **79**, 2251 (1996).

[14] U. Stamm, *Journal of Physics D: Applied Physics* **37**, 3244 (2004).

[15] F. Jin and M. Richardson, *Appl. Opt.* **34**, 5750 (1995).

[16] A. Cummings, G. O'Sullivan, P. Dunne, E. Sokell, N. Murphy, and J. White, *Journal of Physics D: Applied Physics* **38**, 604 (2005).

[17] J. White, P. Dunne, P. Hayden, F. O'Reilly, and G. O'Sullivan, *Applied Physics Letters* **90**, 181502 (2007).

[18] M. Yamaura, S. Uchida, A. Sunahara, Y. Shimada, H. Nishimura, S. Fujioka, T. Okuno, K. Hashimoto, K. Nagai, T. Norimatsu, K. Nishihara, N. Miyanga, Y. Izawa, and C. Yamanaka, *Applied Physics Letters* **86**, 181107 (2005).

[19] H. Tanaka, A. Matsumoto, K. Akinaga, A. Takahashi, and T. Okada, *Applied Physics Letters* **87**, 041503 (2005).

[20] A. Takahashi, D. Nakamura, K. Tamaru, T. Akiyama, and T. Okada, *Applied Physics B: Lasers and Optics* **92**, 73 (2008).

[21] Y. Tao, M. S. Tillack, K. L. Sequoia, R. A. Burdt, S. Yuspeh, and F. Najmabadi, *Applied Physics Letters* **92**, 251501 (2008).

[22] T. Ando, S. Fujioka, H. Nishimura, N. Ueda, Y. Yasuda, K. Nagai, T. Norimatsu, M. Murakami, K. Nishihara, N. Miyanaga, Y. Izawa, K. Mima, and A. Sunahara, *Applied Physics Letters* **89**, 151501 (2006).

[23] M. Richardson, C. S. Koay, K. Takenoshita, C. Keyser, and M. Al-Rabban, *Journal of Vacuum Science and Technology B* **22**, 785 (2004).

[24] S. S. Harilal, M. S. Tillack, Y. Tao, B. O'Shay, R. Paguio, and A. Nikroo, *Opt. Lett.* **31**, 1549 (2006).

[25] S. Fujioka, H. Nishimura, K. Nishihara, M. Murakami, Y.-G. Kang, Q. Gu, K. Nagai, T. Norimatsu, N. Miyanaga, Y. Izawa, K. Mima, Y. Shimada, A. Sunahara, and H. Furukawa, *Applied Physics Letters* **87**, 241503 (2005).

[26] Y. Ueno, G. Soumagne, A. Sumitani, A. Endo, and T. Higashiguchi, *Applied Physics Letters* **91**, 231501 (2007).

[27] K. Takenoshita, C. S. Koay, S. George, S. Teerawattansook, and M. Richardson, *Journal of Vacuum Science and Technology B* **23**, 2879 (2005).

[28] S. S. Harilal, B. O'Shay, Y. Tao, and M. S. Tillack, *Applied Physics B: Lasers and Optics* **86**, 547 (2007), 10.1007/s00340-006-2532-3.

[29] Y. TAO, M. S. TILLACK, S. S. HARILAL, K. L. SEQUOIA, and F. NAJMABADI, *Journal of Applied Physics* **101**, 023305 (2007).

[30] B. SHARKOV and R. SCRIVENS, *IEEE Transactions on Plasma Science* **33**, 1778 (2005).

[31] L. LÁSKA, K. JUNGWIRTH, B. KRÁLIKOVÁ, J. KRÁSA, M. PFEIFER, K. ROHLENA, J. SKÁLA, J. ULLSCHMIED, J. BADZIAK, P. PARYS, J. WOLOWSKI, E. WORYNA, S. GAMMINO, L. TORRISI, F. P. BOODY, and H. HORA, *Plasma Physics and Controlled Fusion* **45**, 585 (2003).

[32] E. WORYNA, J. WOLOWSKI, B. KRÁLIKOVÁ, J. KRÁSA, L. LÁSKA, M. PFEIFER, K. ROHLENA, J. SKÁLA, V. PERINA, F. P. BOODY, R. HÖPFL, and H. HORA, *Review of Scientific Instruments* **71**, 949 (2000).

[33] S. GAMMINO, G. CIAVOLA, L. TORRISI, L. CELONA, J. WOLOWSKI, E. WORYNA, P. PARYS, L. LASKA, J. KRASA, and G. D. SHIRKOV, *Review of Scientific Instruments* **71**, 1119 (2000).

[34] P. FOURNIER, G. GREGOIRE, H. KUGLER, H. HASEROTH, N. LISI, C. MEYER, P. OSTROUMOV, J.-C. SCHNURIGER, R. SCRIVENS, F. V. RODRIGUEZ, B. H. WOLF, S. HOMENKO, K. MAKAROV, Y. SATOV, A. STEPANOV, S. KONDRASHEV, B. SHARKOV, and A. SHUMSHUROV, *Review of Scientific Instruments* **71**, 924 (2000).

[35] S. J. GITOMER, R. D. JONES, F. BEGAY, A. W. EHLER, J. F. KEPHART, and R. KRISTAL, *Physics of Fluids* **29**, 2679 (1986).

[36] D. W. FORSLUND, J. M. KINDEL, and K. LEE, *Phys. Rev. Lett.* **39**, 284 (1977).

[37] L. LASKA, J. KRASA, M. PFEIFER, K. ROHLENA, S. GAMMINO, L. TORRISI, L. ANDO, and G. CIAVOLA, *Review of Scientific Instruments* **73**, 654 (2002).

[38] Y. TAO, M. S. TILLACK, N. AMIN, R. A. BURDT, S. YUSPEH, N. M. SHAIKH, and F. NAJMABADI, *Review of Scientific Instruments* **80**, 123503 (2009).

[39] J. S. PEARLMAN, *Review of Scientific Instruments* **48**, 1064 (1977).

[40] E. WORYNA, P. PARYS, J. WOLOWSKI, and W. MRÓZ, *Laser and Particle Beams* **14**, 293 (1996).

[41] F. BIJKERK, G. HERGENHAN, G. SCHRIEVER, K. GABEL, M. SCHUERMANN, R. DE BRUIJN, S. A. VAN DER WESTEN, T. MISSALLA, U. STAMM, and V. BAKSHI, Cross-Calibration of Extreme Ultraviolet (EUV) Energy Sensors, Technical Report 04024498A-TR, SEMATECH, 2004.

[42] K. L. SEQUOIA, Y. TAO, S. YUSPEH, R. BURDT, and M. S. TILLACK, *Applied Physics Letters* **92**, 221505 (2008).

[43] W. STECKELMACHER, *Journal of Physics E: Scientific Instruments* **6**, 1061 (1973).

[44] D. C. SLATER, *Review of Scientific Instruments* **49**, 1493 (1978).

[45] I. G. KOZLOV and V. S. STRIZHENKO, *Soviet Physics – Technical Physics* **15**, 954 (1970).

[46] A. L. HUGHES and V. ROJANSKY, *Phys. Rev.* **34**, 284 (1929).

[47] P. MARMET and L. KERWIN, *Canadian Journal of Physics* **38**, 787 (1960).

[48] H. P. EUBANK and T. D. WILKERSON, *Review of Scientific Instruments* **34**, 12 (1963).

[49] S. DENUS, J. FARNY, Z. WERESZCZYNSKI, J. WOLOWSKI, and E. WORYNA, *Journal of Technical Physics* **18**, 25 (1977).

[50] D. P. HALE and W. D. ALLEN, *Journal of Physics E: Scientific Instruments* **4**, 311 (1971).

[51] H. H. FLEISCHMANN, D. E. ASHBY, and A. V. LARSON, *Nuclear Fusion* **5**, 349 (1965).

[52] J. H. MOORE, C. C. DAVIS, and M. A. COPLAN, *Building Scientific Apparatus*, Westview Press, 3rd edition, 2003.

[53] R. LATHAM, *High Voltage Vacuum Insulation*, Academic Press, Inc., 1995.

[54] E. FLAXER, *Measurement Science and Technology* **17**, N37 (2006).

[55] J. FRICKE, A. MÜLLER, and E. SALZBORN, *Nuclear Instruments and Methods* **175**, 379 (1980).

[56] S. SHCHEMELININ, S. PSZONA, G. GARTY, A. BRESKIN, and R. CHECHIK, *Nuclear Instruments and Methods in Physics Research Section A: Accelerators, Spectrometers, Detectors and Associated Equipment* **438**, 447 (1999).

[57] M. TASSOTTO and P. R. WATSON, *Review of Scientific Instruments* **71**, 2704 (2000).

[58] M. KREMS, J. ZIRBEL, M. THOMASON, and R. D. DUBOIS, *Review of Scientific Instruments* **76**, 093305 (2005).

[59] J. R. TAYLOR, *An Introduction to Error Analysis: The Study of Uncertainties in Physical Measurements*, University Science Books, 2nd edition, 1996.

[60] R. FABBRO, E. FABRE, F. AMIRANOFF, C. GARBAN-LABAUNE, J. VIRMONT, M. WEINFELD, and C. E. MAX, *Phys. Rev. A* **26**, 2289 (1982).

[61] A. Ng, D. Pasini, P. Celliers, D. Parfeniuk, L. D. Silva, and J. Kwan, *Applied Physics Letters* **45**, 1046 (1984).

[62] F. Dahmani, *Journal of Applied Physics* **74**, 622 (1993).

[63] F. Dahmani and T. Kerdja, *Laser and Particle Beams* **9**, 769 (1991).

[64] R. A. Burdt, S. Yuspeh, K. L. Sequoia, Y. Tao, M. S. Tillack, and F. Najmabadi, *Journal of Applied Physics* **106**, 033310 (2009).

[65] P. Mora, *Physics of Fluids* **25**, 1051 (1982).

[66] R. Fabbro, C. Max, and E. Fabre, *Physics of Fluids* **28**, 1463 (1985).

[67] F. Dahmani and T. Kerdja, *Physics of Fluids B: Plasma Physics* **3**, 1232 (1991).

[68] R. C. Spitzer, R. L. Kauffman, T. Orzechowski, D. W. Phillion, and C. Cerjan, *Journal of Vacuum Science and Technology B* **11**, 2986 (1993).

[69] S. Fujioka, H. Nishimura, K. Nishihara, A. Sasaki, A. Sunahara, T. Okuno, N. Ueda, T. Ando, Y. Tao, Y. Shimada, K. Hashimoto, M. Yamaura, K. Shigemori, M. Nakai, K. Nagai, T. Norimatsu, T. Nishikawa, N. Miyanaga, Y. Izawa, and K. Mima, *Phys. Rev. Lett.* **95**, 235004 (2005).

[70] Y. Tao, F. Sohbatzadeh, H. Nishimura, R. Matsui, T. Hibino, T. Okuno, S. Fujioka, K. Nagai, T. Norimatsu, K. Nishihara, N. Miyanaga, Y. Izawa, A. Sunahara, and T. Kawamura, *Applied Physics Letters* **85**, 1919 (2004).

[71] D. R. Gray and J. D. Kilkenny, *Plasma Physics* **22**, 81 (1980).

[72] J. T. Larsen and S. M. Lane, *Journal of Quantitative Spectroscopy and Radiative Transfer* **51**, 179 (1994), Special Issue Radiative Properties of Hot Dense Matter.

[73] K. L. Sequoia, *Extreme-ultraviolet radiation transport in small scale length laser-produced tin plasmas*, PhD dissertation, University of California San Diego, Mechanical and Aerospace Engineering, 2009.

[74] R. A. Burdt, Y. Tao, M. S. Tillack, S. Yuspeh, N. M. Shaikh, E. Flaxer, and F. Najmabadi, *Journal of Applied Physics* **107**, 043303 (2010).

[75] R. A. Burdt, Y. Ueno, Y. Tao, S. Yuspeh, M. S. Tillack, and F. Najmabadi, *Applied Physics Letters* **97**, 041502 (2010).

[76] R. M. CLEMENT, R. A. DAVIES, H. T. MILES, and S. K. SETHURAMAN, *Journal of Physics D: Applied Physics* **13**, 1643 (1980).

[77] R. KELLY and R. W. DREYFUS, *Surface Science* **198**, 263 (1988).

[78] G. T. TALLENTS, *Optics Communications* **37**, 108 (1981).

[79] G. T. TALLENTS, *Optics Communications* **38**, 448 (1981).

[80] R. RAO, *Linear Statistical Interference and Its Applications*, Wiley, New York, 2nd edition, 1973.

[81] C. W. ALLEN, *Astrophysical Quantities*, p. 90, Athlone, London, 1955.

[82] A. V. GUREVICH and L. P. PITAEVSKIĬ, *Soviet Physics JETP* **19**, 870 (1964).

[83] P. T. RUMSBY and J. W. M. PAUL, *Plasma Physics* **16**, 247 (1974).

[84] H. PUELL, *Zeitschrift Naturforschung Teil A* **25**, 1807 (1970).

[85] A. THUM-JAGER and K. ROHR, *Journal of Physics D: Applied Physics* **32**, 2827 (1999).

[86] N. M. KUZNETSOV and YU. P. RAIZER, *Journal of Applied Mechanics and Technical Physics* **6**, 6 (1965), 10.1007/BF01565811.

[87] M. MATTIOLI, *Plasma Physics* **13**, 19 (1971).

[88] G. S. VORONOV and L. E. CHERNYSHEV, *Soviet Physics – Technical Physics* **18**, 940 (1974).

[89] B. E. PATON and N. R. ISENOR, *Canadian Journal of Physics* **46**, 1237 (1968).

[90] YU. A. BYKOVSKII, N. N. DEGTYARENKO, V. I. DYMOVICH, V. F. ELESIN, YU. P. KOZYREV, B. I. NIKOLAEV, S. V. RYZHIKH, and S. M. SIL'NOV, *Soviet Physics – Technical Physics* **14**, 1269 (1970).

[91] R. DINGER, K. ROHR, and H. WEBER, *Journal of Physics D: Applied Physics* **13**, 2301 (1980).

[92] W. DEMTRODER and W. JANTZ, *Plasma Physics* **12**, 691 (1970).

[93] YA. B. ZEL'DOVICH and YU. P. RAIZER, *Physics of Shock Waves and High-Temperature Hydrodynamic Phenomena*, Dover Publications, Inc., 2002.

[94] J. KRASA, L. LASKA, K. ROHLENA, M. PFEIFER, J. SKALA, B. KRALIKOVA, P. STRAKA, E. WORYNA, and J. WOLOWSKI, *Applied Physics Letters* **75**, 2539 (1999).

[95] E. L. CLARK, K. KRUSHELNICK, M. ZEPF, F. N. BEG, M. TATARAKIS, A. MACHACEK, M. I. K. SANTALA, I. WATTS, P. A. NORREYS, and A. E. DANGOR, *Phys. Rev. Lett.* **85**, 1654 (2000).

[96] A. SASAKI, A. SUNAHARA, K. NISHIHAWRA, T. NISHIKAWA, F. KOIKE, and H. TANUMA, *Journal of Physics: Conference Series* **112**, 042062 (2008).

[97] Y. TAO and M. S. TILLACK, *Applied Physics Letters* **89**, 111502 (2006).

[98] A. LORUSSO, J. KRASA, K. ROHLENA, V. NASSISI, F. BELLONI, and D. DORIA, *Applied Physics Letters* **86**, 081501 (2005).

[99] Y. UENO, G. SOUMAGNE, A. SUMITANI, A. ENDO, T. HIGASHIGUCHI, and N. YUGAMI, *Applied Physics Letters* **92**, 211503 (2008).

[100] D. R. BATES, A. E. KINGSTON, and R. W. P. MCWHIRTER, *Proceedings of the Royal Society of London. Series A. Mathematical and Physical Sciences* **267**, 297 (1962).

[101] R. R. GOFORTH and P. HAMMERLING, *Journal of Applied Physics* **47**, 3918 (1976).

[102] G. L. PAYNE, J. D. PEREZ, T. E. SHARP, and B. A. WATSON, *Journal of Applied Physics* **49**, 4688 (1978).

[103] A. CARUSO, G. GATTI, and C. STRANGIO, *Il Nuovo Cimento D* **2**, 1213 (1983).

[104] I. KUNZ, *Interpretation of Ion Energy Spectra by the Recombination Model*, PhD dissertation, Technische Hochschule, Darmstadt, Germany, F.R., 1990.

[105] V. BARANOV, K. MAKAROV, V. ROERICH, Y. SATOV, A. STAROSTIN, A. STEPANOV, B. SHARKOV, V. BARANOV, K. MAKAROV, V. ROERICH, Y. SATOV, A. STAROSTIN, A. STEPANOV, K. LANGBEIN, and T. SHERWOOD, *Laser and Particle Beams* **14**, 347 (1996).

[106] A. E. STEPANOV, YU. A. SATOV, K. N. MAKAROV, V. C. ROERICH, Y. B. SMAKOVSKIY, D. D. MALUTA, and A. N. STAROSTIN, *Plasma Physics and Controlled Fusion* **45**, 1261 (2003).

[107] J. WHITE, P. HAYDEN, P. DUNNE, A. CUMMINGS, N. MURPHY, P. SHERIDAN, and G. O'SULLIVAN, *Journal of Applied Physics* **98**, 113301 (2005).

[108] G. O'SULLIVAN, A. CUMMINGS, P. DUNNE, P. HAYDEN, L. MCKINNEY, N. MURPHY, and J. WHITE, Atomic Physics of Highly Charged Ions and the Case for Sn as a Source Material, in *EUV Sources for Lithography*, edited by V. BAKSHI, pp. 149–168, SPIE Press, 2006.

[109] T. A. CARLSON, C. NESTOR, JR., N. WASSERMAN, and J. MCDOWELL, *Atomic Data and Nuclear Data Tables* **2**, 63 (1970).

[110] S. LOCH, M. PINDZOLA, and D. GRIFFIN, *International Journal of Mass Spectrometry* **271**, 68 (2008).

[111] M. R. ZAGHLOUL, M. A. BOURHAM, and J. M. DOSTER, *Journal of Physics D: Applied Physics* **33**, 977 (2000).

[112] Y. TAO, M. TILLACK, S. YUSEPH, R. BURDT, and F. NAJMABADI, *Applied Physics B: Lasers and Optics* **99**, 397 (2010).

[113] S. YUSPEH, K. L. SEQUOIA, Y. TAO, M. S. TILLACK, R. A. BURDT, and F. NAJMABADI, *Applied Physics Letters* **96**, 261501 (2010).

[114] R. W. P. MCWHIRTER, Spectral Intensities, in *Plasma Diagnostic Techniques*, edited by R. H. HUDDLESTONE and S. L. LEONARD, p. 201, London, 1965, Academic Press.

[115] L. SPITZER, *Physics of Fully Ionized Gases*, p. 144, Dover Publications, Inc., New York, second edition, 1990.

[116] L. F. SHAMPINE and M. W. REICHELT, *SIAM Journal on Scientific Computing* **18**, 1 (1997).

[117] F. F. CHEN, *Introduction to Plasma Physics*, pp. 158–159, Plenum Press, New York, 1974.

[118] Y. TAO, H. NISHIMURA, S. FUJIOKA, A. SUNAHARA, M. NAKAI, T. OKUNO, N. UEDA, K. NISHIHARA, N. MIYANAGA, and Y. IZAWA, *Applied Physics Letters* **86**, 201501 (2005).

[119] Y. Y. TSUI, R. FEDOSEJEVS, A. A. OFFENBERGER, R. RANKIN, and C. E. CAPJACK, *Physics of Fluids B: Plasma Physics* **5**, 4115 (1993).

[120] K. NISHIHARA, A. SUNAHARA, A. SASAKI, M. NUNAMI, H. TANUMA, S. FUJIOKA, Y. SHIMADA, K. FUJIMA, H. FURUKAWA, T. KATO, F. KOIKE, R. MORE, M. MURAKAMI, T. NISHIKAWA, V. ZHAKHOVSKII, K. GAMATA, A. TAKATA, H. UEDA, H. NISHIMURA, Y. IZAWA, N. MIYANAGA, and K. MIMA, *Physics of Plasmas* **15**, 056708 (2008).

[121] J. WHITE, G. O'SULLIVAN, S. ZAKHAROV, P. CHOI, V. ZAKHAROV, H. NISHIMURA, S. FUJIOKA, and K. NISHIHARA, *Applied Physics Letters* **92**, 151501 (2008).

[122] B. MEYER and G. THIELL, *Physics of Fluids* **27**, 302 (1984).

[123] J. GRUN, R. DECOSTE, B. H. RIPIN, and J. GARDNER, *Applied Physics Letters* **39**, 545 (1981).

[124] O. MORRIS, A. O'CONNOR, E. SOKELL, and P. DUNNE, *Plasma Sources Science and Technology* **19**, 025007 (2010).

[125] D. NAKAMURA, T. AKIYAMA, K. OKAZAKI, K. TAMARU, A. TAKAHASHI, and T. OKADA, *Journal of Physics D: Applied Physics* **41**, 245210 (2008).

[126] Y. MATSUOKA, Y. NAKAI, S. FUJIOKA, S. MAEDA, M. SHIMOMURA, Y. SHIMADA, A. SUNAHARA, H. NISHIMURA, and M. YOSHIDA, *Applied Physics Letters* **97**, 111502 (2010).

[127] S. SARRAF and D. M. WOODALL, *Review of Scientific Instruments* **49**, 1147 (1978).

[128] L. TORRISI, L. ANDÓ, S. GAMMINO, J. KRÁSA, and L. LÁSKA, *Nuclear Instruments and Methods in Physics Research Section B: Beam Interactions with Materials and Atoms* **184**, 327 (2001).

[129] S. S. HARILAL, B. O'SHAY, M. S. TILLACK, and M. V. MATHEW, *Journal of Applied Physics* **98**, 013306 (2005).

[130] N. M. SHAIKH, Y. TAO, R. A. BURDT, S. YUSPEH, N. AMIN, and M. S. TILLACK, *Journal of Applied Physics* **108**, 083109 (2010).

[131] M. V. MATHEW, S. S. HARILAL, and M. S. TILLACK, *Journal of Physics D: Applied Physics* **40**, 447 (2007).

[132] J. WHITE, P. DUNNE, P. HAYDEN, and G. O'SULLIVAN, *Journal of Applied Physics* **106**, 113303 (2009).

[133] V. SIZYUK, A. HASSANEIN, and T. SIZYUK, *Journal of Applied Physics* **100**, 103106 (2006).

[134] B. O'SHAY, F. NAJMABADI, S. S. HARILAL, and M. S. TILLACK, *Journal of Physics: Conference Series* **59**, 773 (2007).